

A general model for the identification of specific PAHs in the far-IR[★]

G. Mulas^{1,2}, G. Mallocci^{1,2}, C. Joblin², and D. Toublanc²

¹ INAF – Osservatorio Astronomico di Cagliari, Astrochemistry Group, Strada n.54, Loc. Poggio dei Pini, 09012 Capoterra (CA), Italy

e-mail: [gmulas;gmallocci]@ca.astro.it

² Centre d'Etude Spatiale des Rayonnements, CNRS et Université Paul Sabatier Toulouse 3, Observatoire Midi-Pyrénées, 9 Avenue du Colonel Roche, 31028 Toulouse Cedex 04, France

e-mail: [giuliano.mallocci;christine.joblin;dominique.toublanc]@cesr.fr

Received 29 September 2005 / Accepted 9 June 2006

ABSTRACT

Context. In the framework of the interstellar PAH hypothesis, far-IR skeletal bands are expected to be a fingerprint of single species in this class.

Aims. A detailed model of the photo-physics of interstellar PAHs is required for such single-molecule identification of their far-IR features in the presently available Infrared Space Observatory data and in those of the forthcoming Herschel Space Observatory mission.

Methods. We modelled the detailed photophysics of a vast sample of species in different radiation fields, using a compendium of Monte-Carlo techniques and quantum-chemical calculations. This enabled us to validate the use of purely theoretical data and assess the expected accuracy and reliability of the resulting synthetic far-IR emission spectra.

Results. We produce positions and intensities of the expected far-IR features that ought to be emitted by each species in the sample in the considered radiation fields. A composite emission spectrum for our sample is computed for one of the most favourable sources for detection, namely the Red Rectangle nebula. The resulting spectrum is compared with the estimated dust emission in the same source to assess the dependence of detectability on key molecular parameters.

Conclusions. Identifying specific PAHs from their far-IR features is going to be a difficult feat in general; still, it may well be possible under favourable conditions.

Key words. astrochemistry – line: identification – molecular processes – ISM: lines and bands – ISM: molecules – infrared: ISM

1. Introduction

The hypothesis of the ubiquitous presence of free gas-phase polycyclic aromatic hydrocarbons (PAHs) in the interstellar medium (ISM) originated about 20 years ago (Léger & Puget 1984; Allamandola et al. 1985). Due to their spectral properties and their high photostability, these molecules were suggested as the most natural interpretation for the aromatic infrared bands (AIBs), a set of emission bands observed near 3.3, 6.2, 7.7, 8.6, 11.3, and 12.7 μm , in many dusty environments excited by UV photons (Léger et al. 1989; Allamandola et al. 1989). The AIBs are the spectral fingerprint of the excitation of vibrations in aromatic C–C and C–H bonds (Duley & Williams 1981). Furthermore, PAHs and their cations were also supposed to account for a subset of diffuse interstellar bands (DIBs) (Léger & d'Hendecourt 1985; van der Zwet & Allamandola 1985; Crawford et al. 1985), more than 300 absorption features observed in the near-UV, visible and near-IR in the spectra of reddened stars (Herbig 1995; Ehrenfreund & Charnley 2000; Draine 2003) in the Milky Way, as well as in external galaxies (Ehrenfreund et al. 2002; Sollerman et al. 2005).

These PAHs are believed to play an important role in the physics and chemistry of the ISM, showing intermediate properties between gas and dust phases, i.e. behaving at the same time both as very small grains and large molecules. This has motivated many observational, experimental, and theoretical efforts in the last two decades, which confirmed that PAH-related species are promising candidates for explaining AIBs and some of the DIBs, accounting for a substantial fraction of the total interstellar carbon budget (Salama 1999). However, despite the large number of studies and the tentative identification of neutral anthracene and pyrene in the Red Rectangle nebula (Vijh et al. 2004, 2005; Mulas et al. 2006b), no *definitive* spectral identification of any *specific* individual member in this class exists to date.

The large number of low-temperature matrix isolation spectroscopy studies of PAHs are of fundamental importance in assessing the link between their optical absorption spectra and DIBs (Joblin et al. 1995b; Salama et al. 1996, 1999; Salama 1999; Ruiterkamp et al. 2002, 2005); at the same time, they do not permit an unambiguous identification of any single PAH, due to the unpredictable matrix-induced broadening and shift of the absorption bands. Measurements of the electronic absorption spectrum of cold PAH ions in gas phase (Romanini et al. 1999; Pino et al. 1999; Bréchnignac & Pino 1999; Biennier et al. 2003, 2004; Sukhorukov et al. 2004; Tan & Salama 2005a,b) are

[★] Appendices are only available in electronic form at <http://www.aanda.org>

“the right way” to identify specific PAHs based on their optical absorption spectrum, but each of them still represents a demanding experimental task, which can hardly be generalised in a systematic way to a representative sample of this vast class of molecules.

As to IR spectroscopy, “classical” AIBs do not permit unambiguous identification of any single species, because vibrational transitions in the near and medium IR are a common feature of the whole class of PAHs (Langhoff 1996; Salama 1999). These vibrational modes just probe specific chemical bonds and not the overall structure of the whole molecule. Indeed, the emission in these bands is usually explained by assuming a whole population of different PAHs to contribute to them (Schutte et al. 1993; Cook & Saykally 1998; Allamandola et al. 1999; Bakes et al. 2001a,b; Pech et al. 2002).

On the other hand, every single such molecule ought to show a unique spectral fingerprint in the far-IR spectral region, which contains the low-frequency vibrational modes associated with collective oscillations of the whole skeletal structure (Zhang et al. 1996; Joblin et al. 2002; Mulas et al. 2003). Moreover, far-IR bands tend to be emitted when the excitation energy of the molecule is relatively low (Joblin et al. 2002); this results in slower internal vibrational redistribution of energy and thus smaller lifetime broadening, implying that their rotational envelopes might still be discernible, as suggested by the gas-phase laboratory measurements of Zhang et al. (1996). It might then be possible to resolve the rotational structure with a high resolution spectrometer, such as the HIFI heterodyne spectrometer onboard the forthcoming Herschel Space Observatory (HSO) mission¹, providing one more crucial identification element for interstellar PAHs (Joblin et al. 2002).

The far-IR spectrum emitted by a given interstellar PAH will essentially depend only on its molecular properties and on the exciting radiation field, and can be modelled in detail if all these “ingredients” are known (Joblin et al. 2002; Mallocci et al. 2003; Mulas et al. 2003, 2006b). Here we make use of a database of theoretical spectral properties of a sample of PAHs (Mallocci et al. 2006) to derive their expected far-IR emission in a grid of radiation fields (RFs) covering some of the environments in which the AIBs, commonly attributed to PAHs, have been observed.

In this paper we describe the modelling procedure, explain the approximations used, and assess their impact on the resulting calculated spectra, both in terms of absolute fluxes and band ratios. Then we present the calculated spectra for a large sample of PAHs and their cations. Our approach can also be used to model molecular rotation and thus the expected rotational envelopes of far-IR emission bands (Joblin et al. 2002). This calculation is very demanding from a computational point of view and is the subject of forthcoming work (Mulas et al. 2006b).

In Sect. 2 we summarise the modelling procedure we used. We then proceed in Sect. 3 to validate our modelling approach, concerning respectively the use of theoretical UV-visible photo-absorption spectra (Sect. 3.1), the impact of some necessary simplifying assumptions for the molecular relaxation processes following electronic excitation (Sect. 3.2), and its comparison with an independently developed model (Sect. 3.3). Results are presented in Sect. 4, while Sect. 5 discusses the diagnostic potential and limitations of the calculated spectra.

2. Modelling procedure

Our Monte-Carlo (MC) modelling procedure is described in detail elsewhere (Mulas 1998; Joblin et al. 2002; Mallocci et al. 2003; Mulas et al. 2003, 2006b). It requires the following parameters:

1. the exciting radiation field;
2. the UV-visible photo-absorption cross-section up to the Lyman limit;
3. the dominant de-excitation pathways following the absorption of an UV-visible photon;
4. the complete vibrational analysis in the electronic ground state (frequencies, symmetry of the modes and intensities of the IR-active modes).

These data, along with some general assumptions on the photophysics of PAHs, enable one to calculate all the probabilities involved in the exchange of photons between the molecule and the radiation field. Until recently the general applicability of this procedure was hindered by the scarcity of complete photo-absorption spectra of neutral and cationic PAHs ranging from the visible to the Lyman limit at 13.6 eV. However, we recently produced theoretical UV-visible photo-absorption spectra for a sample of 20 PAHs and their cations, using the time-dependent density functional theory (TD-DFT, e.g. Marques & Gross 2004) implementation in the OCTOPUS computer code (Marques et al. 2003), and showed them to be in good agreement with available experimental data (Joblin 1992; Joblin et al. 1992); this validated the use of the former as a decent surrogate when the latter are not available (Mallocci et al. 2004).

We here extend our previous work (Mulas et al. 2003) to the whole sample of molecules studied in Mallocci et al. (2004), using the theoretical photo-absorption cross-sections published therein and computing the vibrational frequencies with the NWChem code (Straatsma et al. 2003). Following previously published calibration calculations (Langhoff 1996; Bauschlicher & Langhoff 1997), we obtained the full vibrational analyses using the exchange-correlation functional B3LYP (Becke 1993) and the 4–31G basis set (Frisch et al. 1984). The vibrational frequencies obtained at the B3LYP/4–31G level of theory are usually scaled with an empirical factor of 0.958, which accounts for anharmonicity and other minor corrections (Langhoff 1996; Bauschlicher & Langhoff 1997; Hudgins et al. 2001) and brings them into near coincidence with experimental data. Our calculated vibrational frequencies are in good agreement with the previously published results. Since the aim of the present paper is to produce synthetic spectra that are as accurate as possible for direct comparison with observational data, we scale the computed vibrational frequencies with the above empirical factor in a different way from what we did in our proof-of-concept papers on ovalene, in which we applied no such scaling (Mallocci et al. 2003; Mulas et al. 2003). The only gas-phase emission data for PAHs in the far-IR currently available are, to the best of our knowledge, those by Zhang et al. (1996) and those by Pirali (2004) and Pirali et al. (2006). The comparison between our calculated band positions and the experimental data is shown in Table 1. The differences among frequencies may be partly due to the temperature effects, since in both experiments PAHs have to be heated. Inspection of Table 1 shows that the empirical scale factor calibrated on mid-IR data is probably not the best one for far-IR bands. More work is needed both from an experimental point of view, to study the temperature effect on band position and width, and from a theoretical point of view, to derive the best empirical scaling procedure for this spectral

¹ www.sron.nl/divisions/lea/hifi/directory.html

Table 1. Comparison between available far-IR gas-phase laboratory measurements (Zhang et al. 1996; Pirali 2004; Pirali et al. 2006, first column), our DFT results, both unscaled (second column) and scaled with an empirical factor of ~ 0.958 (third column) and the previously published DFT results (Langhoff 1996; Martin et al. 1996, last column).

Band positions (cm^{-1})			
Experimental	Unscaled DFT	Scaled DFT	Previous DFT
Naphthalene (C_{10}H_8)			
167.0 ^a , 166 ^c	178.2	170.8	171.8 ^d , 171 ^e
360.6 ^a , 359 ^c	376.3	360.5	357.7 ^d , 359 ^e
Anthracene ($\text{C}_{14}\text{H}_{10}$)			
87 ^c	94.7	90.7	91.0 ^d , 90 ^e
227 ^c	239.0	228.9	232.3 ^d , 232 ^e
Phenanthrene ($\text{C}_{14}\text{H}_{10}$)			
97 ^c	104.3	99.9	99 ^e
221 ^c	235.8	225.9	226.8 ^d , 226 ^e
Pyrene ($\text{C}_{16}\text{H}_{10}$)			
95.0 ^a , 95 ^c	102.7	98.4	98.6 ^d
214.2 ^a , 207 ^c	218.4	209.2	210.0 ^d
350.0 ^a , 348 ^c	368.6	353.1	353.5 ^d
Chrysene ($\text{C}_{18}\text{H}_{12}$)			
173 ^c	192.8	184.7	–
231.5 ^a , 233 ^c	242.7	232.5	233.0 ^d
Perylene ($\text{C}_{20}\text{H}_{12}$)			
–	98.9	94.8	98.6 ^d
–	182.7	175.0	175.9 ^d
464.9 ^b	479.7	459.6	462.0 ^d

^a Gas-phase emission measurements (Zhang et al. 1996);

^b Gas-phase emission measurements (Pirali 2004);

^c Gas-phase emission measurements (Pirali et al. 2006);

^d B3LYP/4–31G calculation (Langhoff 1996);

^e B3LYP/cc-pVDZ calculation (Martin et al. 1996).

range. For the time being, the calculated positions of the bands in this work may therefore be affected by a small systematic error due to the scaling adopted, and some caution is needed for interpreting them. All the vibrational frequencies (not only the IR-active ones) are used within the MC model to compute the density of vibrational states as a function of energy (e.g. Mulas 1998; Cook & Saykally 1998). These data are being integrated in an online database of computed molecular properties, which is under construction (Mallocci et al. 2006).

For the present simulations we used the relatively UV-poor RF of the extended halo surrounding the Red Rectangle proto-planetary nebula (Men'shchikov et al. 2002; Mulas et al. 2006b), the interstellar RF (ISRF) in the galactic plane at about 5 kpc from the galactic centre (as given by Mathis et al. 1983) and the relatively UV-rich RF in the photodissociation region (PDR) of the planetary nebula IRAS 21282+5050 (Pech et al. 2002). The RFs considered are shown in Fig. 1; note that the RF of the extended halo of the Red Rectangle drops to negligible values above ~ 9 eV on the scale of this plot. This choice of RFs is by no means intended to represent a choice of the environments in which we expect the far-IR bands of PAHs to be most easily detected. They were chosen to span the range of conditions in

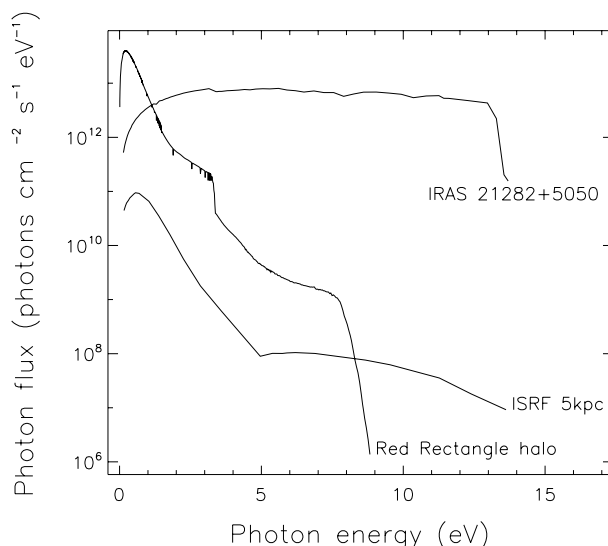


Fig. 1. The RFs considered, namely the ISRF given by Mathis et al. (1983), the RF of the extended halo surrounding the Red Rectangle proto-planetary nebula and the relatively UV-rich RF in the PDR of the planetary nebula IRAS 21282+5050; the latter two were obtained respectively from observational data (Vijh et al. 2004, 2005) and from an appropriate stellar atmospheric model of Kurucz (1992).

which AIBs have been detected. As explained later in Sect. 5, this choice is not a limiting one.

3. Model validation

To assess the validity of our results, we address in the following subsections:

- the impact of the systematic use of theoretical photo-absorption spectra in the place of the experimental ones;
- the impact of some necessary simplifying assumptions on the relaxation channels available to the molecules; and
- the reliability of the current model, by comparing it to another independent implementation.

3.1. Use of theoretical photo-absorption spectra

To test and validate the use of the calculated absorption spectra of Mallocci et al. (2004) in the MC simulation, we compared them with the results obtained by applying the same modelling procedure to the experimental spectra of anthracene, pyrene, coronene, and ovalene (Joblin 1992; Joblin et al. 1992). For all of these molecules, the agreement between theoretical and laboratory data is reasonably good, with typical absolute errors of ~ 0.3 eV between the calculated and measured positions of the absorption bands, as expected for TD-DFT calculations (e.g. Hirata et al. 1999, 2003; Mallocci et al. 2004). In some cases these relatively small differences are widely amplified in the low-energy part of the estimated photon absorption rates for the Red Rectangle and, to a lesser extent, for the ISRF, because these RFs are very steep (see Fig. 1), i.e. the photon flux changes up to about an order of magnitude in 0.3 eV. To make sure that any differences depend *only* on the different σ adopted, we used in all cases theoretical frequencies and intensities of the vibrational bands for this comparison.

Appendix A shows in detail the comparison between the synthetic (σ_{th}) and laboratory (σ_{lab}) photo-absorption cross sections of anthracene, pyrene, coronene, and ovalene, as well as the

impact of their differences on the estimated energy-dependent absorption rates in the three RFs considered. The agreement between IR emission fluxes calculated using σ_{th} and those calculated using σ_{lab} is found to be *quantitatively* very good for all of the four molecules, the worst error being a factor of 2 for pyrene in the Red Rectangle, much better in all other cases. In all cases, *relative* intensities among IR bands appear very accurate, with differences of the order of, at most, $\sim 20\%$.

3.2. Molecular relaxation processes

The predicted IR emission spectra were derived under the assumption that the absorption of a UV-visible photon be immediately followed by one or several non-radiative transitions leaving the molecule in a highly excited vibrational level of the electronic ground-state E_0 , from which it relaxes by vibrational transitions (Allamandola et al. 1989; Leach 1995a,b). Quite generally, upon reaching E_0 , any PAH redistributes its remaining excitation energy very quickly among the accessible vibrational modes, to achieve internal thermal equilibrium (ITE). Fast intramolecular radiationless transitions ensure that ITE is efficiently established between vibrational transitions.

Since the molecule is a closed, isolated system in which energy is conserved between photon emissions or absorptions, microcanonical statistics applies to the distribution of energy among vibrational degrees of freedom in this regime. However, the rate of intramolecular transitions is a sensitive function of excitation energy, and it becomes ineffective below a molecule-specific decoupling threshold E_{dec} . Since energy gets emitted in discrete steps during relaxation, the molecule is likely to effectively jump from an excitation energy above the threshold, i.e. in ITE, to one below the threshold, in which redistribution of energy does not occur anymore. When this happens, the number of vibrational quanta in each energetically accessible mode is likely to be frozen according to microcanonical statistics at that energy. In perfect isolation conditions, all of these vibrational quanta must be emitted via radiative transitions, even if they are electric-dipole forbidden. Since the population of vibrational modes upon decoupling depends *only* on the statistics of accessible states, very low-energy modes are clearly favoured in the final redistribution of excitation energy immediately before decoupling, regardless of their IR-activity.

The dominant process competing with radiative relaxation is the absorption of another UV-visible photon before the molecule reaches the vibrational ground state. When this happens, the total available energy rises above E_{dec} again. Emission in the weakest IR bands, towards the low-energy end, essentially happens only when the stronger ones are energetically inaccessible; if vibrational cascades are interrupted, IR-inactive and weak IR-active bands are consequently suppressed, in favour of the stronger ones, which are emitted much more quickly when the molecule excitation energy is high enough. Since no data is available on the spontaneous transition rates in IR-inactive vibrational modes of PAHs and their calculation is not presently implemented in the commonly available quantum chemistry packages, we modelled them as IR-active bands with an oscillator strength equal to the average of all IR-active bands scaled down by a factor 10^4 , which yields the appropriate order of magnitude for electric quadrupole transitions. The only available direct measurements to date for the decoupling energy E_{dec} were performed on perylene and anthracene (Bouzou et al. 1983; Felker & Zewail 1984); in our model runs, we therefore chose the threshold for other PAHs by requiring the density of vibrational states to be the same as in anthracene at its measured E_{dec} ($\sim 1700 \text{ cm}^{-1}$).

In all environments considered, collisions are less frequent than photon absorption events (Omont 1986), so we neglected them in our treatment. They may play a role in populating/depopping IR-inactive modes after decoupling, when timescales between photon emission/absorption events are relatively long, especially for ions, which have larger collisional cross sections. This can be expected to become relatively more important for environments for which the ratio between gas density and UV-visible radiation density is higher. However, while not necessarily negligible, this is a higher-order correction in all cases considered here.

Immediate conversion of all excitation energy to vibrational energy in E_0 is not necessarily the only relaxation path available. Photoionisation can be relevant for neutral PAHs in the RFs considered, so we took it into account in our modelling calculating the energy-dependent yield using the analytical expression given by Le Page et al. (2001) and the experimental ionisation energies (Lias 2005). Since the RFs considered do not contain significant fluxes of photons capable of doubly ionising the PAHs considered here, we neglect ionisation for cations. The probabilities of the main dissociation channels have been estimated to be negligible for our purposes (Allain et al. 1996a,b). However, recent results with the PIRENEA experiment (Joblin et al. 2006) show that the coronene cation loses one H atom at an average excitation energy of 10.5 eV. Therefore, a fully detailed model would need to follow the photophysical and chemical evolution of a PAH population including ionisation, electron recombination, photodissociation, and reactivity, in particular with H atoms. This is outside of the scope of the present paper. In any case, as far as the IR emission spectrum is concerned, the effect of photodissociation and/or photoionisation is a higher-order correction. Indeed, the overall IR emission spectrum stems from the sum over a large number of relaxation cascades, which in this respect can be considered essentially independent, and photodissociation, photoionisation, etc., happen only in a small fraction of them.

Provided they neither ionise nor dissociate, all closed-shell (e.g. neutral, fully hydrogenated) PAHs, upon excitation from their ground electronic singlet state $S_n \leftarrow S_0$, will undergo very fast internal conversion to a low-lying singlet electronic level S_m , which is almost always S_1 (e.g. Leach 1995a,b). Afterwards, the molecule relaxes radiatively in the visible and/or in the IR. For a thorough discussion see e.g. Mulas et al. (2006b) where all the relaxation channels were modelled in detail. A short resumé is also given in Appendix B.

In open-shell PAHs (e.g. singly charged ions of fully hydrogenated species) usually both the ground D_0 and first excited D_1 electronic states are doublets and are connected by an electric dipole-permitted electronic transition (Birks 1970). In this situation, internal conversion (IC) $D_n \rightarrow D_0$, followed by vibrational transitions, is expected to always be the dominant relaxation channel (Leach 1995a,b), fluorescence and phosphorescence being negligible. Energy-dependent quantum yields for the main relaxation channels of closed-shell PAHs are known for very few molecules (Bréchnac 2005) and only IC to D_0 is important for open-shell species. Therefore, since this work aims to systematically explore the far-IR spectral fingerprint of a large sample of molecules, we chose to neglect the relaxation channels via fluorescence and phosphorescence.

To assess the impact of this simplification, the spectra presented here can be compared with those we obtained in Mulas et al. (2006b), in which we modelled all relaxation channels in full detail. In Appendix B we present such a comparison, which shows that neglecting fluorescence and phosphorescence leads

Table 2. Comparison between two sets of model runs for coronene ($C_{24}H_{12}$) in different exciting RFs. For each model run and each band, we list the absolute integrated flux and, in parentheses, the flux fraction.

Peak (μm)	ISRF		Red Rectangle		IRAS 21282+5050	
	model 1 ^a (Wsr^{-1}) (%)	model 2 ^b (Wsr^{-1}) (%)	model 1 ^a (Wsr^{-1}) (%)	model 2 ^b (Wsr^{-1}) (%)	model 1 ^a (Wsr^{-1}) (%)	model 2 ^b (Wsr^{-1}) (%)
3.26	3.8×10^{-27} (37.96)	3.9×10^{-27} (38.15)	5.8×10^{-26} (24.76)	6.3×10^{-26} (25.36)	4.3×10^{-22} (46.68)	4.2×10^{-22} (46.50)
3.29	2.6×10^{-28} (2.58)	2.6×10^{-28} (2.56)	4.0×10^{-27} (1.72)	4.2×10^{-27} (1.70)	2.9×10^{-23} (3.18)	2.9×10^{-23} (3.16)
6.24	5.2×10^{-28} (5.15)	5.4×10^{-28} (5.21)	1.3×10^{-26} (5.47)	1.4×10^{-26} (5.51)	4.6×10^{-23} (5.01)	4.5×10^{-23} (5.00)
6.69	9.2×10^{-30} (0.09)	9.7×10^{-30} (0.09)	2.4×10^{-28} (0.10)	2.6×10^{-28} (0.11)	8.0×10^{-25} (0.09)	6.9×10^{-25} (0.08)
7.21	1.1×10^{-28} (1.07)	1.1×10^{-28} (1.08)	2.8×10^{-27} (1.22)	3.1×10^{-27} (1.24)	9.1×10^{-24} (0.99)	8.8×10^{-24} (0.97)
7.63	6.6×10^{-28} (6.59)	7.0×10^{-28} (6.77)	1.7×10^{-26} (7.49)	1.9×10^{-26} (7.73)	5.5×10^{-23} (6.05)	5.5×10^{-23} (6.10)
8.25	3.0×10^{-28} (2.92)	3.0×10^{-28} (2.93)	8.0×10^{-27} (3.42)	8.7×10^{-27} (3.53)	2.4×10^{-23} (2.63)	2.4×10^{-23} (2.64)
8.78	3.1×10^{-28} (3.10)	3.3×10^{-28} (3.21)	8.8×10^{-27} (3.79)	9.5×10^{-27} (3.82)	8.8×10^{-23} (2.75)	2.5×10^{-23} (2.75)
11.57	3.4×10^{-27} (33.25)	3.5×10^{-27} (33.89)	9.9×10^{-26} (42.48)	1.1×10^{-25} (42.72)	2.6×10^{-22} (27.89)	2.5×10^{-22} (28.02)
12.43	1.1×10^{-29} (0.11)	1.1×10^{-29} (0.11)	3.3×10^{-28} (0.14)	3.7×10^{-28} (0.15)	8.0×10^{-25} (0.09)	8.3×10^{-25} (0.09)
12.90	1.6×10^{-28} (1.56)	1.6×10^{-28} (1.60)	4.7×10^{-27} (2.03)	5.3×10^{-27} (2.12)	1.2×10^{-23} (1.29)	1.2×10^{-23} (1.30)
18.21	3.9×10^{-28} (3.91)	4.1×10^{-28} (4.01)	1.2×10^{-26} (5.29)	1.3×10^{-26} (5.44)	2.8×10^{-23} (3.04)	2.8×10^{-23} (3.11)
26.20	2.8×10^{-29} (0.28)	2.3×10^{-29} (0.22)	9.7×10^{-28} (0.42)	7.8×10^{-27} (0.32)	1.8×10^{-24} (0.19)	1.5×10^{-24} (0.16)
80.60	2.4×10^{-29} (0.24)	1.6×10^{-29} (0.16)	8.4×10^{-28} (0.36)	6.0×10^{-28} (0.24)	1.0×10^{-24} (0.11)	7.6×10^{-25} (0.08)

^a Results from the present model based on Mulas (1998), neglecting the possibility of ionisation for a consistent comparison (see text);

^b Results from the corrected (see text) model of Joblin et al. (2002).

to overestimating of the absolute vibrational emission fluxes in each band by up to a factor ~ 2 in the worst case, for the high energy bands, while low energy bands are almost unaffected. This means that the calculated spectra, despite the use of σ_{th} and the neglect of relaxation channels involving fluorescence and phosphorescence, still retain their full potential to identify specific PAHs, this approximation appearing to essentially impact the accuracy of calculated column densities.

3.3. Comparison with an alternative model

The model used here is an enhanced version of the one described in Mulas (1998). As an internal consistency test, we also derived the IR emission spectra using an independent model based on Joblin et al. (2002). Such a comparison enabled us to discover and correct some implementation errors in both of them. More specifically, an incorrect distribution of vibrational levels was used in Joblin et al. (2002), and biased absolute values of IR emission band intensities were produced in Mulas et al. (2003).

The result of this comparison for neutral coronene is shown in Table 2, which clearly demonstrate that the two models are very close. For both models we assumed a decoupling energy threshold of $\sim 1200 \text{ cm}^{-1}$, following the prescription discussed in Sect. 3.2. We notice that the model used here, as previously explained, takes into account the possibility that absorption of a high-energy photon results in an ionisation instead of IR emission. Since the model by Joblin et al. (2002) does not include this possibility, for a proper comparison we deliberately excluded it in the simulations compared in Table 2. This results in a slight overestimation of emission that is larger for high-energy bands; the latter tend to be emitted when the molecule is highly excited, hence after the absorption of harder photons which, in turn, are more likely to ionise it.

The small remaining difference between the two models is probably due to the somewhat different algorithms used to estimate the density of vibrational states (DoS), namely the Beyer-Swinehart (BS, Beyer & Swinehart 1973) method in Joblin et al. (2002) and a version of the

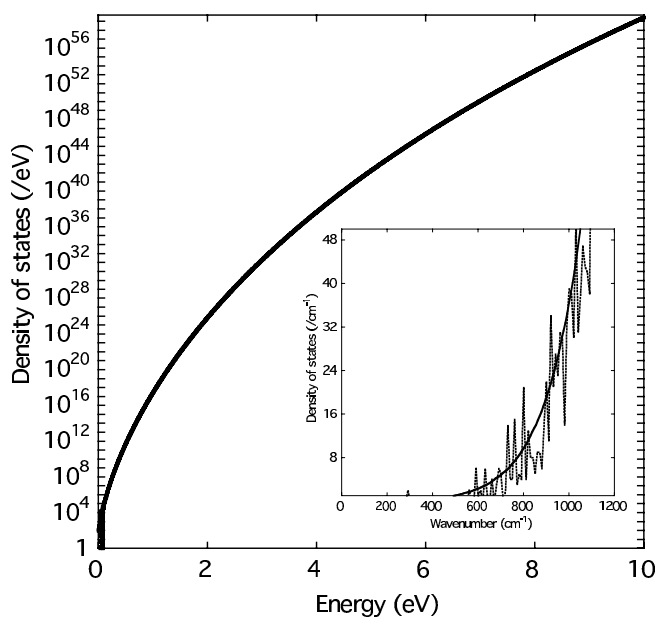


Fig. 2. Comparison between the DoS of neutral coronene computed by the current model, based on Mulas (1998) (continuous line) and that of Joblin et al. (2002) (dotted line). The DoSs are perfectly coincident for energies well above the energy of a single vibrational quantum, while they differ for very low energies.

Stein-Rabinovitch (SR, Stein & Rabinovitch 1973) method in Mulas (1998), slightly modified to ensure its continuity down to low energies. The resulting DoSs are plotted in Fig. 2, which shows them to be essentially coincident except for very low energies, where the modified SR DoS is still smooth while the BS one strongly oscillates. Such behaviour depends on the difference between the formal definition of DoS and the actual way it is calculated. For a finite system, as a large molecule, states are discrete and the DoS is thus not well-defined as a function, being instead a distribution, i.e. the sum of a collection of Dirac deltas, one for each discrete level. On the other hand, the integral of the

DoS over any finite interval still is a well-defined function. Both the BS and the SR algorithms count the number of vibrational states in a grid of finite energy intervals and obtain the DoS dividing the resulting number by the bin size. This is, therefore, not the DoS in its strict mathematical sense, but rather its average over a finite energy interval. As a consequence, the DoS thus calculated is obviously dependent on the chosen bin size, this dependence becoming very extreme for increasingly small bin sizes, when the latter becomes comparable to the spacing of the discrete levels.

The way out of this apparent formal impasse is to recognise that what is needed to calculate probabilities in the ergodic regime is *not* really the exact DoS, as to its strict mathematical definition, but rather its average over an energy range given by the Heisenberg indetermination principle. Moreover, the DoS is *only* used when the molecule is in ITE, i.e. when intramolecular radiationless transitions are fast and, as a consequence, energy indetermination is large. Therefore, we slightly modified the SR algorithm to make sure that the resulting DoS is continuous regardless of the assumed energy bin size used for calculating the density and that it converges to a well-defined limiting value for vanishingly small bin size. Essentially, this is equivalent to calculating the average of the DoS over an energy bin of the same size as a single vibrational quantum of the lowest frequency mode of the molecule.

We stress that the results of the simulations are fundamentally independent of the algorithm used: statistics tend to wash out the effect of the strong oscillations in the BS DoS. However, for smaller and smaller bin sizes, and correspondingly stronger oscillations in the DoS, increasingly long simulations are required to obtain numerical convergence. When using the explicitly smoothed DoS in the simulations, instead, numerical convergence is faster and independent of the bin size adopted for the DoS calculation.

4. Results

The whole sample of molecules investigated is shown in Fig. 2 of Mallocci et al. (2004). Table 3 summarises the resulting integrated photon absorption rates \mathcal{R} and average energies \mathcal{E} of the absorbed photons. The energy absorption rate is $\mathcal{R}\mathcal{E}$.

Our model runs produce band positions and the corresponding integrated fluxes. More specifically, the model yields the total number of photons, and hence the total power \mathcal{P} , isotropically radiated in each vibrational mode by one molecule embedded in a given RF. The dimensions of this quantity are energy per unit time per unit solid angle per molecule. The statistical error on the number of photons is Poissonian, therefore the purely statistical contribution to errors can be made negligible by extending the length of the model runs. This is typically achieved simulating $\sim 10^4$ photon absorption events and the following de-excitation cascades. The accuracy of our model results is limited by that of the level of theory we used to perform the vibrational analyses. Our calculated positions of far-IR vibrational bands compare rather favourably with the sparse experimental measurements available (see Table 1). As to the calculated Einstein coefficients for spontaneous emission in the IR bands, a comparison between gas-phase measurements of band intensities (Joblin et al. 1994, 1995a) and DFT calculations at the level of theory we used here (Langhoff 1996) show differences that range from $\sim 10\%$ to a factor of 2 for single bands. The largest discrepancy is found for the high frequency in-plane C–H stretch modes, with generally better agreement for the other modes. To the best of our knowledge, with the exception of the works by Zhang et al. (1996),

Pirali (2004), and Pirali et al. (2006), there are no other gas-phase laboratory data available for far-IR bands of our sample of PAHs. More experimental work is therefore definitely needed for a systematic assessment of their accuracy and reliability.

Tables C.1 to C.40 in Appendix C list the calculated far-IR emission spectra of all 20 PAHs considered and of their cations. In such tables permitted transitions are distinguished between parallel and perpendicular, depending on the direction of the electric dipole transition moment with respect to the plane of the molecule. In addition, we explicitly mark electric dipole forbidden bands.

Moreover, no data are available, to the best of our knowledge, on the intensity of bands which are IR-inactive in the harmonic electric-dipole approximation. Further experimental and theoretical work on these bands is needed for an accurate assessment of the photon absorption rates below which each electric-dipole-forbidden band might be emitted efficiently.

We assumed 100% efficient conversion of absorbed energy to IR emission, overestimating our calculated fluxes for closed-shell species (see Sect. 3), very slightly in the case of far-IR bands. This only marginally affects the diagnostic capability of the calculated spectra, i.e. the possibility of using them to identify specific PAHs upon comparison with astronomical observations, but instead affects the accuracy of column density (limits) derived using them. This is not an issue for open-shell species.

Overall, as a conservative estimate, we expect our absolute estimated far-IR fluxes to be accurate within a factor of 2 and our band positions within better than $\sim 2\%$.

5. Discussion

The results in Appendix C show the diagnostic potential of far-IR observations for the identification of *specific* PAHs. All the molecules in our sample, in the RFs considered, exhibit a few relatively strong IR-active bands that dominate its far-IR spectrum. These bands, in most cases flopping modes of the whole molecule, strongly depend on its size and shape and on the rigidity of its bonds. This latter dependence usually makes the far-IR spectrum of each cation distinguishable from that of its parent neutral, even if similar to it.

For each species the IR emission spectrum expected for the RF of the Red Rectangle halo is considerably “colder” than the one expected for the ISM, which in turn is “colder” than that in the PDR of IRAS 21282+5050; i.e. a larger and larger flux fraction is emitted in higher energy bands going from the first to the last. This is just the effect of the spectral energy distribution of the exciting RF, which in the Monte-Carlo simulations translates to a higher average excitation energy \mathcal{E} of the molecules (see Table 3). Another similar trend seen there is that the IR emission spectrum of larger molecules is “colder”, in the same sense as above, than that of smaller ones in the same RF. Again, this is expected due to the larger number of vibrational degrees of freedom for increasing number of atoms.

An interesting result of our simulations is the prediction of non-negligible emission in far-IR electric-dipole forbidden vibrational transitions. Such emission is essentially the excitation energy remaining “trapped” in IR-inactive modes at the end of the vibrational cascade following UV-visible absorption. In perfect isolation conditions, this energy has no other way out than to be slowly emitted via forbidden or very weakly-permitted vibrational transitions. The absorption of an additional UV-visible photon by the molecule before it can emit the energy trapped in its IR-inactive modes effectively quenches the emission of far-IR photons. Hence emission in an IR-inactive mode only occurs if

Table 3. Integrated photon absorption rates \mathcal{R} (s^{-1}) and average absorbed energy \mathcal{E} (eV), computed using calculated photo-absorption cross-sections (Mallocci et al. 2004) for the whole sample of 20 neutral PAHs and their cations in the three RFs considered.

Molecule	Charge state	Radiation field					
		ISRF		Red Rectangle		IRAS 21282+5050	
		\mathcal{R} (s^{-1})	\mathcal{E} (eV)	\mathcal{R} (s^{-1})	\mathcal{E} (eV)	\mathcal{R} (s^{-1})	\mathcal{E} (eV)
Naphthalene (C ₁₀ H ₈)	Neutral	3.9×10^{-8}	7.9	5.7×10^{-7}	5.6	3.8×10^{-3}	8.9
	Cation	6.6×10^{-8}	4.7	3.1×10^{-6}	2.8	3.1×10^{-3}	9.0
Fluorene (C ₁₃ H ₁₀)	Neutral	5.2×10^{-8}	7.8	8.9×10^{-7}	5.2	4.9×10^{-3}	9.2
	Cation	1.3×10^{-7}	4.0	6.7×10^{-6}	2.7	4.1×10^{-3}	9.2
Anthracene (C ₁₄ H ₁₀)	Neutral	6.4×10^{-8}	6.8	2.5×10^{-6}	4.0	5.2×10^{-3}	8.6
	Cation	1.7×10^{-7}	3.4	8.5×10^{-6}	2.5	4.4×10^{-3}	8.6
Phenanthrene (C ₁₄ H ₁₀)	Neutral	5.6×10^{-8}	7.4	1.1×10^{-6}	5.1	5.1×10^{-3}	8.8
	Cation	1.7×10^{-7}	3.2	9.1×10^{-6}	2.3	4.3×10^{-3}	8.8
Pyrene (C ₁₆ H ₁₀)	Neutral	8.1×10^{-8}	6.4	3.7×10^{-6}	3.8	5.7×10^{-3}	8.6
	Cation	1.4×10^{-7}	4.0	9.2×10^{-6}	2.7	4.9×10^{-3}	8.6
Fluoranthene (C ₁₆ H ₁₀)	Neutral	7.6×10^{-8}	6.8	3.2×10^{-6}	3.8	6.0×10^{-3}	8.9
	Cation	2.4×10^{-7}	3.0	1.3×10^{-5}	2.2	5.1×10^{-3}	8.8
Tetracene (C ₁₈ H ₁₂)	Neutral	1.3×10^{-7}	5.4	5.8×10^{-6}	3.5	6.8×10^{-3}	8.4
	Cation	3.7×10^{-7}	2.8	1.9×10^{-5}	2.2	6.0×10^{-3}	8.4
Chrysene (C ₁₈ H ₁₂)	Neutral	8.6×10^{-8}	6.7	2.9×10^{-6}	4.3	6.7×10^{-3}	8.7
	Cation	4.6×10^{-7}	2.2	3.0×10^{-5}	1.6	5.9×10^{-3}	8.7
Perylene (C ₂₀ H ₁₂)	Neutral	1.7×10^{-7}	4.6	1.0×10^{-5}	2.9	7.1×10^{-3}	8.7
	Cation	2.3×10^{-7}	3.7	1.4×10^{-5}	2.6	6.2×10^{-3}	8.6
Pentacene (C ₂₂ H ₁₄)	Neutral	1.6×10^{-7}	5.4	7.2×10^{-6}	3.8	8.2×10^{-3}	8.3
	Cation	7.2×10^{-7}	2.3	4.3×10^{-5}	2.0	7.5×10^{-3}	8.2
Benzo[g,h,i]perylene (C ₂₂ H ₁₂)	Neutral	1.3×10^{-7}	5.8	7.0×10^{-6}	3.4	7.8×10^{-3}	8.5
	Cation	2.8×10^{-7}	3.3	1.6×10^{-5}	2.4	6.9×10^{-3}	8.4
Anthanthrene (C ₂₂ H ₁₂)	Neutral	1.7×10^{-7}	4.9	1.1×10^{-5}	3.1	7.9×10^{-3}	8.4
	Cation	3.2×10^{-7}	3.1	2.0×10^{-5}	2.3	7.1×10^{-3}	8.4
Coronene (C ₂₄ H ₁₂)	Neutral	1.3×10^{-7}	6.2	4.5×10^{-6}	4.1	8.5×10^{-3}	8.5
	Cation	3.1×10^{-7}	3.3	1.6×10^{-5}	2.4	7.6×10^{-3}	8.4
Dibenzo[cd,lm]perylene (C ₂₆ H ₁₄)	Neutral	4.6×10^{-7}	3.0	4.0×10^{-5}	1.9	9.5×10^{-3}	8.5
	Cation	4.5×10^{-7}	3.1	2.8×10^{-5}	2.5	8.4×10^{-3}	8.4
Bisanthene (C ₂₈ H ₁₄)	Neutral	5.1×10^{-7}	2.7	2.5×10^{-5}	2.0	9.9×10^{-3}	8.5
	Cation	5.7×10^{-7}	2.5	3.6×10^{-5}	1.7	9.0×10^{-3}	8.4
Terrylene (C ₃₀ H ₁₆)	Neutral	7.7×10^{-7}	2.7	3.9×10^{-5}	2.1	1.1×10^{-2}	8.6
	Cation	9.6×10^{-7}	2.4	4.8×10^{-5}	2.0	1.0×10^{-2}	8.6
Ovalene (C ₃₂ H ₁₄)	Neutral	2.8×10^{-7}	4.6	2.0×10^{-5}	3.1	1.1×10^{-2}	8.2
	Cation	5.5×10^{-7}	2.9	3.8×10^{-5}	2.2	1.1×10^{-2}	8.2
Circumbiphenyl (C ₃₈ H ₁₆)	Neutral	3.1×10^{-7}	4.7	2.7×10^{-5}	3.1	1.3×10^{-2}	8.2
	Cation	8.7×10^{-7}	2.4	6.9×10^{-5}	1.9	1.2×10^{-2}	8.2
Quaterrylene (C ₄₀ H ₂₀)	Neutral	2.2×10^{-6}	2.0	1.1×10^{-4}	1.7	1.5×10^{-2}	8.6
	Cation	2.7×10^{-6}	1.9	1.4×10^{-4}	1.6	1.4×10^{-2}	8.5
Dicoronylene (C ₄₈ H ₂₀)	Neutral	8.8×10^{-7}	3.2	5.8×10^{-5}	2.6	1.7×10^{-2}	8.1
	Cation	2.2×10^{-6}	2.0	1.5×10^{-4}	1.6	1.6×10^{-2}	8.0

its time scale is shorter than, or at least comparable to, the rate of UV-visible photon absorption. Such conditions are by and large met in the ISRF, in which the calculated fluxes in such bands can be comparable to the lowest-energy permitted ones. In the Red Rectangle halo, on the other hand, the radiation density is high enough to make the absorption of another UV-visible photon happen on a timescale comparable to that of the emission of photons in IR-inactive modes, which is reduced. In the PDR of IRAS 21282+5050, the absorption of UV-visible photons completely dominates the emission in all weak IR bands, essentially suppressing them. An increase in molecular size produces the same effect, described above, of an increase in RF intensity; this happens because the photo-absorption cross-sections and, consequently, the photon absorption rates \mathcal{R} , scale roughly with the

number of carbon atoms in the molecule (Joblin 1992; Joblin et al. 1992), while the total IR emissivity at the low-energy end does not scale in the same way for this sample of molecules.

Quite generally, emission in far-IR bands can be divided into three different regimes, depending only on the photon absorption rate:

1. for very dilute RFs, e.g. in the diffuse ISM, a molecule always has time to completely relax after each photon absorption, and consequently the fluxes in *all* far-IR bands scale linearly with the photon absorption rate;
2. for intermediate RFs, e.g. in the Red Rectangle halo, a molecule always has time to emit all quanta in IR-active modes, but absorbs another photon before being able to

completely relax IR-inactive modes; hence, fluxes in IR-active bands still scale linearly with the photon absorption rate, while some emission in electric-dipole forbidden bands is suppressed;

3. for very strong RFs, e.g. in the PDR of IRAS 21282+5050, a molecule is always vibrationally “warm”, since photon absorption events are very frequent, and it almost never reaches the bottom of its IR emission cascade; as a result, *all* weak IR bands tend to be progressively suppressed in favour of the stronger ones (i.e. classical AIBs).

The boundaries between these regimes will depend on the molecule, since different molecules will have different photon absorption rates in the same RF.

Within the same regime, far-IR fluxes scale linearly with the dilution of the RF adopted, which means that the data we present here cover a relatively wide range of environments. For example, the ISRF estimated by Draine (1978) is very similar to the interstellar RF we used, with just a different dilution factor; the former has an intensity in Habing units of $G_1 \approx 1.68 G_0$ (Weingartner & Draine 2001), while the latter corresponds to $G_2 \approx 3.49 G_0$; therefore, the expected far-IR spectrum for the Draine ISRF can be obtained simply by multiplying the fluxes we calculated by the ratio $G_1/G_2 \approx 0.48$. As another example, the RF in the Orion Bar is very similar to the one of IRAS 21282+5050, with a ~ 10 -fold relative dilution, so the expected far-IR spectrum for the Orion Bar can be obtained as a first-order approximation, by dividing the fluxes we calculated for IRAS 21282+5050 by a factor of 10.

The PAH emission in IR-inactive modes, if detectable, will provide a powerful probe both of the absolute intensity of the RF the emitting molecule is embedded in and of some poorly-known molecular parameters (Joblin et al. 2002; Mallocci et al. 2003; Mulas et al. 2003, 2006b). However, as a cautionary remark, we recall that in the absence of any information on the intensity of electric-dipole forbidden vibrational bands, in the model we made the simplification of considering them as electric-dipole permitted bands with an oscillator strength 10^4 times smaller than the average IR-active bands. Therefore, while both the asymptotic results calculated for the ISRF (perfect isolation) and for the PDR of IRAS 21282+5050 (complete suppression) are expected to be correct, as well as the general trends predicted, accurate quantitative results for intermediate cases will require either the measurement or the calculation of IR-inactive band intensities. On the plus side, the impact of this uncertainty on the accuracy of fluxes in IR-active bands is by and large negligible in all cases.

For comparison with observational data, in the optically thin case, the spectra we presented here must be multiplied by the assumed column density and the result integrated over the instrumental aperture on the sky for extended sources. A detailed radiative transfer analysis is needed for the optically thick case. We previously performed such a comparison for three small, neutral PAHs in the Red Rectangle (Mulas et al. 2006b) and, in this case, found the expected band intensities to be well within the sensitivity of available Infrared Space Observatory (ISO) data. This example clearly demonstrated the discriminating capabilities of our synthetic spectra with presently available ISO observations and even more so for the forthcoming HSO mission, which is expected to go about two orders of magnitude deeper than ISO in the far-IR.

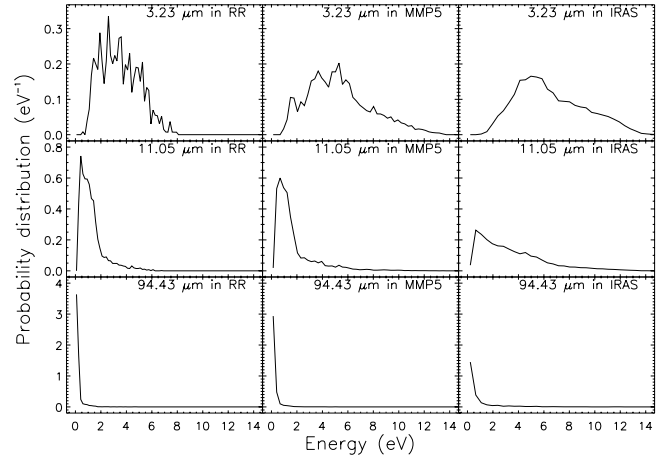


Fig. 3. Distribution of the excitation energies at which photons are emitted by neutral bisanthene in three RFs and three vibrational bands.

5.1. Detectability

To assess the possibility of identifying specific interstellar PAHs in a large population of species, we computed the spectrum of a weighted sum of all the species in our sample, using the inverse of the number of carbon atoms in each molecule as its weight, i.e.

$$I_{\lambda}^{\text{tot}} = k \sum_{\text{PAH}} \frac{1}{N_{\text{C}}(\text{PAH})} I_{\lambda}^{\text{PAH}}, \quad (1)$$

the summation being over all molecules and charge states in our sample and the single spectra calculated for the Red Rectangle halo; k is a normalisation constant which is defined later.

To assess the problem of detectability, some assumption on band shapes had to be made. One major cause of band broadening is the overlap of many nearly degenerate vibrational modes due to different occurrences of the same chemical bond in the molecule, such as e.g. out-of-plane C–H bends. This is automatically taken into account in our model, which calculates separate expected fluxes for all bands, regardless of their near degeneracy.

Another cause of broadening is anharmonicity: almost all emitted photons are not due to a transition from a state in which one single vibrational mode was singly excited to the ground state, but from highly excited states. As an example, Figs. 3 and 4 show the distribution of the number of photons emitted in three vibrational modes as a function of the excitation energy of neutral and cationic bisanthene ($\text{C}_{28}\text{H}_{14}$), a medium-sized molecule of our sample, in the three modelled RFs.

Figures 5 and 6 show the distribution of the number of photons emitted in the same three specific vibrational modes as a function of the excitation energy in that specific vibrational mode. As described in detail by Oomens et al. (2003), the peak position of the bands is a function of vibrational energy (i.e. cross-anharmonic shifts) and quantum number (i.e. anharmonic shifts) of the emitting vibrational mode. Knowledge of these molecular parameters, together with the distributions in energy and quantum number (i.e. Figs. 3 to 6), would enable one to derive the effect of anharmonicity on band shape for each band.

Furthermore, intramolecular energy redistribution is extremely effective at high excitation energies and causes strong lifetime broadening. The rate of radiationless transitions causing intramolecular energy redistribution is known to be a steep function of molecular vibrational excitation energy. Thus again, in principle, if this function were known, this broadening might

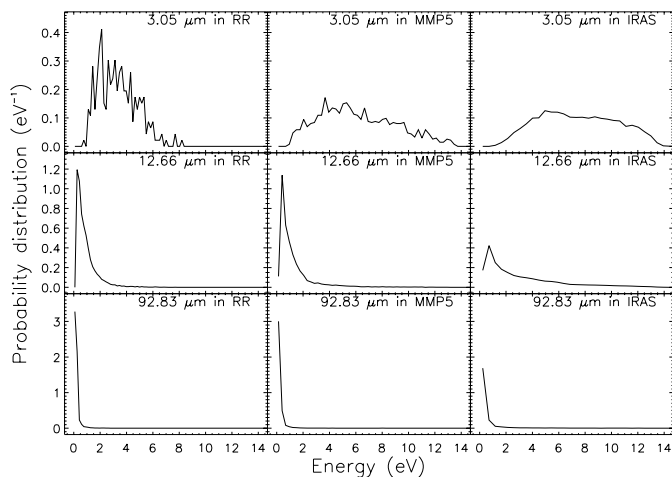


Fig. 4. Like Fig. 3 for the bisanthene cation.

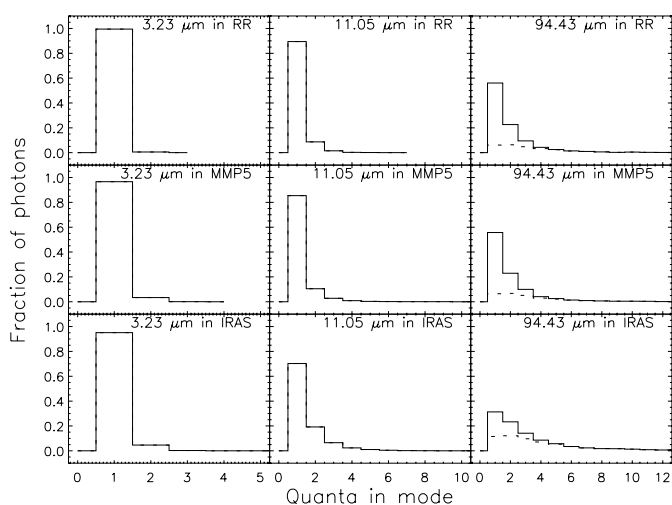


Fig. 5. Distribution of the photons emitted by neutral bisanthene in three RFs and three vibrational bands as a function of the vibrational excitation quanta in the mode.

be estimated from the distribution of energies of the emitting molecules. In the case of the lowest frequency modes, lifetime broadening becomes negligible, since they tend to be emitted below or only slightly above the decoupling energy E_{dec} .

We performed a completely detailed calculation of anharmonic and lifetime broadening effects on band shape for the C–H stretching modes near $3.3 \mu\text{m}$ for neutral anthracene, phenanthrene, and pyrene in the Red Rectangle (Mulas et al. 2006b), using experimental data (Joblin et al. 1995a; Pech et al. 2002). Since the molecular parameters required for this are only available for very few bands of very few species, we did not include this effect in our present calculations.

Finally, far-IR bands are expected to show rotational profiles. The population of rotational levels, for isolated PAHs in space, is probably far from thermal equilibrium (Rouan et al. 1992; Le Coupanec et al. 1998, 1999). While our modelling approach can be extended to estimate this precisely, this implies a huge increase in computational costs, with a factor of the order of the number of rotational levels to be traced (i.e. $\sim 10^5$). It also requires the detailed knowledge of more molecular parameters (e.g. the matrix of vibration-rotation constants and anharmonic vibrational parameters, Barone 2005), which are not readily available for our sample and far from trivial to

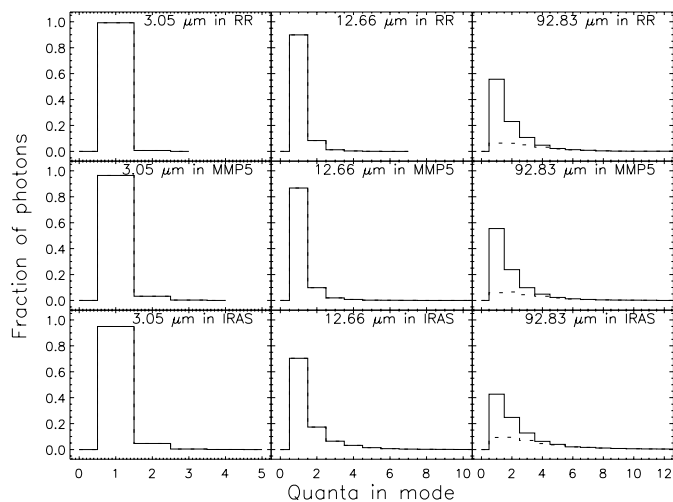


Fig. 6. Like Fig. 5 for the bisanthene cation.

calculate. We performed such a complete calculation for two of the smallest neutral PAHs in our sample, namely naphthalene and anthracene, as a test case (Mulas et al. 2006a). For the present paper, we simulated rotational profiles by including, for each band, two relatively broad Gaussians, displaced by their width σ_{PR} on either side of the calculated band origin, representing P and R branches and, for perpendicular bands, a narrower Gaussian of width σ_{Q} representing the central Q branch. A fraction of $\sim 20\%$ of the flux in the band was assigned to the Q branch, when present, the remaining split evenly between the P and R branches. Real values will deviate possibly by a factor of ~ 2 from this. The population of levels between different values of the quantum number J of the total angular momentum is qualitatively expected to follow a pseudo-thermal distribution (Rouan et al. 1992), its pseudo-temperature scaling with the average energy of the emitted IR photons. The parameter σ_{PR} in our approximate representation of the P and R branches scales with the square root of this pseudo-temperature, since they involve transitions between states of different J (see e.g. Cami et al. 2004).

A c-type² band of a planar molecule such as a PAH will generally exhibit a sharp central Q branch since, in the rigid rotor approximation, all the transitions composing it are coincident in energy if the rotational constants do not change between the two vibrational states involved (Herzberg 1991). For this class of molecules, the fractional variation in rotational constants due to vibrational excitation is usually of the order of $\sim 10^{-4}$, arriving at most to $\sim 10^{-2}$ in the infrequent case of accidental near degeneracy, giving rise to very strong Coriolis perturbations (Herzberg 1991; Mulas et al. 2006a). The transitions in the Q branch, by definition, connect states with the same J . The relative population of levels with the same J , due to internal vibration-rotation energy transfer (IVRET Rouan et al. 1992) remains in thermal equilibrium with the bath of vibrational states down to the decoupling energy. This means that the relative population of levels

² IR-permitted bands are labelled according to the direction of the change of the electric dipole moment in the involved vibrational mode, in relation to the axes of the principal momenta of inertia (I_i , with $i = x, y, z$) of the molecule. These axes, and the corresponding rotational constants and transition types, are labelled in order of increasing I_i . A c-type band therefore corresponds to a transition in which the electric dipole moment changes along the direction of maximum momentum of inertia, which for planar molecules is always perpendicular to the symmetry plane (Herzberg 1991).

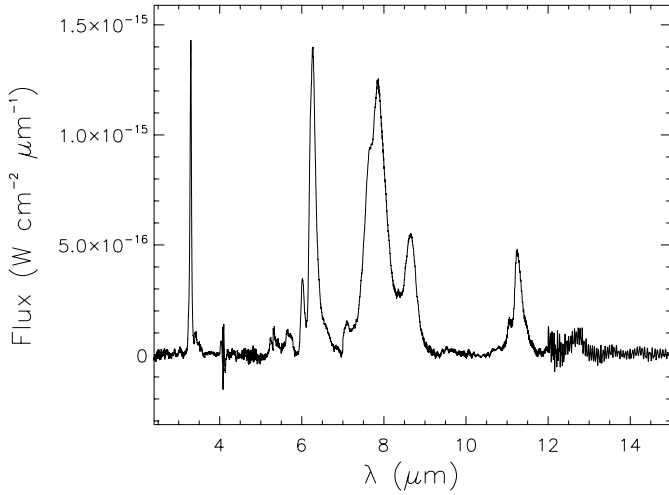


Fig. 7. Continuum-subtracted AIBs spectrum of the Red Rectangle, from the online ISO spectral database.

with the same J will reflect the excitation of the molecule when each photon gets emitted. Since low-energy photons are emitted near the end of the relaxation cascades, the latter distribution will be very “cold” for them. This “cold” relative population of levels and the almost unchanged rotational constants in the transition conspire to produce Q branches that are very much sharper than the corresponding P and R branches.

In the absence of reliable estimates in this respect, we had to assume a starting point from which to apply the above scaling relations. We took $0.7 \text{ cm}^{-1} \leq \sigma_{\text{PR}} \leq 5.5 \text{ cm}^{-1}$ for neutral naphthalene, which amounts to pseudo-temperatures in J , calculated according to the recipe in Cami et al. (2004), between $\sim 10 \text{ K}$ (highly subthermal) and $\sim 500 \text{ K}$ (highly suprathedral). Any realistic value for the environments considered ought to fall in this wide range.

For σ_{Q} , the profile of Q branches will be blurred by anharmonic effects, which are expected to perturb the energy of the transition by a fractional amount of less than 1%, essentially of the same order as the empirical correction factors (i.e. ~ 0.96 in this case) commonly used to account for anharmonicity, bringing harmonic frequencies into near coincidence with experimental values.

For a direct comparison with present and forthcoming observations, we chose the normalisation factor k in the definition of I_{λ}^{tot} (see Eq. (1)) by requiring that its integral between 3 and $14 \mu\text{m}$ be equal to the integral, over the same wavelength interval, of the observed ISO-SWS spectrum of the AIBs in the Red Rectangle. This spectrum, taken from the online ISO database, is reproduced after continuum subtraction in Fig. 7 for reference. Our synthetic summed spectrum is shown in Fig. 8. The same figure also shows the estimated dust continuum in the Red Rectangle, obtained by extrapolating the long wavelength tail of the observed continuum in available ISO-LWS observations of the same source with a grey body spectrum in the Rayleigh-Jeans approximation (see Fig. 9), given (in $\text{W cm}^{-2} \mu\text{m}^{-1}$) by $I_{\lambda}^{\text{dust}} = A \lambda^{-\beta}$, with $A = 8.14 \times 10^{-12}$, $\beta = 3.31$ and λ in μm . This extrapolation is consistent with the spectral energy distribution previously obtained by detailed modelling in Men’shchikov et al. (2002).

The molecules in our sample are likely not to be the interstellar population, as the mid-IR spectra of the mixtures show some difference with the interstellar spectra. Nonetheless, this combined spectrum serves the intended purpose of getting a visual

estimate of the density of bands and, hence, of probable spectral congestion as a function of wavelength.

In almost all assumed conditions, P and R branches tend to blend in a structureless continuum, from which Q branches of perpendicular bands stand out more or less clearly depending on their assumed width. Indeed, the main obstacle to the detection and identification of these bands is probably not posed by their absolute fluxes, but rather by spectral congestion and spectral contrast against a strong background continuum.

We conclude that a-type and b-type bands of PAHs, which display no sharp Q branches, will probably remain unobservable for the foreseeable future. On the other hand, the Q branches of some c-type bands, for some specific molecules, might turn out to be observable, if molecular parameters conspire to make them narrow enough. More theoretical and experimental work will be needed to find the most promising candidates in this zoo of possible species.

The density of bands decreases with the wavelength. The search for such bands therefore appears favoured at $\lambda > 100\text{--}200 \mu\text{m}$. The decrease in the dust continuum towards the millimetre range will make the detection of the bands easier. Indeed, Fig. 8 shows that, under the most favourable combination of molecular parameters, most of the bands in our sample at wavelengths beyond $\sim 120 \mu\text{m}$ are calculated to have peak intensities over 10% of the estimated dust continuum, a few of them even exceeding it. Since our sample does not reproduce the actual population of interstellar PAHs, chemical diversity will dilute the peak intensity of individual bands by an unknown factor, especially if this population is evenly spread over a vast number of different species. Chemical diversity is produced by many concurrent causes, e.g. different carbon skeletons, inclusion of heteroatoms, substitution of hydrogen atoms at the edges by different functional groups, isotopic substitutions, and different hydrogenation and/or charge states. Le Page et al. (2001, 2003) show that the population of a given PAH in any given environment is expected to be dominated by one or two ionisation and hydrogenation states, depending on its size and physical conditions. Mulas et al. (2003) showed the effect of the most likely isotopic substitutions on low-energy bands to be extremely small in the test case of ovalene, which makes it negligible in the present context. Among the other causes of diversity we mentioned above, chemical selection effects will favour the stablest species over the others, so that the most abundant of them *may* be detectable in the far-IR. Dedicated laboratory experiments, based on tentative identifications, will be needed to say the final word.

The ideal tool for this difficult quest could be HSO, with its combined sensitivity and spectral resolving power in the far-IR. The target of choice for such a search would be a source with the following properties:

- it should be a known powerful source of the AIBs;
- it should be an environment with mild excitation conditions, i.e. with not too strong a far-UV RF (to avoid a “hot” dust continuum) but with enough near-UV photons to effectively excite PAH emission.

The above description clearly fits carbon-rich circumstellar environments, such as the Red Rectangle, as well as some relatively bright photon-dominated regions (e.g. the Orion Bar). On

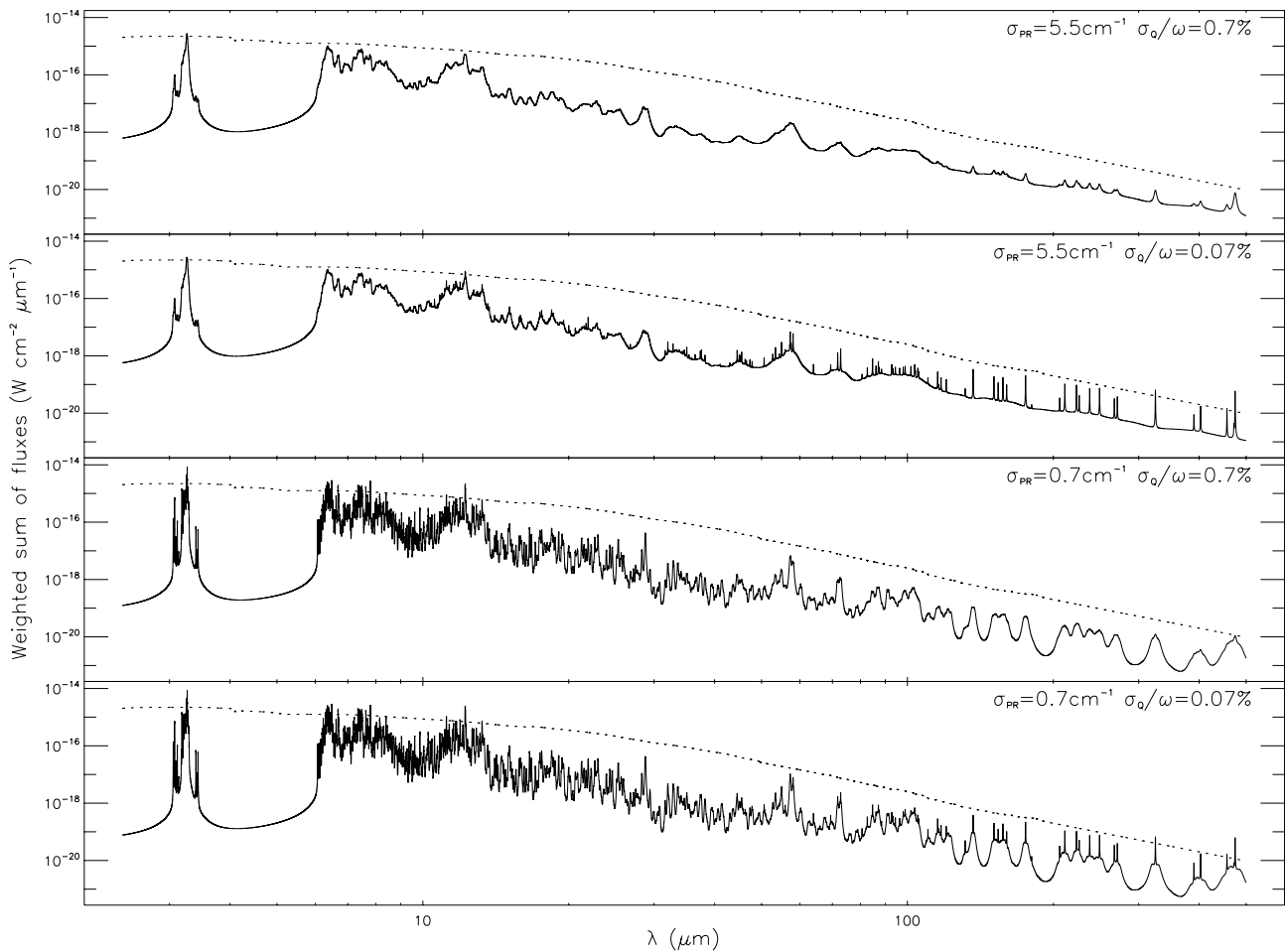


Fig. 8. Weighted sum of the spectra of all PAHs in our sample, calculated for the Red Rectangle halo (see text for its exact definition). The dotted line shows, for comparison, the estimated dust continuum in the same source. Different panels correspond to different assumptions of rotational excitations and anharmonic widths of the bands. The axes are in logarithmic scale, wavelength in abscissa, and flux in ordinate.

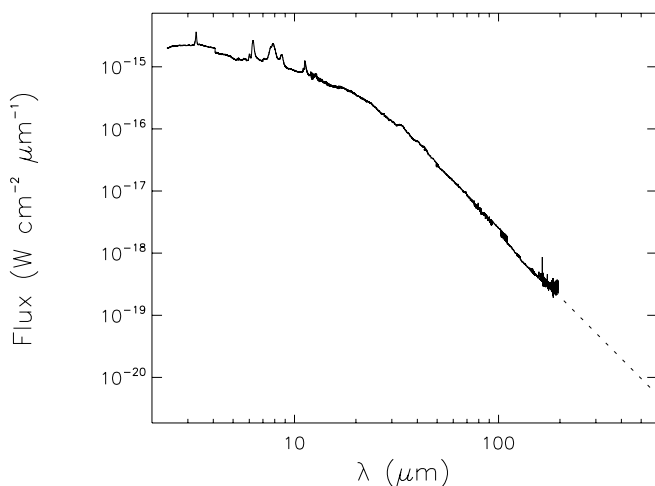


Fig. 9. ISO SWS and LWS spectrum of the Red Rectangle, showing the extrapolated dust continuum to long wavelengths (dotted line).

the other hand, neither the diffuse ISM (too weak AIBs) nor Planetary Nebulae (too strong far-UV flux) would be among the best targets.

Acknowledgements. G. Mallocci acknowledges the “Ministère de la Recherche” and G. Mulas thanks the CNRS for the financial support during their stay at CESR in Toulouse. We are thankful to the authors of OCTOPUS for

making their code available under a free license. We acknowledge the High Performance Computational Chemistry Group for using their code: “NWChem, A Computational Chemistry Package for Parallel Computers, version 4.7” (2005), PNNL, Richland, Washington, USA. Part of the calculations used here were performed using the CINECA supercomputing facility. We thank the referee for his comments, which helped improve this paper.

References

- Allain, T., Leach, S., & Sedlmayr, E. 1996a, *A&A*, 305, 602
 Allain, T., Leach, S., & Sedlmayr, E. 1996b, *A&A*, 305, 616
 Allamandola, L. J., Tielens, A. G. G. M., & Barker, J. R. 1985, *ApJ*, 290, L25
 Allamandola, L. J., Tielens, G. G. M., & Barker, J. R. 1989, *ApJS*, 71, 733
 Allamandola, L. J., Hudgins, D. M., & Sandford, S. A. 1999, *ApJ*, 511, L115
 Bakes, E. L. O., Tielens, A. G. G. M., & Bauschlicher, C. W. 2001a, *ApJ*, 556, 501
 Bakes, E. L. O., Tielens, A. G. G. M., Bauschlicher, C. W., Hudgins, D. M., & Allamandola, L. J. 2001b, *ApJ*, 560, 261
 Barone, V. 2005, *J. Chem. Phys.*, 122, 014108
 Bauschlicher, C. W., & Langhoff, S. R. 1997, *Spectrochimica Acta Part A*, 53, 1225
 Becke, A. D. 1993, *J. Chem. Phys.*, 98, 5648
 Beyer, T., & Swinehart, D. F. 1973, *Communications of the Association for Computing Machinery*, 16, 379
 Biennier, L., Salama, F., Allamandola, L. J., & Scherer, J. J. 2003, *J. Chem. Phys.*, 118, 7863
 Biennier, L., Salama, F., Gupta, M., & O’Keefe, A. 2004, *Chem. Phys. Lett.*, 387, 287
 Birks, J. B. 1970, *Photophysics of Aromatic Molecules* (London: Wiley-Interscience)
 Bouzou, C., Jouvét, C., & Leblond, J. B. 1983, *Chem. Phys. Lett.*, 97, 161

- Bréchnignac, P. 2005, private communication
- Bréchnignac, P., & Pino, T. 1999, *A&A*, 343, L49
- Cami, J., Salama, F., Jiménez-Vicente, J., Galazutdinov, G. A., & Krelowski, J. 2004, *ApJ*, 611, L113
- Cook, D. J., & Saykally, R. J. 1998, *ApJ*, 493, 793
- Crawford, M. K., Tielens, A. G. G. M., & Allamandola, L. J. 1985, *ApJ*, 293, L45
- Draine, B. T. 1978, *ApJS*, 36, 595
- Draine, B. T. 2003, *ARA&A*, 41, 241
- Duley, W. W., & Williams, D. A. 1981, *MNRAS*, 196, 269
- Ehrenfreund, P., & Charnley, S. B. 2000, *ARA&A*, 38, 427
- Ehrenfreund, P., Cami, J., Jiménez-Vicente, J., et al. 2002, *ApJ*, 576, L117
- Felker, P. M., & Zewail, A. H. 1984, *Chem. Phys. Lett.*, 108, 303
- Frish, M. J., Pople, J. A., & Binkley, J. S. 1984, *J. Chem. Phys.*, 80, 3265
- Herbig, G. H. 1995, *ARA&A*, 33, 19
- Herzberg, G. 1991, *Infrared and Raman Spectra of Polyatomic Molecules*, Vol. 2 of Molecular Spectra and Molecular Structure (Krieger Drive, Malabar, Florida: Krieger Publishing Company)
- Hirata, S., Lee, T., & Head-Gordon, M. 1999, *J. Chem. Phys.*, 111, 8904
- Hirata, S., Head-Gordon, M., Szczepanski, J., & Vala, M. 2003, *J. Phys. Chem.*, A, 107, 4940
- Hudgins, D. M., Bauschlicher, C. W., & Allamandola, L. J. 2001, *Spectrochimica Acta Part A*, 57, 907
- Joblin, C. 1992, Ph.D. Thesis, Université Paris 7
- Joblin, C., Léger, A., & Martin, P. 1992, *ApJ*, 393, L79
- Joblin, C., D'Hendecourt, L., Leger, A., & Defourneau, D. 1994, *A&A*, 281, 923
- Joblin, C., Boissel, P., Leger, A., D'Hendecourt, L., & Defourneau, D. 1995a, *A&A*, 299, 835
- Joblin, C., Salama, F., & Allamandola, L. 1995b, *J. Chem. Phys.*, 102, 9743
- Joblin, C., Toubanc, D., Boissel, P., & Tielens, A. G. G. M. 2002, *Molecular Phys.*, 100, 3595
- Joblin, C., Toubanc, D., Pech, C., et al. 2006, submitted
- Kurucz, R. 1992, in *The Stellar Populations of Galaxies*, ed. B. Barbuy, & A. Renzini (Kluwer Academic Publishers, Dordrecht), 225
- Langhoff, S. R. 1996, *J. Phys. Chem.*, 100, 2819
- Le Coupanec, P., Rouan, D., & Leger, A. 1998, *A&A*, 338, 217
- Le Coupanec, P., Rouan, D., Moutou, C., & Léger, A. 1999, *A&A*, 347, 669
- Le Page, V., Snow, T. P., & Bierbaum, V. M. 2001, *ApJS*, 132, 233
- Le Page, V., Snow, T. P., & Bierbaum, V. M. 2003, *ApJ*, 584, 316
- Leach, S. 1995a, *Planet. Space Sci.*, 43, 1153
- Leach, S. 1995b, in *The Diffuse Interstellar Bands*, ed. A. G. G. M. Tielens, & T. P. Snow, *Astrophysics and Space Science Library*, Vol. 202 (Dordrecht: Kluwer Academic Publishers), 281
- Léger, A., & Puget, J. L. 1984, *A&A*, 137, L5
- Léger, A., & d'Hendecourt, L. 1985, *A&A*, 146, 81
- Léger, A., d'Hendecourt, L., & Defourneau, D. 1989, *A&A*, 216, 148
- Lias, S. 2005, in *NIST Chemistry WebBook*, NIST Standard Reference Database Number 69, ed. P. J. Linstrom, & W. G. Mallard (Gaithersburg MD: NIST - <http://webbook.nist.gov>)
- Malloci, G., Mulas, G., & Benvenuti, P. 2003, *A&A*, 410, 623
- Malloci, G., Mulas, G., & Joblin, C. 2004, *A&A*, 426, 105
- Malloci, G., Joblin, C., & Mulas, G. 2006, *Chem. Phys.*, submitted
- Marques, M. A. L., & Gross, E. K. U. 2004, *Ann. Rev. Phys. Chem.*, 55, 3425
- Marques, M. A. L., Castro, A., Bertsch, G. F., & Rubio, A. 2003, *Comput. Phys. Commun.*, 151, 60
- Martin, J. M. L., El-Yazal, J., & Francois, J. 1996, *J. Phys. Chem.*, 100, 15358
- Mathis, J. S., Mezger, P. G., & Panagia, N. 1983, *A&A*, 128, 212
- Men'shchikov, A. B., Schertl, D., Tuthill, P. G., Weigelt, G., & Yungelson, L. R. 2002, *A&A*, 393, 867
- Mulas, G. 1998, *A&A*, 338, 243
- Mulas, G., Malloci, G., & Benvenuti, P. 2003, *A&A*, 410, 639
- Mulas, G., Malloci, G., Joblin, C., & Toubanc, D. 2006a, *A&A*, 456, 161
- Mulas, G., Malloci, G., Joblin, C., & Toubanc, D. 2006b, *A&A*, 446, 537
- Omont, A. 1986, *A&A*, 164, 159
- Oomens, J., Tielens, A. G. G. M., Sartakov, B. G., von Helden, G., & Meijer, G. 2003, *ApJ*, 591, 968
- Pech, C., Joblin, C., & Boissel, P. 2002, *A&A*, 388, 639
- Pino, T., Boudin, N., & Bréchnignac, P. 1999, *J. Chem. Phys.*, 111, 7337
- Pirali, O. 2004, Ph.D. Thesis, Université Paris XI Orsay
- Pirali, O., Nguyen-Thi, V.-O., Parneix, P., Vervloet, M., & Bréchnignac, P. 2006, *Phys. Chem. Chem. Phys.*, 8, 3707
- Romanini, D., Biennier, L., Salama, F., et al. 1999, *Chem. Phys. Lett.*, 303, 165
- Rouan, D., Léger, A., Omont, A., & Giard, M. 1992, *A&A*, 253, 498
- Ruiterkamp, R., Halasinski, T., Salama, F., et al. 2002, *A&A*, 390, 1153
- Ruiterkamp, R., Cox, N. L. J., Spaans, M., et al. 2005, *A&A*, 432, 515
- Salama, F. 1999, in *Solid Interstellar Matter: The ISO Revolution*, ed. L. d'Hendecourt, C. Joblin, & A. Jones (EDP Sciences and Springer-Verlag), 65
- Salama, F., Bakes, E. L. O., Allamandola, L. J., & Tielens, A. G. G. M. 1996, *ApJ*, 458, 621
- Salama, F., Galazutdinov, G. A., Krelowski, J., Allamandola, L. J., & Musaev, F. A. 1999, *ApJ*, 526, 265
- Schutte, W. A., Tielens, A. G. G. M., & Allamandola, L. J. 1993, *ApJ*, 415, 397
- Sollerman, J., Cox, N., Mattila, S., et al. 2005, *A&A*, 429, 559
- Stein, S. E., & Rabinovitch, B. S. 1973, *J. Chem. Phys.*, 58, 2438
- Straatsma, T. P., Apra, E., Windus, T. L., et al. 2003, *NWChem*, A Computational Chemistry Package for Parallel Computers, Version 4.5
- Sukhorukov, O., Staicu, A., Diegel, E., et al. 2004, *Chem. Phys. Lett.*, 386, 259
- Tan, X., & Salama, F. 2005a, *J. Chem. Phys.*, 123, 014312
- Tan, X., & Salama, F. 2005b, *J. Chem. Phys.*, 122, 084318
- van der Zwet, G. P., & Allamandola, L. 1985, *A&A*, 146, 76
- Vijh, U. P., Witt, A. N., & Gordon, K. D. 2004, *ApJ*, 606, L65
- Vijh, U. P., Witt, A. N., & Gordon, K. D. 2005, *ApJ*, 619, 368
- Weingartner, J. C., & Draine, B. T. 2001, *ApJS*, 134, 263
- Zhang, K., Guo, B., Colarusso, P., & Bernath, P. F. 1996, *Science*, 274, 582

Online Material

Table A.1. Comparison between the integrated photon absorption rates \mathcal{R} (in s^{-1}) and the average absorbed energy \mathcal{E} (in eV) computed using theoretical (σ_{th} , Mallocci et al. 2004) and laboratory (σ_{lab} , Joblin 1992; Joblin et al. 1992) photo-absorption cross-sections for anthracene, pyrene, coronene, and ovalene in the three RFs considered.

	ISRF		Radiation field		IRAS 21282+5050		
	\mathcal{R} (s^{-1})	\mathcal{E} (eV)	Red Rectangle	\mathcal{R} (s^{-1})	\mathcal{E} (eV)	\mathcal{R} (s^{-1})	\mathcal{E} (eV)
Anthracene ($\text{C}_{14}\text{H}_{10}$)							
σ_{lab}	6.0×10^{-8}	7.6	1.1×10^{-6}	5.1	5.9×10^{-3}	8.9	
σ_{th}	6.4×10^{-8}	6.8	2.5×10^{-6}	4.0	5.2×10^{-3}	8.6	
Pyrene ($\text{C}_{16}\text{H}_{10}$)							
σ_{lab}	5.6×10^{-8}	7.4	1.1×10^{-6}	5.2	5.1×10^{-3}	8.9	
σ_{th}	8.1×10^{-8}	6.4	3.7×10^{-6}	3.8	5.7×10^{-3}	8.6	
Coronene ($\text{C}_{24}\text{H}_{12}$)							
σ_{lab}	1.4×10^{-7}	6.8	3.9×10^{-6}	4.5	1.1×10^{-2}	8.6	
σ_{th}	1.3×10^{-7}	6.2	4.5×10^{-6}	4.1	8.5×10^{-3}	8.5	
Ovalene ($\text{C}_{32}\text{H}_{14}$)							
σ_{lab}	2.4×10^{-7}	5.6	1.4×10^{-5}	3.5	1.3×10^{-2}	8.2	
σ_{th}	2.8×10^{-7}	4.6	2.0×10^{-5}	3.1	1.1×10^{-2}	8.2	

Appendix A: Quantitative impact of the use of theoretical photo-absorption cross-section

Table A.1 summarises the integrated photon absorption rates \mathcal{R} and the average energy \mathcal{E} of the absorbed photons computed using theoretical and laboratory photo-absorption cross sections. The overall agreement is good for all four molecules in the case of the photodissociation region of the planetary nebula IRAS 21282+5050, whose radiation field (RF) is rather flat and thus very insensitive to the small differences between laboratory and theoretical absorption spectra (see Fig. 1). The largest differences, for opposite reasons, can be seen for the RF of the Red Rectangle, mostly for the two smallest molecules, anthracene and pyrene. In the worst case, the \mathcal{R} value calculated using σ_{th} is overestimated by about a factor of ~ 3 , while \mathcal{E} is underestimated by about $\sim 40\%$. These two errors are systematically in opposite directions, since they both stem from the relatively small differences in the absorption band's theoretical positions at low energies and the steepness of the RFs. Hence the energy absorption rate, i.e. the energy absorbed per unit time by a single molecule embedded in a given RF, obviously given by $\mathcal{R} \cdot \mathcal{E}$, is more accurate than \mathcal{R} . In any standard PAH model, the energy absorption rate $\mathcal{R}\mathcal{E}$ of a molecule equals by and large the total power it radiates in all of its vibrational bands, while \mathcal{E} governs their relative intensities.

Tables A.2 to A.5 compare the calculated IR emission spectra resulting from synthetic (σ_{th}) and laboratory (σ_{lab}) photo-absorption cross sections. The agreement is *quantitatively* very good and the *relative* intensities among IR bands is very accurate, with differences of the order of, at most, $\sim 20\%$.

Figures A.1 to A.4 show the comparison between σ_{th} and σ_{lab} and the impact of their differences on the estimated energy-dependent absorption rates in the three RFs considered for anthracene, pyrene, coronene, and ovalene.

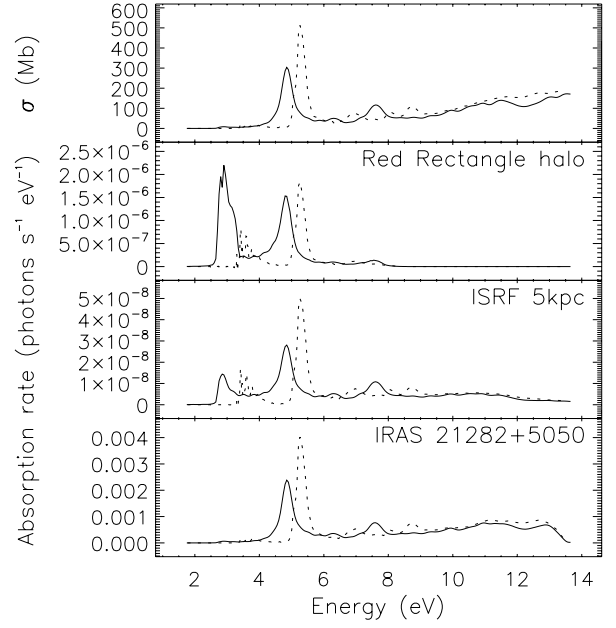


Fig. A.1. The top panel shows the comparison between the measured (dotted line; Joblin 1992; Joblin et al. 1992) and the theoretical photo-absorption cross section up to 13.6 eV (continuous line; Mallocci et al. 2004) for anthracene. The cross-sections are expressed in Megabarns ($1 \text{ Mb} = 10^{-18} \text{ cm}^2$). The three panels below show the comparison between the resulting energy-dependent photon absorption rates for a molecule embedded in the three RFs considered.

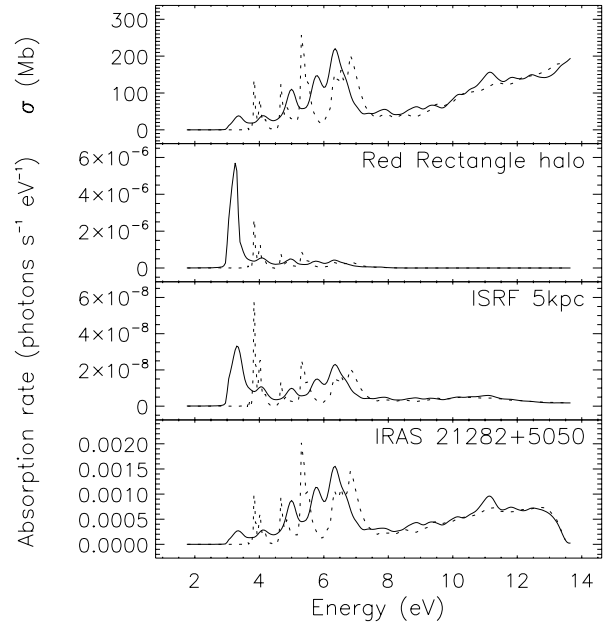


Fig. A.2. Same as Fig. A.1 for pyrene ($\text{C}_{16}\text{H}_{10}$).

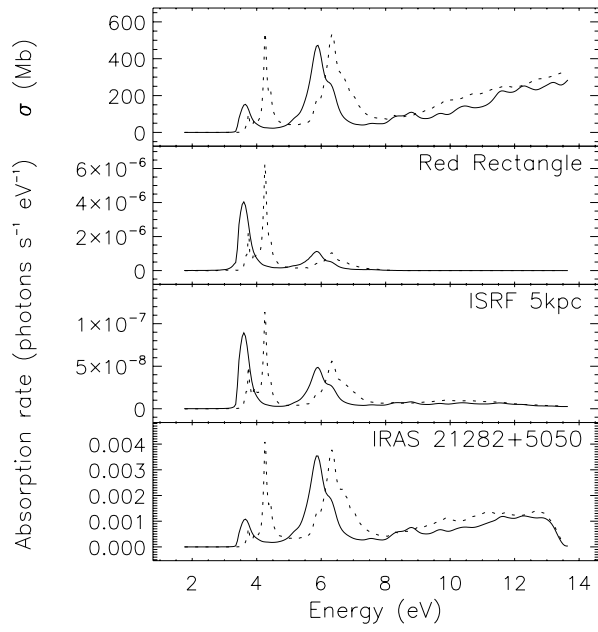


Fig. A.3. Same as Fig. A.1 for coronene ($C_{24}H_{12}$).

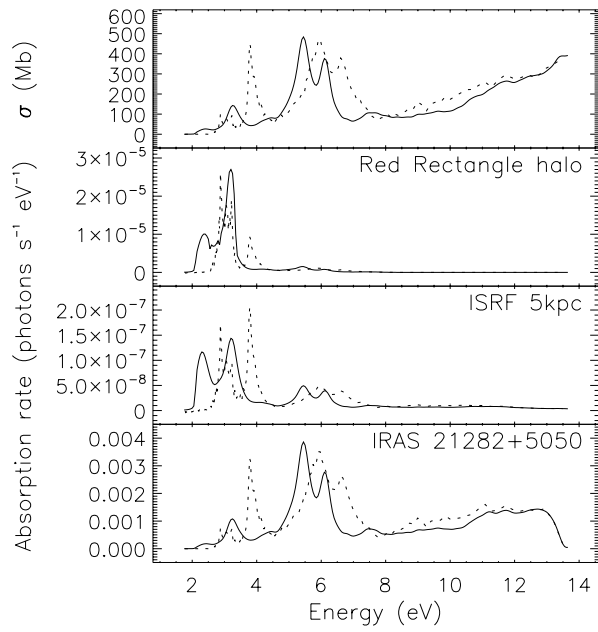


Fig. A.4. Same as Fig. A.1 for ovalene ($C_{32}H_{14}$).

Table A.2. Comparison between various model runs for neutral anthracene ($C_{14}H_{10}$), using either the experimental (σ_{lab} , Joblin 1992; Joblin et al. 1992) or the theoretical (σ_{th} , Mallocci et al. 2004) photo-absorption spectrum, in different RFs. Bands which are electric-dipole forbidden are enclosed in square brackets in the first column. In each of the other columns, we list the absolute flux emitted by one molecule in a given band and RF and, in parentheses, the flux fraction in that band. Bands whose calculated flux fraction in the ISRF is less than 0.05% are omitted.

Peak (μm)	Integrated flux					
	ISRF		Red Rectangle		IRAS 21282+5050	
	σ_{lab} (W sr^{-1}) (%)	σ_{th} (W sr^{-1}) (%)	σ_{lab} (W sr^{-1}) (%)	σ_{th} (W sr^{-1}) (%)	σ_{lab} (W sr^{-1}) (%)	σ_{th} (W sr^{-1}) (%)
3.25	1.2×10^{-27} (27.06)	1.1×10^{-27} (25.74)	1.6×10^{-26} (22.93)	2.4×10^{-26} (19.41)	1.2×10^{-22} (29.33)	9.9×10^{-23} (28.65)
3.26	7.5×10^{-28} (17.55)	7.0×10^{-28} (16.69)	1.1×10^{-26} (15.09)	1.6×10^{-26} (12.80)	7.6×10^{-23} (18.96)	6.5×10^{-23} (18.89)
3.28	2.4×10^{-30} (0.06)	2.3×10^{-30} (0.05)	3.4×10^{-29} (0.05)	5.1×10^{-29} (0.04)	2.2×10^{-25} (0.05)	2.1×10^{-25} (0.06)
3.28	2.0×10^{-28} (4.56)	1.8×10^{-28} (4.41)	2.9×10^{-27} (3.97)	4.3×10^{-27} (3.41)	2.0×10^{-23} (4.89)	1.7×10^{-23} (4.95)
3.29	1.1×10^{-28} (2.53)	1.0×10^{-28} (2.43)	1.6×10^{-27} (2.17)	2.3×10^{-27} (1.84)	1.1×10^{-23} (2.78)	9.2×10^{-24} (2.68)
6.16	1.4×10^{-28} (3.22)	1.3×10^{-28} (3.23)	2.4×10^{-27} (3.37)	4.2×10^{-27} (3.39)	1.3×10^{-23} (3.13)	1.1×10^{-23} (3.18)
6.51	3.9×10^{-29} (0.92)	3.9×10^{-29} (0.93)	6.9×10^{-28} (0.96)	1.3×10^{-27} (1.02)	3.7×10^{-24} (0.91)	3.1×10^{-24} (0.89)
6.86	7.8×10^{-29} (1.82)	7.6×10^{-29} (1.81)	1.4×10^{-27} (1.88)	2.5×10^{-27} (2.03)	7.0×10^{-24} (1.74)	6.1×10^{-24} (1.75)
6.86	3.6×10^{-29} (0.83)	3.6×10^{-29} (0.85)	6.6×10^{-28} (0.92)	1.2×10^{-27} (0.96)	3.2×10^{-24} (0.79)	2.9×10^{-24} (0.83)
7.22	2.7×10^{-30} (0.06)	2.7×10^{-30} (0.06)	5.8×10^{-29} (0.08)	9.1×10^{-29} (0.07)	2.8×10^{-25} (0.07)	2.0×10^{-25} (0.06)
7.43	4.7×10^{-29} (1.10)	4.7×10^{-29} (1.13)	9.0×10^{-28} (1.25)	1.7×10^{-27} (1.33)	4.4×10^{-24} (1.10)	3.8×10^{-24} (1.09)
7.60	7.8×10^{-29} (1.83)	7.8×10^{-29} (1.86)	1.5×10^{-27} (2.04)	2.7×10^{-27} (2.13)	6.9×10^{-24} (1.71)	6.1×10^{-24} (1.78)
7.85	9.8×10^{-29} (2.29)	9.9×10^{-29} (2.37)	1.8×10^{-27} (2.53)	3.5×10^{-27} (2.76)	8.8×10^{-24} (2.20)	7.7×10^{-24} (2.24)
8.55	1.3×10^{-29} (0.31)	1.4×10^{-29} (0.33)	2.5×10^{-28} (0.35)	4.9×10^{-28} (0.39)	1.2×10^{-24} (0.30)	1.0×10^{-24} (0.30)
8.62	3.4×10^{-29} (0.80)	3.4×10^{-29} (0.82)	6.5×10^{-28} (0.91)	1.2×10^{-27} (1.00)	3.1×10^{-24} (0.76)	2.7×10^{-24} (0.79)
8.67	9.0×10^{-29} (2.11)	9.2×10^{-29} (2.19)	1.7×10^{-27} (2.39)	3.2×10^{-27} (2.58)	8.1×10^{-24} (2.01)	6.9×10^{-24} (2.01)
9.95	4.2×10^{-29} (0.98)	4.2×10^{-29} (1.01)	8.1×10^{-28} (1.13)	1.6×10^{-27} (1.24)	3.8×10^{-24} (0.94)	3.2×10^{-24} (0.94)
10.41	7.4×10^{-29} (1.73)	7.5×10^{-29} (1.80)	1.5×10^{-27} (2.02)	2.8×10^{-27} (2.22)	6.7×10^{-24} (1.66)	5.7×10^{-24} (1.66)
11.00	1.6×10^{-29} (0.36)	1.7×10^{-29} (0.41)	3.1×10^{-28} (0.43)	6.2×10^{-28} (0.50)	1.4×10^{-24} (0.35)	1.2×10^{-24} (0.34)
11.32	5.4×10^{-28} (12.60)	5.5×10^{-28} (13.25)	1.1×10^{-26} (14.72)	2.1×10^{-26} (16.66)	4.8×10^{-23} (11.92)	4.2×10^{-23} (12.14)
13.71	5.3×10^{-28} (12.29)	5.5×10^{-28} (13.12)	1.1×10^{-26} (14.64)	2.1×10^{-26} (16.85)	4.6×10^{-23} (11.49)	4.1×10^{-23} (11.77)
15.33	9.2×10^{-30} (0.21)	9.6×10^{-30} (0.23)	2.1×10^{-28} (0.29)	3.9×10^{-28} (0.31)	7.9×10^{-25} (0.20)	7.0×10^{-25} (0.20)
[15.71]	1.7×10^{-30} (0.04)	2.2×10^{-30} (0.05)	4.1×10^{-29} (0.06)	9.9×10^{-29} (0.08)	–	–
16.34	4.2×10^{-29} (0.99)	4.4×10^{-29} (1.04)	8.5×10^{-28} (1.18)	1.7×10^{-27} (1.36)	3.6×10^{-24} (0.90)	3.2×10^{-24} (0.93)
[17.11]	2.3×10^{-30} (0.05)	2.6×10^{-30} (0.06)	5.0×10^{-29} (0.07)	1.1×10^{-28} (0.09)	–	–
[18.71]	2.8×10^{-30} (0.06)	3.3×10^{-30} (0.08)	6.4×10^{-29} (0.09)	1.4×10^{-28} (0.11)	–	–
[20.04]	3.4×10^{-30} (0.08)	3.6×10^{-30} (0.09)	7.3×10^{-29} (0.10)	1.6×10^{-28} (0.13)	–	–
[21.02]	3.4×10^{-30} (0.08)	3.9×10^{-30} (0.09)	8.1×10^{-29} (0.11)	1.8×10^{-28} (0.14)	–	–
21.26	7.3×10^{-29} (1.71)	7.7×10^{-29} (1.85)	1.5×10^{-27} (2.09)	3.1×10^{-27} (2.49)	6.3×10^{-24} (1.56)	5.6×10^{-24} (1.61)
[25.45]	5.0×10^{-30} (0.12)	5.5×10^{-30} (0.13)	1.0×10^{-28} (0.14)	2.2×10^{-28} (0.18)	–	–
[25.62]	4.7×10^{-30} (0.11)	5.4×10^{-30} (0.13)	1.1×10^{-28} (0.15)	2.3×10^{-28} (0.18)	–	–
26.35	5.3×10^{-30} (0.12)	5.9×10^{-30} (0.14)	1.1×10^{-28} (0.16)	2.6×10^{-28} (0.21)	6×10^{-26} (0.02)	6.5×10^{-26} (0.02)
[37.41]	7.4×10^{-30} (0.17)	8.2×10^{-30} (0.20)	1.5×10^{-28} (0.20)	3.2×10^{-28} (0.26)	–	–
[43.01]	8.5×10^{-30} (0.20)	8.8×10^{-30} (0.21)	1.7×10^{-28} (0.23)	3.4×10^{-28} (0.27)	–	–
43.68	1.1×10^{-29} (0.26)	1.2×10^{-29} (0.29)	2.4×10^{-28} (0.33)	5.3×10^{-28} (0.43)	6.7×10^{-25} (0.17)	6.1×10^{-25} (0.18)
[82.09]	1.1×10^{-29} (0.25)	1.3×10^{-29} (0.30)	1.8×10^{-28} (0.25)	3.0×10^{-28} (0.24)	–	–
110.23	1.3×10^{-29} (0.30)	1.4×10^{-29} (0.33)	2.8×10^{-28} (0.39)	6.4×10^{-28} (0.51)	1.8×10^{-25} (0.04)	1.8×10^{-25} (0.05)

Table A.3. Like Table A.2 for neutral pyrene (C₁₆H₁₀).

Peak (μm)	Integrated flux					
	ISRF		Red Rectangle		IRAS 21282+5050	
	σ_{lab} (W sr ⁻¹) (%)	σ_{th} (W sr ⁻¹) (%)	σ_{lab} (W sr ⁻¹) (%)	σ_{th} (W sr ⁻¹) (%)	σ_{lab} (W sr ⁻¹) (%)	σ_{th} (W sr ⁻¹) (%)
3.25	8.9×10^{-28} (21.97)	1.1×10^{-27} (20.58)	1.4×10^{-26} (19.15)	2.7×10^{-26} (15.10)	8.2×10^{-23} (24.28)	9.0×10^{-23} (23.97)
3.26	8.8×10^{-28} (21.56)	1.0×10^{-27} (19.86)	1.3×10^{-26} (18.61)	2.6×10^{-26} (15.05)	7.9×10^{-23} (23.25)	8.7×10^{-23} (23.16)
3.27	2.4×10^{-28} (5.91)	2.8×10^{-28} (5.45)	3.6×10^{-27} (5.05)	6.8×10^{-27} (3.87)	2.2×10^{-23} (6.42)	2.4×10^{-23} (6.43)
3.29	3.3×10^{-29} (0.81)	4.0×10^{-29} (0.77)	4.9×10^{-28} (0.68)	1.0×10^{-27} (0.59)	3.2×10^{-24} (0.94)	3.5×10^{-24} (0.92)
6.26	5.9×10^{-29} (1.45)	7.7×10^{-29} (1.49)	1.1×10^{-27} (1.60)	2.8×10^{-27} (1.57)	4.8×10^{-24} (1.41)	5.5×10^{-24} (1.46)
6.31	1.4×10^{-28} (3.47)	1.8×10^{-28} (3.40)	2.6×10^{-27} (3.58)	6.6×10^{-27} (3.78)	1.1×10^{-23} (3.32)	1.2×10^{-23} (3.29)
6.78	4.2×10^{-29} (1.03)	5.4×10^{-29} (1.05)	7.9×10^{-28} (1.10)	2.1×10^{-27} (1.18)	3.4×10^{-24} (0.99)	3.8×10^{-24} (1.02)
6.92	5.8×10^{-30} (0.14)	6.5×10^{-30} (0.13)	1.1×10^{-28} (0.15)	2.7×10^{-28} (0.15)	4.2×10^{-25} (0.12)	4.7×10^{-25} (0.12)
7.01	1.2×10^{-29} (0.30)	1.7×10^{-29} (0.34)	2.5×10^{-28} (0.34)	5.9×10^{-28} (0.34)	1.0×10^{-24} (0.30)	1.1×10^{-24} (0.30)
7.01	1.2×10^{-28} (3.06)	1.6×10^{-28} (3.14)	2.3×10^{-27} (3.26)	6.3×10^{-27} (3.58)	1.0×10^{-23} (2.97)	1.1×10^{-23} (2.93)
7.61	6.6×10^{-29} (1.62)	8.5×10^{-29} (1.65)	1.3×10^{-27} (1.77)	3.4×10^{-27} (1.96)	5.3×10^{-24} (1.55)	5.8×10^{-24} (1.55)
7.98	3.7×10^{-29} (0.90)	4.8×10^{-29} (0.93)	7.0×10^{-28} (0.98)	2.0×10^{-27} (1.12)	2.8×10^{-24} (0.84)	3.2×10^{-24} (0.85)
8.42	9.9×10^{-29} (2.44)	1.3×10^{-28} (2.59)	2.0×10^{-27} (2.74)	5.4×10^{-27} (3.08)	7.9×10^{-24} (2.32)	8.8×10^{-24} (2.34)
8.62	1.6×10^{-29} (0.39)	2.1×10^{-29} (0.41)	3.0×10^{-28} (0.41)	7.9×10^{-28} (0.45)	1.2×10^{-24} (0.35)	1.3×10^{-24} (0.35)
9.16	4.5×10^{-29} (1.10)	5.9×10^{-29} (1.15)	8.8×10^{-28} (1.23)	2.4×10^{-27} (1.36)	3.6×10^{-24} (1.05)	3.8×10^{-24} (1.00)
10.04	4.7×10^{-30} (0.12)	6.7×10^{-30} (0.13)	1.1×10^{-28} (0.15)	2.8×10^{-28} (0.16)	4.0×10^{-25} (0.12)	4.6×10^{-25} (0.12)
10.25	2.2×10^{-29} (0.55)	3.2×10^{-29} (0.62)	4.9×10^{-28} (0.68)	1.3×10^{-27} (0.72)	1.8×10^{-24} (0.54)	2.0×10^{-24} (0.52)
11.79	9.2×10^{-28} (22.56)	1.3×10^{-27} (24.52)	1.9×10^{-26} (25.96)	5.4×10^{-26} (30.61)	7.1×10^{-23} (20.98)	8.0×10^{-23} (21.29)
12.20	2.4×10^{-29} (0.59)	3.2×10^{-29} (0.63)	4.9×10^{-28} (0.69)	1.4×10^{-27} (0.81)	1.8×10^{-24} (0.54)	2.1×10^{-24} (0.55)
13.40	6.9×10^{-29} (1.69)	9.4×10^{-29} (1.83)	1.4×10^{-27} (1.93)	4.1×10^{-27} (2.34)	5.3×10^{-24} (1.56)	5.9×10^{-24} (1.55)
14.06	2.1×10^{-28} (5.14)	2.9×10^{-28} (5.59)	4.3×10^{-27} (6.03)	1.3×10^{-26} (7.19)	1.6×10^{-23} (4.74)	1.8×10^{-23} (4.82)
14.43	1.9×10^{-30} (0.05)	2.9×10^{-30} (0.06)	4.2×10^{-29} (0.06)	1.5×10^{-28} (0.08)	1.1×10^{-25} (0.03)	1.3×10^{-25} (0.03)
[17.26]	2.0×10^{-30} (0.05)	3.2×10^{-30} (0.06)	4.5×10^{-29} (0.06)	1.6×10^{-28} (0.09)	–	–
[17.34]	2.0×10^{-30} (0.05)	3.3×10^{-30} (0.06)	4.7×10^{-29} (0.07)	1.6×10^{-28} (0.09)	–	–
18.20	1.4×10^{-29} (0.35)	2.0×10^{-29} (0.40)	3.1×10^{-28} (0.43)	9.4×10^{-28} (0.53)	1.1×10^{-24} (0.32)	1.2×10^{-24} (0.32)
[18.98]	2.3×10^{-30} (0.06)	3.5×10^{-30} (0.07)	5.6×10^{-29} (0.08)	1.8×10^{-28} (0.10)	–	–
[19.82]	2.8×10^{-30} (0.07)	4.3×10^{-30} (0.08)	6.2×10^{-29} (0.09)	1.9×10^{-28} (0.11)	–	–
[19.93]	2.8×10^{-30} (0.07)	4.0×10^{-30} (0.08)	5.8×10^{-29} (0.08)	1.9×10^{-28} (0.11)	–	–
20.00	1.3×10^{-29} (0.33)	1.9×10^{-29} (0.38)	2.9×10^{-28} (0.40)	9.0×10^{-28} (0.51)	9.9×10^{-25} (0.29)	1.1×10^{-24} (0.30)
20.38	9.2×10^{-30} (0.23)	1.3×10^{-29} (0.26)	2.0×10^{-28} (0.27)	6.3×10^{-28} (0.36)	6.7×10^{-25} (0.20)	7.8×10^{-25} (0.21)
[21.96]	3.4×10^{-30} (0.08)	4.7×10^{-30} (0.09)	7.5×10^{-29} (0.10)	2.3×10^{-28} (0.13)	–	–
[24.64]	4.1×10^{-30} (0.10)	6.2×10^{-30} (0.12)	8.7×10^{-29} (0.12)	2.7×10^{-28} (0.16)	–	–
[25.27]	4.4×10^{-30} (0.11)	6.2×10^{-30} (0.12)	8.8×10^{-29} (0.12)	2.9×10^{-28} (0.17)	–	–
28.32	8.6×10^{-30} (0.21)	1.2×10^{-29} (0.24)	1.8×10^{-28} (0.26)	6.0×10^{-28} (0.34)	5.5×10^{-25} (0.16)	6.1×10^{-25} (0.16)
[38.63]	6.6×10^{-30} (0.16)	1.0×10^{-29} (0.19)	1.4×10^{-28} (0.20)	4.1×10^{-28} (0.23)	–	–
[40.66]	7.0×10^{-30} (0.17)	1.0×10^{-29} (0.20)	1.5×10^{-28} (0.21)	4.2×10^{-28} (0.24)	–	–
47.80	1.6×10^{-29} (0.39)	2.4×10^{-29} (0.46)	3.6×10^{-28} (0.50)	1.2×10^{-27} (0.66)	1.1×10^{-24} (0.33)	1.3×10^{-24} (0.33)
[66.26]	9.1×10^{-30} (0.22)	1.4×10^{-29} (0.27)	1.6×10^{-28} (0.23)	3.9×10^{-28} (0.22)	–	–
101.60	1.1×10^{-29} (0.27)	1.7×10^{-29} (0.32)	2.5×10^{-28} (0.35)	8.6×10^{-28} (0.49)	8.1×10^{-26} (0.02)	9.0×10^{-26} (0.02)

Table A.4. Like Table A.2 for neutral coronene (C₂₄H₁₂).

Peak (μm)	Integrated flux					
	ISRF		Red Rectangle		IRAS 21282+5050	
	σ_{lab} (W sr ⁻¹) (%)	σ_{th} (W sr ⁻¹) (%)	σ_{lab} (W sr ⁻¹) (%)	σ_{th} (W sr ⁻¹) (%)	σ_{lab} (W sr ⁻¹) (%)	σ_{th} (W sr ⁻¹) (%)
3.26	3.4×10^{-27} (36.85)	2.8×10^{-27} (34.47)	6.1×10^{-26} (27.41)	5.8×10^{-26} (24.75)	3.1×10^{-22} (43.24)	2.3×10^{-22} (42.58)
3.29	2.4×10^{-28} (2.56)	1.9×10^{-28} (2.33)	4.1×10^{-27} (1.86)	4.0×10^{-27} (1.72)	2.1×10^{-23} (2.99)	1.6×10^{-23} (2.88)
6.24	4.9×10^{-28} (5.24)	4.2×10^{-28} (5.27)	1.2×10^{-26} (5.45)	1.3×10^{-26} (5.47)	3.7×10^{-23} (5.16)	2.9×10^{-23} (5.21)
6.69	8.4×10^{-30} (0.09)	7.5×10^{-30} (0.09)	2.0×10^{-28} (0.09)	2.4×10^{-28} (0.10)	5.9×10^{-25} (0.08)	5.1×10^{-25} (0.09)
7.21	1.0×10^{-28} (1.07)	8.9×10^{-29} (1.11)	2.6×10^{-27} (1.17)	2.8×10^{-27} (1.22)	7.4×10^{-24} (1.04)	5.8×10^{-24} (1.06)
7.63	6.3×10^{-28} (6.76)	5.5×10^{-28} (6.88)	1.7×10^{-26} (7.47)	1.7×10^{-26} (7.49)	4.5×10^{-23} (6.31)	3.5×10^{-23} (6.42)
8.25	2.8×10^{-28} (2.99)	2.5×10^{-28} (3.08)	7.3×10^{-27} (3.30)	8.0×10^{-27} (3.42)	2.0×10^{-23} (2.80)	1.6×10^{-23} (2.82)
8.78	2.9×10^{-28} (3.16)	2.6×10^{-28} (3.26)	8.1×10^{-27} (3.64)	8.8×10^{-27} (3.79)	2.1×10^{-23} (2.98)	1.6×10^{-23} (2.96)
11.57	3.2×10^{-27} (33.86)	2.8×10^{-27} (35.56)	9.0×10^{-26} (40.58)	9.9×10^{-26} (42.48)	2.2×10^{-22} (30.21)	1.7×10^{-22} (30.70)
12.43	1.0×10^{-29} (0.11)	9.3×10^{-30} (0.12)	3.0×10^{-28} (0.13)	3.3×10^{-28} (0.14)	6.8×10^{-25} (0.09)	5.2×10^{-25} (0.09)
12.90	1.5×10^{-28} (1.59)	1.3×10^{-28} (1.69)	4.4×10^{-27} (1.99)	4.7×10^{-27} (2.03)	1.0×10^{-23} (1.41)	7.8×10^{-24} (1.42)
18.21	3.7×10^{-28} (3.99)	3.4×10^{-28} (4.24)	1.1×10^{-26} (4.99)	1.2×10^{-26} (5.29)	2.4×10^{-23} (3.35)	1.9×10^{-23} (3.41)
[22.28]	4.9×10^{-30} (0.05)	5.3×10^{-30} (0.07)	1.6×10^{-28} (0.07)	1.8×10^{-28} (0.08)	–	–
26.20	2.7×10^{-29} (0.29)	2.5×10^{-29} (0.31)	8.5×10^{-28} (0.38)	9.7×10^{-28} (0.42)	1.5×10^{-24} (0.21)	1.2×10^{-24} (0.22)
[27.34]	8.8×10^{-30} (0.09)	8.3×10^{-30} (0.10)	2.6×10^{-28} (0.12)	3.1×10^{-28} (0.13)	–	–
[33.59]	1.3×10^{-29} (0.14)	1.2×10^{-29} (0.15)	3.8×10^{-28} (0.17)	4.1×10^{-28} (0.18)	–	–
[34.34]	1.3×10^{-29} (0.14)	1.3×10^{-29} (0.17)	3.8×10^{-28} (0.17)	4.4×10^{-28} (0.19)	–	–
[44.57]	9.6×10^{-30} (0.10)	8.8×10^{-30} (0.11)	2.4×10^{-28} (0.11)	2.9×10^{-28} (0.12)	–	–
[61.10]	1.2×10^{-29} (0.13)	1.2×10^{-29} (0.15)	2.8×10^{-28} (0.13)	3.1×10^{-28} (0.13)	–	–
80.60	2.3×10^{-29} (0.24)	2.2×10^{-29} (0.27)	7.4×10^{-28} (0.33)	8.4×10^{-28} (0.36)	8.4×10^{-25} (0.12)	7.2×10^{-25} (0.13)
[113.37]	3.0×10^{-29} (0.33)	2.8×10^{-29} (0.36)	3.9×10^{-28} (0.18)	4.2×10^{-28} (0.18)	–	–

Table A.5. Like Table A.2 for neutral ovalene (C₃₂H₁₄).

Peak (μm)	Integrated flux					
	ISRF		Red Rectangle		IRAS 21282+5050	
	σ_{lab} (W sr ⁻¹) (%)	σ_{th} (W sr ⁻¹) (%)	σ_{lab} (W sr ⁻¹) (%)	σ_{th} (W sr ⁻¹) (%)	σ_{lab} (W sr ⁻¹) (%)	σ_{th} (W sr ⁻¹) (%)
3.26	1.4×10^{-27} (10.25)	1.2×10^{-27} (8.79)	3.6×10^{-26} (5.92)	3.7×10^{-26} (4.84)	1.3×10^{-22} (15.06)	1.0×10^{-22} (14.81)
3.26	1.1×10^{-27} (8.10)	9.1×10^{-28} (6.88)	2.8×10^{-26} (4.59)	2.8×10^{-26} (3.62)	1.0×10^{-22} (11.62)	7.8×10^{-23} (11.43)
3.27	9.5×10^{-29} (0.68)	8.1×10^{-29} (0.61)	2.4×10^{-27} (0.39)	2.7×10^{-27} (0.35)	8.9×10^{-24} (1.03)	6.8×10^{-24} (0.99)
3.29	6.1×10^{-29} (0.44)	4.8×10^{-29} (0.36)	1.6×10^{-27} (0.26)	1.5×10^{-27} (0.20)	5.4×10^{-24} (0.62)	4.5×10^{-24} (0.65)
3.29	1.2×10^{-28} (0.87)	9.9×10^{-29} (0.75)	3.0×10^{-27} (0.50)	3.1×10^{-27} (0.40)	1.1×10^{-23} (1.28)	8.2×10^{-24} (1.20)
3.29	5.3×10^{-29} (0.38)	4.8×10^{-29} (0.36)	1.3×10^{-27} (0.21)	1.5×10^{-27} (0.20)	5.2×10^{-24} (0.60)	3.8×10^{-24} (0.56)
6.19	5.9×10^{-28} (4.25)	5.3×10^{-28} (4.01)	2.4×10^{-26} (4.01)	3.0×10^{-26} (3.84)	3.9×10^{-23} (4.53)	3.0×10^{-23} (4.44)
6.26	3.4×10^{-28} (2.43)	3.1×10^{-28} (2.34)	1.4×10^{-26} (2.36)	1.7×10^{-26} (2.15)	2.3×10^{-23} (2.63)	1.7×10^{-23} (2.56)
6.35	1.5×10^{-29} (0.11)	1.4×10^{-29} (0.10)	7.0×10^{-28} (0.11)	6.4×10^{-28} (0.08)	9.1×10^{-25} (0.11)	7.8×10^{-25} (0.11)
6.49	1.2×10^{-29} (0.09)	1.3×10^{-29} (0.10)	5.8×10^{-28} (0.09)	6.6×10^{-28} (0.09)	8.0×10^{-25} (0.09)	6.2×10^{-25} (0.09)
6.57	2.9×10^{-28} (2.08)	2.6×10^{-28} (1.96)	1.2×10^{-26} (1.97)	1.5×10^{-26} (1.98)	1.8×10^{-23} (2.10)	1.4×10^{-23} (2.09)
6.74	5.2×10^{-29} (0.38)	4.6×10^{-29} (0.35)	2.1×10^{-27} (0.35)	2.7×10^{-27} (0.35)	3.3×10^{-24} (0.38)	2.5×10^{-24} (0.36)
6.87	1.6×10^{-29} (0.12)	1.5×10^{-29} (0.11)	6.7×10^{-28} (0.11)	8.9×10^{-28} (0.12)	8.7×10^{-25} (0.10)	7.7×10^{-25} (0.11)
6.96	1.3×10^{-29} (0.09)	1.1×10^{-29} (0.09)	5.4×10^{-28} (0.09)	7.2×10^{-28} (0.09)	8.1×10^{-25} (0.09)	6.3×10^{-25} (0.09)
7.15	8.6×10^{-29} (0.62)	7.4×10^{-29} (0.56)	3.9×10^{-27} (0.64)	4.6×10^{-27} (0.59)	5.4×10^{-24} (0.62)	4.2×10^{-24} (0.61)
7.18	5.8×10^{-29} (0.42)	5.2×10^{-29} (0.39)	2.6×10^{-27} (0.43)	3.3×10^{-27} (0.43)	3.5×10^{-24} (0.40)	2.9×10^{-24} (0.42)
7.25	2.4×10^{-29} (0.17)	2.2×10^{-29} (0.16)	1.1×10^{-27} (0.18)	1.1×10^{-27} (0.15)	1.4×10^{-24} (0.16)	1.1×10^{-24} (0.16)
7.29	2.3×10^{-28} (1.65)	2.2×10^{-28} (1.65)	1.0×10^{-26} (1.67)	1.3×10^{-26} (1.65)	1.4×10^{-23} (1.67)	1.1×10^{-23} (1.64)
7.59	1.0×10^{-28} (0.72)	9.4×10^{-29} (0.71)	4.3×10^{-27} (0.70)	5.2×10^{-27} (0.67)	6.0×10^{-24} (0.70)	4.7×10^{-24} (0.68)
7.67	8.5×10^{-28} (6.15)	8.0×10^{-28} (6.06)	3.8×10^{-26} (6.29)	4.8×10^{-26} (6.20)	5.1×10^{-23} (5.94)	4.1×10^{-23} (5.95)
7.83	3.5×10^{-28} (2.55)	3.4×10^{-28} (2.56)	1.6×10^{-26} (2.66)	2.1×10^{-26} (2.71)	2.2×10^{-23} (2.51)	1.7×10^{-23} (2.49)
8.07	1.1×10^{-28} (0.82)	1.1×10^{-28} (0.83)	5.3×10^{-27} (0.88)	6.5×10^{-27} (0.84)	6.9×10^{-24} (0.79)	5.4×10^{-24} (0.79)
8.13	4.3×10^{-29} (0.31)	4.3×10^{-29} (0.32)	2.1×10^{-27} (0.35)	2.7×10^{-27} (0.34)	2.8×10^{-24} (0.33)	2.0×10^{-24} (0.30)
8.24	2.9×10^{-29} (0.21)	2.9×10^{-29} (0.22)	1.3×10^{-27} (0.21)	1.7×10^{-27} (0.22)	1.7×10^{-24} (0.19)	1.3×10^{-24} (0.20)
8.48	7.4×10^{-29} (0.54)	7.5×10^{-29} (0.57)	3.6×10^{-27} (0.59)	4.6×10^{-27} (0.60)	4.3×10^{-24} (0.50)	3.5×10^{-24} (0.51)
8.56	8.7×10^{-28} (6.26)	8.5×10^{-28} (6.46)	4.1×10^{-26} (6.74)	5.2×10^{-26} (6.79)	5.1×10^{-23} (5.92)	4.1×10^{-23} (6.00)
8.63	5.2×10^{-30} (0.04)	5.5×10^{-30} (0.04)	2.2×10^{-28} (0.04)	2.5×10^{-28} (0.03)	2.8×10^{-25} (0.03)	2.0×10^{-25} (0.03)
10.28	4.2×10^{-30} (0.03)	4.9×10^{-30} (0.04)	1.9×10^{-28} (0.03)	2.7×10^{-28} (0.03)	2.4×10^{-25} (0.03)	1.8×10^{-25} (0.03)
10.36	4.8×10^{-29} (0.34)	4.9×10^{-29} (0.37)	2.4×10^{-27} (0.40)	3.1×10^{-27} (0.40)	2.5×10^{-24} (0.29)	2.0×10^{-24} (0.30)
10.98	1.6×10^{-28} (1.13)	1.5×10^{-28} (1.16)	7.7×10^{-27} (1.27)	1.0×10^{-26} (1.34)	8.4×10^{-24} (0.97)	6.7×10^{-24} (0.98)
11.18	3.2×10^{-27} (22.80)	3.1×10^{-27} (23.86)	1.6×10^{-25} (26.32)	2.1×10^{-25} (27.52)	1.7×10^{-22} (19.54)	1.4×10^{-22} (19.93)
11.86	1.9×10^{-27} (13.34)	1.9×10^{-27} (14.15)	9.5×10^{-26} (15.68)	1.3×10^{-25} (16.30)	9.7×10^{-23} (11.22)	7.8×10^{-23} (11.37)
12.86	1.7×10^{-28} (1.24)	1.8×10^{-28} (1.39)	9.1×10^{-27} (1.49)	1.2×10^{-26} (1.57)	8.9×10^{-24} (1.03)	7.3×10^{-24} (1.06)
12.89	1.1×10^{-28} (0.81)	1.1×10^{-28} (0.86)	5.8×10^{-27} (0.95)	7.6×10^{-27} (0.99)	5.7×10^{-24} (0.66)	4.4×10^{-24} (0.65)
13.13	5.9×10^{-29} (0.42)	6×10^{-29} (0.45)	3.1×10^{-27} (0.51)	4.1×10^{-27} (0.53)	3.0×10^{-24} (0.34)	2.4×10^{-24} (0.36)
14.20	5.3×10^{-29} (0.38)	5.2×10^{-29} (0.39)	2.8×10^{-27} (0.46)	3.8×10^{-27} (0.49)	2.6×10^{-24} (0.30)	2.1×10^{-24} (0.31)
15.03	9.2×10^{-30} (0.07)	7.9×10^{-30} (0.06)	4.8×10^{-28} (0.08)	6.1×10^{-28} (0.08)	4.2×10^{-25} (0.05)	3.4×10^{-25} (0.05)
15.26	6.1×10^{-30} (0.04)	5.3×10^{-30} (0.04)	2.8×10^{-28} (0.05)	3.8×10^{-28} (0.05)	2.2×10^{-25} (0.03)	2.0×10^{-25} (0.03)
15.90	4.5×10^{-28} (3.26)	4.8×10^{-28} (3.60)	2.5×10^{-26} (4.09)	3.3×10^{-26} (4.33)	2.2×10^{-23} (2.52)	1.7×10^{-23} (2.56)
17.45	7.5×10^{-29} (0.54)	7.8×10^{-29} (0.59)	4.0×10^{-27} (0.67)	5.5×10^{-27} (0.71)	3.4×10^{-24} (0.40)	2.7×10^{-24} (0.40)
18.42	2.1×10^{-28} (1.48)	2.2×10^{-28} (1.66)	1.1×10^{-26} (1.89)	1.6×10^{-26} (2.02)	9.5×10^{-24} (1.10)	7.8×10^{-24} (1.15)
20.44	1.1×10^{-29} (0.08)	1.1×10^{-29} (0.09)	5.9×10^{-28} (0.10)	8.4×10^{-28} (0.11)	4.8×10^{-25} (0.06)	3.9×10^{-25} (0.06)
23.57	3.8×10^{-29} (0.27)	3.9×10^{-29} (0.29)	2.2×10^{-27} (0.36)	2.9×10^{-27} (0.38)	1.6×10^{-24} (0.19)	1.3×10^{-24} (0.19)
25.61	9.2×10^{-29} (0.66)	1.0×10^{-28} (0.76)	5.3×10^{-27} (0.87)	7.3×10^{-27} (0.95)	3.7×10^{-24} (0.43)	3.1×10^{-24} (0.46)
29.35	4.0×10^{-30} (0.03)	4.6×10^{-30} (0.03)	1.3×10^{-28} (0.02)	1.5×10^{-28} (0.02)	–	–
29.42	8.0×10^{-29} (0.58)	8.9×10^{-29} (0.67)	4.7×10^{-27} (0.77)	6.6×10^{-27} (0.86)	3.4×10^{-24} (0.39)	2.7×10^{-24} (0.39)
36.70	6.7×10^{-29} (0.49)	7.6×10^{-29} (0.58)	3.9×10^{-27} (0.64)	5.5×10^{-27} (0.71)	2.6×10^{-24} (0.30)	2.2×10^{-24} (0.32)
[37.15]	6.3×10^{-30} (0.05)	7.9×10^{-30} (0.06)	1.8×10^{-28} (0.03)	2.2×10^{-28} (0.03)	–	–
[39.08]	7.4×10^{-30} (0.05)	8.3×10^{-30} (0.06)	2.0×10^{-28} (0.03)	2.4×10^{-28} (0.03)	–	–
47.39	1.0×10^{-29} (0.07)	1.2×10^{-29} (0.09)	2.1×10^{-28} (0.04)	2.4×10^{-28} (0.03)	–	–
[51.42]	1.1×10^{-29} (0.08)	1.3×10^{-29} (0.10)	2.3×10^{-28} (0.04)	2.4×10^{-28} (0.03)	–	–
[65.35]	1.4×10^{-29} (0.10)	1.8×10^{-29} (0.13)	2.0×10^{-28} (0.03)	2.2×10^{-28} (0.03)	–	–
[79.27]	1.7×10^{-29} (0.12)	1.9×10^{-29} (0.15)	1.9×10^{-28} (0.03)	1.9×10^{-28} (0.03)	–	–
93.33	3.0×10^{-29} (0.22)	3.4×10^{-29} (0.26)	1.8×10^{-27} (0.30)	2.5×10^{-27} (0.33)	5.1×10^{-25} (0.06)	4.5×10^{-25} (0.07)
160.24	2.6×10^{-29} (0.18)	3.1×10^{-29} (0.23)	1.5×10^{-27} (0.25)	2.2×10^{-27} (0.28)	–	–
[161.07]	1.9×10^{-29} (0.13)	2.1×10^{-29} (0.16)	7.1×10^{-29} (0.01)	7.6×10^{-29} (0.01)	–	–

Appendix B: Comparison between detailed and approximated PAH photophysics

Tables from B.1 to B.3 shows the comparison between model runs for neutral anthracene, phenanthrene, and pyrene, either taking into account the detailed relaxation channels available or assuming only IR de-excitation. Neglecting fluorescence and phosphorescence leads to an overestimation of the absolute emission fluxes by up to a factor ~ 2 in the worst case for the high energy bands. Low energy bands are almost unaffected. This is because fluorescence and/or phosphorescence, when they occur, essentially cause the molecule to “skip” the high excitation part of the vibrational cascade, in which high energy vibrational photons are preferentially emitted, while the low energy vibrational photons are emitted near the end of the emission cascade and this part is never skipped anyway.

All closed-shell (e.g. neutral, fully hydrogenated) PAHs, upon excitation $S_n \leftarrow S_0$, will almost always (i.e. if they don't ionise or dissociate) undergo very fast internal conversion (IC) to a low lying singlet electronic level S_m , which is usually S_1 (e.g. Leach 1995a,b), with few exceptions (e.g. fluorene, for which it is S_2). From there, three relaxation channels are available, their branching ratios being dependent on the vibrational energy available:

1. fluorescence $S_m \rightarrow S_0$ with a permitted electronic transition, the remaining energy being subsequently radiated by vibrational transitions in S_0 ; relaxation of small PAHs via this path is the proposed origin of the blue luminescence observed in the Red Rectangle (Vijh et al. 2004, 2005);
2. direct $S_m \rightsquigarrow T_1$ or indirect $S_m \rightsquigarrow T_n \rightsquigarrow T_1$ intersystem crossing, a radiationless transition followed by the emission of a phosphorescence photon in a $T_1 \rightarrow S_0$ spin-forbidden, electronic-permitted transition; the remaining energy is radiated in vibrational transitions either (almost always) from S_0 after the phosphorescence transition or (very seldom) from the first triplet state T_1 before it;
3. IC $S_m \rightsquigarrow S_0$, a radiationless transition, after which essentially all the excitation energy is radiated by vibrational transitions.

According to experimental results (Bréchnignac 2005), the rate of fluorescence transitions (1) is essentially independent of the excitation energy. The rate of radiationless transitions (2) increases slightly with excitation energy for the three molecules considered. The relaxation path (3) by IC to the ground state is opened only when some excess vibrational energy in S_m is available, such threshold depending on the specific molecule, varying e.g. from $\sim 2 \times 10^3 \text{ cm}^{-1}$ for anthracene to $\sim 4 \times 10^4 \text{ cm}^{-1}$ for pyrene (Bréchnignac 2005). Above this threshold the rate of IC to S_0 (3) increases exponentially, becoming by and large the dominant relaxation path.

Table B.1. Comparison between model runs for neutral anthracene, assuming the detailed relaxation channels available or considering only IR de-excitation. We list the absolute flux emitted by one molecule in the Red Rectangle RF and, in parentheses, the flux fraction in that band. Bands whose calculated flux fraction is $\leq 0.03\%$ are omitted. Electric-dipole forbidden bands are enclosed in square brackets.

Peak (μm)	Detailed (Wsr^{-1}) (%)	Approximated (Wsr^{-1}) (%)
3.25	1.4×10^{-26} (22.40)	1.6×10^{-26} (22.93)
3.26	9.3×10^{-27} (14.59)	1.1×10^{-26} (15.09)
3.28	3.0×10^{-29} (0.05)	3.4×10^{-29} (0.05)
3.28	2.5×10^{-27} (3.86)	2.9×10^{-27} (3.97)
3.29	1.3×10^{-27} (2.12)	1.6×10^{-27} (2.17)
6.16	2.1×10^{-27} (3.33)	2.4×10^{-27} (3.37)
6.51	6.2×10^{-28} (0.98)	6.9×10^{-28} (0.96)
6.86	1.2×10^{-27} (1.95)	1.4×10^{-27} (1.88)
6.86	5.7×10^{-28} (0.89)	6.6×10^{-28} (0.92)
7.22	4.2×10^{-29} (0.07)	5.8×10^{-29} (0.08)
7.43	7.8×10^{-28} (1.22)	9.0×10^{-28} (1.25)
7.60	1.3×10^{-27} (2.00)	1.5×10^{-27} (2.04)
7.85	1.6×10^{-27} (2.57)	1.8×10^{-27} (2.53)
8.55	2.3×10^{-28} (0.36)	2.5×10^{-28} (0.35)
8.62	5.9×10^{-28} (0.93)	6.5×10^{-28} (0.91)
8.67	1.5×10^{-27} (2.35)	1.7×10^{-27} (2.39)
9.95	7.3×10^{-28} (1.15)	8.1×10^{-28} (1.13)
10.41	1.3×10^{-27} (2.05)	1.5×10^{-27} (2.02)
11.00	2.8×10^{-28} (0.44)	3.1×10^{-28} (0.43)
11.32	9.6×10^{-27} (15.04)	1.1×10^{-26} (14.72)
13.71	9.6×10^{-27} (15.02)	1.1×10^{-26} (14.64)
15.33	1.8×10^{-28} (0.28)	2.1×10^{-28} (0.29)
[15.71]	4.1×10^{-29} (0.06)	4.1×10^{-29} (0.06)
16.34	7.7×10^{-28} (1.22)	8.5×10^{-28} (1.18)
[17.11]	5.3×10^{-29} (0.08)	5.0×10^{-29} (0.07)
[18.71]	6.5×10^{-29} (0.10)	6.4×10^{-29} (0.09)
[20.04]	7.8×10^{-29} (0.12)	7.3×10^{-29} (0.10)
[21.02]	8.1×10^{-29} (0.13)	8.1×10^{-29} (0.11)
21.26	1.4×10^{-27} (2.20)	1.5×10^{-27} (2.09)
[25.45]	1.0×10^{-28} (0.16)	1.0×10^{-28} (0.14)
[25.62]	1.1×10^{-28} (0.17)	1.1×10^{-28} (0.15)
26.35	1.2×10^{-28} (0.18)	1.1×10^{-28} (0.16)
[37.41]	1.5×10^{-28} (0.23)	1.5×10^{-28} (0.20)
[43.01]	1.7×10^{-28} (0.27)	1.7×10^{-28} (0.23)
43.68	2.3×10^{-28} (0.36)	2.4×10^{-28} (0.33)
[82.09]	1.8×10^{-28} (0.29)	1.8×10^{-28} (0.25)
110.23	2.8×10^{-28} (0.44)	2.8×10^{-28} (0.39)

Table B.2. Like Table C.5 for neutral phenanthrene (C₁₄H₁₀).

Peak (μm)	Detailed (Wsr ⁻¹) (%)	Approximated (Wsr ⁻¹) (%)
3.23	3.6×10^{-27} (6.57)	6.2×10^{-27} (7.20)
3.24	4.3×10^{-27} (7.89)	7.1×10^{-27} (8.35)
3.25	3.1×10^{-28} (0.56)	5.5×10^{-28} (0.64)
3.26	5.8×10^{-27} (10.60)	9.4×10^{-27} (10.97)
3.26	5.1×10^{-27} (9.43)	8.6×10^{-27} (10.01)
3.27	2.2×10^{-27} (4.13)	3.7×10^{-27} (4.38)
3.28	3.2×10^{-28} (0.58)	4.9×10^{-28} (0.57)
3.28	6.2×10^{-28} (1.15)	9.8×10^{-28} (1.15)
3.29	7.0×10^{-29} (0.13)	1.0×10^{-28} (0.12)
6.21	1.3×10^{-28} (0.23)	2.0×10^{-28} (0.24)
6.23	8.8×10^{-29} (0.16)	1.4×10^{-28} (0.16)
6.27	6.9×10^{-28} (1.27)	1.1×10^{-27} (1.33)
6.57	2.6×10^{-28} (0.48)	4.8×10^{-28} (0.57)
6.68	1.1×10^{-27} (2.07)	1.9×10^{-27} (2.18)
6.84	2.2×10^{-27} (4.05)	3.7×10^{-27} (4.30)
6.93	5.7×10^{-28} (1.05)	9.7×10^{-28} (1.14)
7.04	1.0×10^{-28} (0.18)	1.8×10^{-28} (0.21)
7.06	1.5×10^{-28} (0.27)	2.4×10^{-28} (0.28)
7.45	3.5×10^{-28} (0.64)	5.6×10^{-28} (0.66)
7.70	2.4×10^{-28} (0.45)	4.1×10^{-28} (0.48)
8.00	1.5×10^{-27} (2.68)	2.3×10^{-27} (2.71)
8.16	1.4×10^{-28} (0.25)	2.1×10^{-28} (0.25)
8.31	3.0×10^{-28} (0.55)	4.9×10^{-28} (0.57)
8.46	1.0×10^{-28} (0.19)	1.6×10^{-28} (0.19)
8.60	3.7×10^{-29} (0.07)	5.8×10^{-29} (0.07)
8.71	1.9×10^{-28} (0.36)	3.2×10^{-28} (0.37)
9.15	1.3×10^{-28} (0.23)	2.0×10^{-28} (0.23)
9.63	5.4×10^{-28} (0.99)	8.6×10^{-28} (1.01)
9.66	9.5×10^{-29} (0.18)	1.4×10^{-28} (0.17)
10.01	2.1×10^{-28} (0.38)	3.2×10^{-28} (0.37)
10.53	6.2×10^{-28} (1.15)	9.3×10^{-28} (1.09)
11.48	1.5×10^{-27} (2.71)	2.3×10^{-27} (2.64)
11.49	2.2×10^{-28} (0.40)	3.1×10^{-28} (0.37)
12.05	2.9×10^{-29} (0.05)	3.5×10^{-29} (0.04)
12.24	7.5×10^{-27} (13.83)	1.2×10^{-26} (13.46)
12.70	2.8×10^{-29} (0.05)	2.3×10^{-29} (0.03)
13.23	3.0×10^{-29} (0.05)	3.2×10^{-29} (0.04)
13.58	8.9×10^{-27} (16.30)	1.3×10^{-26} (15.56)
13.95	3.1×10^{-28} (0.58)	4.3×10^{-28} (0.50)
13.98	1.8×10^{-28} (0.33)	2.6×10^{-28} (0.30)
14.12	4.6×10^{-29} (0.08)	4.8×10^{-29} (0.06)
15.94	5.2×10^{-28} (0.96)	7.3×10^{-28} (0.85)
[16.86]	6.3×10^{-29} (0.12)	6.2×10^{-29} (0.07)
18.19	1.1×10^{-28} (0.21)	1.2×10^{-28} (0.14)
[18.73]	7.6×10^{-29} (0.14)	7.5×10^{-29} (0.09)
19.99	1.6×10^{-28} (0.29)	1.8×10^{-28} (0.21)
20.07	4.0×10^{-28} (0.74)	5.5×10^{-28} (0.64)
22.75	2.4×10^{-28} (0.44)	2.8×10^{-28} (0.33)
23.25	4.8×10^{-28} (0.88)	6.3×10^{-28} (0.74)
24.72	1.5×10^{-28} (0.28)	1.7×10^{-28} (0.20)
[25.36]	1.3×10^{-28} (0.23)	1.2×10^{-28} (0.14)
41.08	2.4×10^{-28} (0.45)	2.5×10^{-28} (0.29)
[41.68]	1.8×10^{-28} (0.34)	1.9×10^{-28} (0.22)
44.26	3.1×10^{-28} (0.57)	3.5×10^{-28} (0.41)
100.13	3.5×10^{-28} (0.65)	3.4×10^{-28} (0.40)
[105.47]	1.3×10^{-28} (0.25)	1.4×10^{-28} (0.16)

Table B.3. Like Table C.5 for neutral pyrene (C₁₆H₁₀).

Peak (μm)	Integrated flux	
	Detailed (Wsr ⁻¹) (%)	Approximated (Wsr ⁻¹) (%)
3.25	9.6×10^{-27} (17.55)	1.4×10^{-26} (19.15)
3.26	9.3×10^{-27} (16.94)	1.3×10^{-26} (18.61)
3.27	2.6×10^{-27} (4.70)	3.6×10^{-27} (5.05)
3.29	3.6×10^{-28} (0.66)	4.9×10^{-28} (0.68)
6.26	8.4×10^{-28} (1.53)	1.1×10^{-27} (1.60)
6.31	1.9×10^{-27} (3.53)	2.6×10^{-27} (3.58)
6.78	6.1×10^{-28} (1.12)	7.9×10^{-28} (1.10)
6.92	7.4×10^{-29} (0.14)	1.1×10^{-28} (0.15)
7.01	1.8×10^{-28} (0.32)	2.5×10^{-28} (0.34)
7.01	1.8×10^{-27} (3.30)	2.3×10^{-27} (3.26)
7.61	9.8×10^{-28} (1.78)	1.3×10^{-27} (1.77)
7.98	5.6×10^{-28} (1.02)	7.0×10^{-28} (0.98)
8.42	1.5×10^{-27} (2.75)	2.0×10^{-27} (2.74)
8.62	2.4×10^{-28} (0.43)	3.0×10^{-28} (0.41)
9.16	7.1×10^{-28} (1.29)	8.8×10^{-28} (1.23)
10.04	8.4×10^{-29} (0.15)	1.1×10^{-28} (0.15)
10.25	3.7×10^{-28} (0.67)	4.9×10^{-28} (0.68)
10.47	3.3×10^{-29} (0.06)	4.0×10^{-29} (0.06)
11.79	1.5×10^{-26} (27.79)	1.9×10^{-26} (25.96)
12.20	4.0×10^{-28} (0.74)	4.9×10^{-28} (0.69)
13.40	1.2×10^{-27} (2.14)	1.4×10^{-27} (1.93)
14.06	3.6×10^{-27} (6.55)	4.3×10^{-27} (6.03)
14.43	4.1×10^{-29} (0.07)	4.2×10^{-29} (0.06)
14.75	2.6×10^{-29} (0.05)	2.7×10^{-29} (0.04)
[17.26]	4.5×10^{-29} (0.08)	4.5×10^{-29} (0.06)
[17.34]	4.6×10^{-29} (0.08)	4.7×10^{-29} (0.07)
18.20	2.6×10^{-28} (0.48)	3.1×10^{-28} (0.43)
[18.98]	5.5×10^{-29} (0.10)	5.6×10^{-29} (0.08)
[19.82]	6.1×10^{-29} (0.11)	6.2×10^{-29} (0.09)
[19.93]	6.4×10^{-29} (0.12)	5.8×10^{-29} (0.08)
20.00	2.6×10^{-28} (0.48)	2.9×10^{-28} (0.40)
20.38	1.8×10^{-28} (0.33)	2.0×10^{-28} (0.27)
[21.96]	7.2×10^{-29} (0.13)	7.5×10^{-29} (0.10)
[24.64]	8.7×10^{-29} (0.16)	8.7×10^{-29} (0.12)
[25.27]	9.1×10^{-29} (0.17)	8.8×10^{-29} (0.12)
28.32	1.8×10^{-28} (0.32)	1.8×10^{-28} (0.26)
[38.63]	1.4×10^{-28} (0.26)	1.4×10^{-28} (0.20)
[40.66]	1.5×10^{-28} (0.27)	1.5×10^{-28} (0.21)
47.80	3.3×10^{-28} (0.61)	3.6×10^{-28} (0.50)
[66.26]	1.7×10^{-28} (0.32)	1.6×10^{-28} (0.23)
101.60	2.6×10^{-28} (0.46)	2.5×10^{-28} (0.35)

Appendix C: Detailed far-IR spectra for all molecules in the sample

In the following, we report all the calculated far-IR spectra in full detail for our sample of molecules and RFs. In each table, we listed band positions and expected integrated fluxes. Only bands redwards of $\sim 15 \mu\text{m}$ are included. Bands whose calculated flux fraction in the ISRF is $\leq 0.05\%$ of the total IR emission were omitted. The positions of electric-dipole forbidden bands are enclosed in square brackets. Bands corresponding to vibrations parallel or perpendicular to the symmetry plane of the molecule are marked by \parallel and \perp , respectively.

Table C.1. Predicted far-IR ($\lambda_{\text{peak}} \geq 15 \mu\text{m}$) emission spectrum of one molecule of neutral naphthalene (C_{10}H_8) in different exciting RFs. Under optically thin conditions total fluxes can be obtained simply multiplying these fluxes by the appropriate column density.

Peak (μm)	Integrated flux		
	ISRF (W sr^{-1}) (%)	Red Rectangle (W sr^{-1}) (%)	IRAS 21282+5050 (W sr^{-1}) (%)
15.82	1.6×10^{-29} (0.51)	2.5×10^{-28} (0.62)	1.4×10^{-24} (0.48)
[15.90]	4.3×10^{-30} (0.14)	7.3×10^{-29} (0.18)	–
[19.50]	5.4×10^{-30} (0.18)	9.7×10^{-29} (0.24)	–
[19.54]	5.4×10^{-30} (0.18)	9.4×10^{-29} (0.23)	–
⊥ 20.88	4.7×10^{-29} (1.53)	7.5×10^{-28} (1.83)	4.1×10^{-24} (1.45)
[21.16]	6.0×10^{-30} (0.20)	1.0×10^{-28} (0.25)	–
[25.75]	7.3×10^{-30} (0.24)	1.3×10^{-28} (0.31)	–
27.74	9.1×10^{-30} (0.30)	1.6×10^{-28} (0.40)	6.6×10^{-25} (0.23)
[53.95]	1.1×10^{-29} (0.36)	1.8×10^{-28} (0.43)	–
⊥ 58.56	1.2×10^{-29} (0.39)	2.0×10^{-28} (0.49)	4.9×10^{-25} (0.17)

Table C.2. Like Table C.1 for the naphthalene cation ($\text{C}_{10}\text{H}_8^+$).

Peak (μm)	Integrated flux		
	ISRF (W sr^{-1}) (%)	Red Rectangle (W sr^{-1}) (%)	IRAS 21282+5050 (W sr^{-1}) (%)
16.37	2.4×10^{-29} (0.74)	1.1×10^{-27} (0.98)	1.2×10^{-24} (0.56)
[17.83]	8.1×10^{-30} (0.25)	4.3×10^{-28} (0.38)	1.3×10^{-26} (0.01)
[19.96]	9.6×10^{-30} (0.29)	4.4×10^{-28} (0.40)	1.1×10^{-26} (0.01)
[20.72]	1.0×10^{-29} (0.31)	4.7×10^{-28} (0.42)	1.5×10^{-26} (0.01)
[22.77]	1.1×10^{-29} (0.33)	5.3×10^{-28} (0.48)	1.2×10^{-26} (0.01)
⊥ 23.64	3.5×10^{-29} (1.06)	1.5×10^{-27} (1.39)	1.6×10^{-24} (0.76)
[27.07]	1.3×10^{-29} (0.38)	6.4×10^{-28} (0.58)	–
28.31	1.5×10^{-29} (0.46)	7.4×10^{-28} (0.67)	5.4×10^{-25} (0.25)
[55.16]	1.9×10^{-29} (0.58)	8.1×10^{-28} (0.73)	–
⊥ 63.98	2.1×10^{-29} (0.63)	1.0×10^{-27} (0.95)	5.6×10^{-25} (0.26)

Table C.3. Like Table C.1 for fluorene ($\text{C}_{13}\text{H}_{10}$).

Peak (μm)	Integrated flux		
	ISRF (W sr^{-1}) (%)	Red Rectangle (W sr^{-1}) (%)	IRAS 21282+5050 (W sr^{-1}) (%)
⊥ 15.78	3.7×10^{-30} (0.10)	6.8×10^{-29} (0.11)	2.4×10^{-25} (0.07)
16.04	3.7×10^{-29} (0.97)	6.9×10^{-28} (1.17)	3.1×10^{-24} (0.89)
[17.69]	2.5×10^{-30} (0.07)	5.3×10^{-29} (0.09)	–
18.49	3.4×10^{-30} (0.09)	7.3×10^{-29} (0.12)	1.7×10^{-25} (0.05)
⊥ 20.56	6.6×10^{-30} (0.17)	1.3×10^{-28} (0.22)	4.7×10^{-25} (0.14)
20.65	5.3×10^{-30} (0.14)	1.1×10^{-28} (0.18)	3.7×10^{-25} (0.11)
[23.72]	4.4×10^{-30} (0.11)	8.4×10^{-29} (0.14)	–
23.83	6.2×10^{-30} (0.16)	1.3×10^{-28} (0.21)	3.6×10^{-25} (0.11)
⊥ 23.92	2.6×10^{-29} (0.68)	5.1×10^{-28} (0.85)	2.1×10^{-24} (0.60)
[39.45]	7.3×10^{-30} (0.19)	1.4×10^{-28} (0.23)	–
⊥ 40.26	1.7×10^{-29} (0.43)	3.3×10^{-28} (0.55)	1.2×10^{-24} (0.36)
45.48	8.2×10^{-30} (0.21)	1.7×10^{-28} (0.29)	9.4×10^{-26} (0.03)
[60.73]	9.3×10^{-30} (0.24)	1.5×10^{-28} (0.25)	–
⊥ 135.37	1.2×10^{-29} (0.31)	2.5×10^{-28} (0.43)	5.9×10^{-26} (0.02)

Table C.4. Like Table C.1 for the fluorene cation ($C_{13}H_{10}^+$).

Peak (μm)	Integrated flux		
	ISRF (W sr^{-1}) (%)	Red Rectangle (W sr^{-1}) (%)	IRAS 21282+5050 (W sr^{-1}) (%)
\perp 15.15	5.0×10^{-29} (0.90)	2.4×10^{-27} (1.06)	2.0×10^{-24} (0.68)
\parallel 16.14	7.3×10^{-30} (0.13)	3.7×10^{-28} (0.16)	1.8×10^{-25} (0.06)
\parallel 16.35	1.1×10^{-28} (1.91)	5.1×10^{-27} (2.23)	3.9×10^{-24} (1.37)
\parallel 18.92	1.4×10^{-29} (0.26)	7.2×10^{-28} (0.32)	4.3×10^{-25} (0.15)
[20.11]	8.1×10^{-30} (0.15)	3.7×10^{-28} (0.16)	–
[20.38]	7.8×10^{-30} (0.14)	4×10^{-28} (0.17)	–
[22.64]	9.6×10^{-30} (0.17)	4.5×10^{-28} (0.20)	–
\perp 22.84	3.1×10^{-29} (0.56)	1.6×10^{-27} (0.71)	9.9×10^{-25} (0.35)
\parallel 24.23	1.2×10^{-29} (0.22)	6.1×10^{-28} (0.27)	2.1×10^{-25} (0.07)
\perp 25.54	1.6×10^{-29} (0.30)	9.3×10^{-28} (0.41)	4.3×10^{-25} (0.15)
[40.59]	1.8×10^{-29} (0.33)	7.2×10^{-28} (0.32)	–
\perp 43.62	2.7×10^{-29} (0.49)	1.5×10^{-27} (0.64)	6.7×10^{-25} (0.24)
\parallel 47.31	2.2×10^{-29} (0.40)	1.2×10^{-27} (0.52)	2.5×10^{-25} (0.09)
[78.65]	2.6×10^{-29} (0.48)	5.4×10^{-28} (0.24)	–
\perp 122.23	3.1×10^{-29} (0.56)	1.7×10^{-27} (0.74)	1.3×10^{-25} (0.04)

Table C.5. Like Table C.1 for anthracene ($C_{14}H_{10}$).

Peak (μm)	Integrated flux		
	ISRF (W sr^{-1}) (%)	Red Rectangle (W sr^{-1}) (%)	IRAS 21282+5050 (W sr^{-1}) (%)
\parallel 15.33	9.6×10^{-30} (0.23)	3.9×10^{-28} (0.31)	7.0×10^{-25} (0.20)
[15.71]	2.2×10^{-30} (0.05)	9.9×10^{-29} (0.08)	–
\parallel 16.34	4.4×10^{-29} (1.04)	1.7×10^{-27} (1.36)	3.2×10^{-24} (0.93)
[17.11]	2.6×10^{-30} (0.06)	1.1×10^{-28} (0.09)	–
[18.71]	3.3×10^{-30} (0.08)	1.4×10^{-28} (0.11)	–
[20.04]	3.6×10^{-30} (0.09)	1.6×10^{-28} (0.13)	–
[21.02]	3.9×10^{-30} (0.09)	1.8×10^{-28} (0.14)	–
\perp 21.26	7.7×10^{-29} (1.85)	3.1×10^{-27} (2.49)	5.6×10^{-24} (1.61)
[25.45]	5.5×10^{-30} (0.13)	2.2×10^{-28} (0.18)	–
[25.62]	5.4×10^{-30} (0.13)	2.3×10^{-28} (0.18)	–
\perp 26.35	5.9×10^{-30} (0.14)	2.6×10^{-28} (0.21)	6.5×10^{-26} (0.02)
[37.41]	8.2×10^{-30} (0.20)	3.2×10^{-28} (0.26)	–
[43.01]	8.8×10^{-30} (0.21)	3.4×10^{-28} (0.27)	–
\parallel 43.68	1.2×10^{-29} (0.29)	5.3×10^{-28} (0.43)	6.1×10^{-25} (0.18)
[82.09]	1.3×10^{-29} (0.30)	3.0×10^{-28} (0.24)	–
\perp 110.23	1.4×10^{-29} (0.33)	6.4×10^{-28} (0.51)	1.8×10^{-25} (0.05)

Table C.6. Like Table C.1 for the anthracene cation ($C_{14}H_{10}^+$).

Peak (μm)	Integrated flux		
	ISRF (W sr^{-1}) (%)	Red Rectangle (W sr^{-1}) (%)	IRAS 21282+5050 (W sr^{-1}) (%)
15.08	9.2×10^{-30} (0.13)	4.1×10^{-28} (0.15)	2.5×10^{-25} (0.07)
[15.94]	5.3×10^{-30} (0.08)	2.5×10^{-28} (0.09)	–
16.56	6.9×10^{-30} (0.10)	3.6×10^{-28} (0.13)	1.9×10^{-25} (0.05)
[17.97]	7.0×10^{-30} (0.10)	3.5×10^{-28} (0.13)	–
[19.41]	8.3×10^{-30} (0.12)	4.2×10^{-28} (0.16)	–
[20.84]	9.8×10^{-30} (0.14)	5.0×10^{-28} (0.19)	–
[22.02]	1.1×10^{-29} (0.16)	5.4×10^{-28} (0.20)	–
⊥ 22.81	7.5×10^{-29} (1.10)	3.6×10^{-27} (1.34)	2.7×10^{-24} (0.69)
[26.02]	1.4×10^{-29} (0.21)	6.7×10^{-28} (0.25)	–
⊥ 26.51	1.5×10^{-29} (0.22)	8.0×10^{-28} (0.30)	2.0×10^{-25} (0.05)
[26.90]	1.5×10^{-29} (0.22)	7.4×10^{-28} (0.27)	–
[37.28]	2.2×10^{-29} (0.33)	9.5×10^{-28} (0.35)	–
44.40	2.9×10^{-29} (0.43)	1.5×10^{-27} (0.55)	6.5×10^{-25} (0.17)
[45.89]	2.6×10^{-29} (0.37)	1.0×10^{-27} (0.38)	–
[83.78]	3.4×10^{-29} (0.49)	9.5×10^{-28} (0.35)	–
⊥ 115.42	3.8×10^{-29} (0.56)	2.0×10^{-27} (0.74)	2.7×10^{-25} (0.07)

Table C.7. Like Table C.1 for phenanthrene ($C_{14}H_{10}$).

Peak (μm)	Integrated flux		
	ISRF (W sr^{-1}) (%)	Red Rectangle (W sr^{-1}) (%)	IRAS 21282+5050 (W sr^{-1}) (%)
15.94	2.9×10^{-29} (0.70)	7.3×10^{-28} (0.85)	2.2×10^{-24} (0.61)
[16.86]	2.2×10^{-30} (0.05)	6.2×10^{-29} (0.07)	–
18.19	4.5×10^{-30} (0.11)	1.2×10^{-28} (0.14)	2.7×10^{-25} (0.07)
[18.73]	2.8×10^{-30} (0.07)	7.5×10^{-29} (0.09)	–
19.99	6.8×10^{-30} (0.16)	1.8×10^{-28} (0.21)	4.7×10^{-25} (0.13)
⊥ 20.07	2.0×10^{-29} (0.48)	5.5×10^{-28} (0.64)	1.6×10^{-24} (0.44)
22.75	1.0×10^{-29} (0.25)	2.8×10^{-28} (0.33)	7.4×10^{-25} (0.21)
⊥ 23.25	2.4×10^{-29} (0.57)	6.3×10^{-28} (0.74)	1.8×10^{-24} (0.50)
24.72	6.1×10^{-30} (0.15)	1.7×10^{-28} (0.20)	3.0×10^{-25} (0.08)
[25.36]	4.9×10^{-30} (0.12)	1.2×10^{-28} (0.14)	–
41.08	8.7×10^{-30} (0.21)	2.5×10^{-28} (0.29)	2.4×10^{-25} (0.07)
[41.68]	7.8×10^{-30} (0.19)	1.9×10^{-28} (0.22)	–
⊥ 44.26	1.2×10^{-29} (0.30)	3.5×10^{-28} (0.41)	7.5×10^{-25} (0.21)
⊥ 100.13	1.2×10^{-29} (0.30)	3.4×10^{-28} (0.40)	1.3×10^{-25} (0.04)
[105.47]	1.1×10^{-29} (0.27)	1.4×10^{-28} (0.16)	–

Table C.8. Like Table C.1 for the phenanthrene cation ($C_{14}H_{10}^+$).

Peak (μm)	Integrated flux		
	ISRF (W sr^{-1}) (%)	Red Rectangle (W sr^{-1}) (%)	IRAS 21282+5050 (W sr^{-1}) (%)
16.49	7.1×10^{-29} (1.12)	3.6×10^{-28} (1.35)	2.4×10^{-24} (0.70)
18.23	1.1×10^{-29} (0.18)	5.9×10^{-29} (0.22)	2.4×10^{-25} (0.07)
[18.34]	7.0×10^{-30} (0.11)	3.8×10^{-29} (0.14)	–
20.26	1.3×10^{-29} (0.20)	7.8×10^{-29} (0.29)	3.3×10^{-25} (0.10)
[20.82]	9.0×10^{-30} (0.14)	4.6×10^{-29} (0.17)	–
⊥ 21.17	1.1×10^{-29} (0.17)	5.7×10^{-29} (0.21)	1.4×10^{-25} (0.04)
22.98	1.2×10^{-29} (0.19)	6.6×10^{-29} (0.25)	1.8×10^{-25} (0.05)
⊥ 24.51	3.0×10^{-29} (0.48)	1.6×10^{-28} (0.60)	7.9×10^{-25} (0.23)
25.38	1.4×10^{-29} (0.22)	7.2×10^{-29} (0.27)	1.4×10^{-25} (0.04)
[26.47]	1.4×10^{-29} (0.22)	7.8×10^{-29} (0.29)	–
41.63	2.3×10^{-29} (0.37)	1.3×10^{-28} (0.48)	3.7×10^{-26} (0.01)
[42.88]	2.4×10^{-29} (0.38)	1.2×10^{-28} (0.45)	–
⊥ 47.27	3.1×10^{-29} (0.48)	1.7×10^{-28} (0.63)	6.3×10^{-25} (0.18)
⊥ 98.06	3.6×10^{-29} (0.57)	2.0×10^{-28} (0.75)	2.3×10^{-25} (0.07)
[121.17]	3.6×10^{-29} (0.57)	1.6×10^{-28} (0.59)	–

Table C.9. Like Table C.1 for pyrene ($C_{16}H_{10}$).

Peak (μm)	Integrated flux		
	ISRF (W sr^{-1}) (%)	Red Rectangle (W sr^{-1}) (%)	IRAS 21282+5050 (W sr^{-1}) (%)
[17.26]	3.2×10^{-30} (0.06)	1.6×10^{-28} (0.09)	–
[17.34]	3.3×10^{-30} (0.06)	1.6×10^{-28} (0.09)	–
18.20	2.0×10^{-29} (0.40)	9.4×10^{-28} (0.53)	1.2×10^{-24} (0.32)
[18.98]	3.5×10^{-30} (0.07)	1.8×10^{-28} (0.10)	–
[19.82]	4.3×10^{-30} (0.08)	1.9×10^{-28} (0.11)	–
[19.93]	4.0×10^{-30} (0.08)	1.9×10^{-28} (0.11)	–
20.00	1.9×10^{-29} (0.38)	9.0×10^{-28} (0.51)	1.1×10^{-24} (0.30)
⊥ 20.38	1.3×10^{-29} (0.26)	6.3×10^{-28} (0.36)	7.8×10^{-25} (0.21)
[21.96]	4.7×10^{-30} (0.09)	2.3×10^{-28} (0.13)	–
[24.64]	6.2×10^{-30} (0.12)	2.7×10^{-28} (0.16)	–
[25.27]	6.2×10^{-30} (0.12)	2.9×10^{-28} (0.17)	–
28.32	1.2×10^{-29} (0.24)	6.0×10^{-28} (0.34)	6.1×10^{-25} (0.16)
[38.63]	1.0×10^{-29} (0.19)	4.1×10^{-28} (0.23)	–
[40.66]	1.0×10^{-29} (0.20)	4.2×10^{-28} (0.24)	–
⊥ 47.80	2.4×10^{-29} (0.46)	1.2×10^{-27} (0.66)	1.3×10^{-24} (0.33)
[66.26]	1.4×10^{-29} (0.27)	3.9×10^{-28} (0.22)	–
⊥ 101.60	1.7×10^{-29} (0.32)	8.6×10^{-28} (0.49)	9.0×10^{-26} (0.02)

Table C.10. Like Table C.1 for the pyrene cation ($C_{16}H_{10}^+$).

Peak (μm)	Integrated flux		
	ISRF (W sr^{-1}) (%)	Red Rectangle (W sr^{-1}) (%)	IRAS 21282+5050 (W sr^{-1}) (%)
[15.02]	3.2×10^{-30} (0.05)	2.1×10^{-28} (0.07)	1.7×10^{-27} (0.00)
[17.57]	5.3×10^{-30} (0.08)	3.4×10^{-28} (0.11)	4.6×10^{-27} (0.00)
[18.30]	6.4×10^{-30} (0.10)	3.7×10^{-28} (0.12)	3.1×10^{-27} (0.00)
18.61	1.7×10^{-29} (0.25)	1×10^{-27} (0.32)	5.9×10^{-25} (0.15)
[18.99]	6.4×10^{-30} (0.10)	4.2×10^{-28} (0.13)	3.3×10^{-27} (0.00)
19.94	1.4×10^{-29} (0.22)	9.4×10^{-28} (0.29)	4.9×10^{-25} (0.12)
[20.35]	7.4×10^{-30} (0.11)	5×10^{-28} (0.16)	2.2×10^{-27} (0.00)
[21.08]	7.9×10^{-30} (0.12)	4.8×10^{-28} (0.15)	3.1×10^{-27} (0.00)
⊥ 21.47	9.8×10^{-30} (0.15)	6.6×10^{-28} (0.21)	2.7×10^{-25} (0.07)
[22.21]	9×10^{-30} (0.13)	5.4×10^{-28} (0.17)	2.6×10^{-27} (0.00)
[25.23]	1.1×10^{-29} (0.16)	6.9×10^{-28} (0.22)	–
[25.53]	1.1×10^{-29} (0.17)	6.6×10^{-28} (0.21)	–
27.90	1.9×10^{-29} (0.28)	1.3×10^{-27} (0.40)	6.3×10^{-25} (0.15)
[39.67]	1.9×10^{-29} (0.28)	1×10^{-27} (0.33)	–
[41.33]	2×10^{-29} (0.30)	1×10^{-27} (0.32)	–
⊥ 50.61	3.2×10^{-29} (0.47)	2×10^{-27} (0.64)	9.1×10^{-25} (0.23)
[68.39]	2.6×10^{-29} (0.38)	1.1×10^{-27} (0.33)	–
⊥ 98.93	3.2×10^{-29} (0.47)	2×10^{-27} (0.62)	2.5×10^{-25} (0.06)

Table C.11. Like Table C.1 for fluoranthene ($C_{16}H_{10}$).

Peak (μm)	Integrated flux		
	ISRF (W sr^{-1}) (%)	Red Rectangle (W sr^{-1}) (%)	IRAS 21282+5050 (W sr^{-1}) (%)
14.99	1.5×10^{-29} (0.30)	5.5×10^{-28} (0.38)	7.5×10^{-25} (0.27)
⊥ 15.51	3.6×10^{-29} (0.71)	1.2×10^{-27} (0.81)	1.8×10^{-24} (0.66)
16.04	3.2×10^{-30} (0.06)	1.5×10^{-28} (0.11)	1.2×10^{-25} (0.04)
[16.99]	3.0×10^{-30} (0.06)	1.3×10^{-28} (0.09)	–
17.86	3.5×10^{-30} (0.07)	1.6×10^{-28} (0.11)	6.1×10^{-26} (0.02)
17.94	4.5×10^{-30} (0.09)	2.0×10^{-28} (0.14)	1.6×10^{-25} (0.06)
⊥ 19.39	6.6×10^{-30} (0.13)	2.8×10^{-28} (0.19)	2.6×10^{-25} (0.09)
⊥ 20.61	9.1×10^{-30} (0.18)	3.6×10^{-28} (0.25)	3.9×10^{-25} (0.14)
20.65	7.1×10^{-30} (0.14)	3.0×10^{-28} (0.21)	3.0×10^{-25} (0.11)
[21.54]	5.1×10^{-30} (0.10)	2.0×10^{-28} (0.14)	–
21.57	5.6×10^{-30} (0.11)	2.3×10^{-28} (0.16)	1.1×10^{-25} (0.04)
29.12	7.8×10^{-30} (0.15)	3.4×10^{-28} (0.24)	5.1×10^{-26} (0.02)
⊥ 31.96	9.6×10^{-30} (0.19)	4.0×10^{-28} (0.28)	2.3×10^{-25} (0.08)
[32.80]	8.5×10^{-30} (0.17)	3.2×10^{-28} (0.22)	–
⊥ 43.97	1.4×10^{-29} (0.28)	6.3×10^{-28} (0.44)	5.4×10^{-25} (0.20)
47.93	1.3×10^{-29} (0.25)	5.7×10^{-28} (0.39)	3.7×10^{-25} (0.13)
[57.31]	1.3×10^{-29} (0.25)	3.6×10^{-28} (0.25)	–
⊥ 65.70	1.6×10^{-29} (0.31)	6.9×10^{-28} (0.48)	5.0×10^{-25} (0.18)

Table C.12. Like Table C.1 for the fluoranthene cation ($C_{16}H_{10}^+$).

Peak (μm)	Integrated flux		
	ISRF (W sr^{-1}) (%)	Red Rectangle (W sr^{-1}) (%)	IRAS 21282+5050 (W sr^{-1}) (%)
[15.58]	5.5×10^{-30} (0.07)	2.5×10^{-28} (0.07)	5.9×10^{-28} (0.00)
16.05	7.5×10^{-30} (0.09)	4.1×10^{-28} (0.12)	6.7×10^{-26} (0.02)
⊥ 16.18	1.9×10^{-28} (2.31)	9.8×10^{-27} (2.82)	5.1×10^{-24} (1.33)
[17.63]	8.1×10^{-30} (0.10)	3.3×10^{-28} (0.09)	1.2×10^{-28} (0.00)
17.77	4.2×10^{-29} (0.52)	2.2×10^{-27} (0.62)	1.0×10^{-24} (0.27)
17.81	1.5×10^{-29} (0.18)	7.5×10^{-28} (0.22)	2.5×10^{-25} (0.07)
20.69	3.3×10^{-29} (0.41)	1.9×10^{-27} (0.55)	7.3×10^{-25} (0.19)
21.26	2.1×10^{-29} (0.26)	1.0×10^{-27} (0.30)	3.4×10^{-25} (0.09)
⊥ 21.65	1.4×10^{-29} (0.17)	7.4×10^{-28} (0.21)	7.5×10^{-26} (0.02)
⊥ 23.24	2.3×10^{-29} (0.28)	1.3×10^{-27} (0.37)	3.8×10^{-25} (0.10)
[23.34]	1.5×10^{-29} (0.19)	5.5×10^{-28} (0.16)	–
28.74	2.1×10^{-29} (0.26)	1.1×10^{-27} (0.32)	4.1×10^{-26} (0.01)
⊥ 34.03	2.8×10^{-29} (0.35)	1.6×10^{-27} (0.45)	2.3×10^{-25} (0.06)
[39.41]	3.0×10^{-29} (0.37)	6.3×10^{-28} (0.18)	–
49.37	3.5×10^{-29} (0.43)	5.1×10^{-28} (0.15)	–
⊥ 60.35	4.7×10^{-29} (0.58)	2.5×10^{-27} (0.72)	5.4×10^{-25} (0.14)
[81.51]	4.1×10^{-29} (0.51)	3.1×10^{-28} (0.09)	–
⊥ 98.49	5.1×10^{-29} (0.62)	2.8×10^{-27} (0.81)	3.2×10^{-25} (0.08)

Table C.13. Like Table C.1 for tetracene ($C_{18}H_{12}$).

Peak (μm)	Integrated flux		
	ISRF (W sr^{-1}) (%)	Red Rectangle (W sr^{-1}) (%)	IRAS 21282+5050 (W sr^{-1}) (%)
15.63	1.6×10^{-29} (0.23)	7.1×10^{-29} (0.29)	4.4×10^{-25} (0.18)
16.31	5.3×10^{-29} (0.78)	2.3×10^{-28} (0.93)	1.5×10^{-24} (0.62)
17.93	8.5×10^{-29} (1.25)	3.8×10^{-28} (1.54)	2.5×10^{-24} (0.99)
[19.98]	2.6×10^{-30} (0.04)	1.2×10^{-29} (0.05)	–
⊥ 21.15	1.5×10^{-29} (0.23)	7.4×10^{-29} (0.30)	4.4×10^{-25} (0.18)
[21.36]	3.0×10^{-30} (0.04)	1.4×10^{-29} (0.06)	–
⊥ 21.55	1.9×10^{-28} (2.80)	8.7×10^{-28} (3.49)	5.3×10^{-24} (2.12)
22.69	5.4×10^{-30} (0.08)	2.7×10^{-29} (0.11)	9.5×10^{-26} (0.04)
[26.73]	4.8×10^{-30} (0.07)	2.5×10^{-29} (0.10)	–
[31.73]	6.8×10^{-30} (0.10)	3.3×10^{-29} (0.13)	–
[31.95]	6.8×10^{-30} (0.10)	3.2×10^{-29} (0.13)	–
[33.20]	7.4×10^{-30} (0.11)	3.6×10^{-29} (0.14)	–
⊥ 37.47	1.1×10^{-29} (0.16)	5.6×10^{-29} (0.23)	1.6×10^{-25} (0.06)
[52.27]	1.2×10^{-29} (0.18)	5.6×10^{-29} (0.22)	–
66.17	1.7×10^{-29} (0.26)	8.5×10^{-29} (0.34)	2.2×10^{-25} (0.09)
[67.60]	1.4×10^{-29} (0.21)	6.4×10^{-29} (0.26)	–
[110.11]	1.6×10^{-29} (0.24)	6.6×10^{-29} (0.26)	–
⊥ 180.44	2.1×10^{-29} (0.31)	1.0×10^{-28} (0.42)	1.9×10^{-26} (0.01)

Table C.14. Like Table C.1 for the tetracene cation ($C_{18}H_{12}^+$).

Peak (μm)	Integrated flux		
	ISRF (W sr^{-1}) (%)	Red Rectangle (W sr^{-1}) (%)	IRAS 21282+5050 (W sr^{-1}) (%)
16.23	9.9×10^{-30} (0.08)	5.1×10^{-28} (0.09)	2.1×10^{-25} (0.04)
18.16	8.7×10^{-30} (0.07)	4.9×10^{-28} (0.09)	1.4×10^{-25} (0.03)
[19.72]	6.7×10^{-30} (0.05)	3.2×10^{-28} (0.06)	–
[20.37]	7.8×10^{-30} (0.06)	3.6×10^{-28} (0.07)	–
[21.12]	8.9×10^{-30} (0.07)	4.0×10^{-28} (0.07)	–
⊥ 21.53	9.1×10^{-29} (0.73)	4.5×10^{-27} (0.83)	2.0×10^{-24} (0.37)
22.60	1.3×10^{-29} (0.11)	6.4×10^{-28} (0.12)	1.7×10^{-25} (0.03)
⊥ 22.87	1.5×10^{-28} (1.21)	7.5×10^{-27} (1.38)	3.2×10^{-24} (0.59)
[26.08]	1.6×10^{-29} (0.13)	5.9×10^{-28} (0.11)	–
[30.78]	2.0×10^{-29} (0.16)	8.6×10^{-28} (0.16)	–
[32.97]	2.1×10^{-29} (0.17)	9.4×10^{-28} (0.17)	–
[33.78]	2.3×10^{-29} (0.18)	9.0×10^{-28} (0.17)	–
⊥ 38.22	3.5×10^{-29} (0.28)	1.9×10^{-27} (0.34)	4.6×10^{-25} (0.09)
[50.82]	3.7×10^{-29} (0.30)	1.1×10^{-27} (0.20)	–
60.07	4.6×10^{-29} (0.37)	2.4×10^{-27} (0.45)	4.1×10^{-25} (0.08)
[67.32]	4.7×10^{-29} (0.38)	1.1×10^{-27} (0.19)	–
[96.38]	5.4×10^{-29} (0.43)	7.6×10^{-28} (0.14)	–
⊥ 175.31	6.7×10^{-29} (0.54)	3.4×10^{-27} (0.63)	1.7×10^{-25} (0.03)

Table C.15. Like Table C.1 for chrysene ($C_{18}H_{12}$).

Peak (μm)	Integrated flux		
	ISRF (W sr^{-1}) (%)	Red Rectangle (W sr^{-1}) (%)	IRAS 21282+5050 (W sr^{-1}) (%)
⊥ 17.26	4.1×10^{-29} (0.71)	1.4×10^{-27} (0.88)	2.7×10^{-24} (0.62)
17.53	7.2×10^{-30} (0.13)	2.3×10^{-28} (0.15)	4.3×10^{-25} (0.10)
⊥ 18.05	1.9×10^{-29} (0.33)	6.3×10^{-28} (0.41)	1.2×10^{-24} (0.27)
18.57	1.6×10^{-29} (0.29)	5.9×10^{-28} (0.38)	1.1×10^{-24} (0.25)
20.83	5.6×10^{-29} (0.99)	2.0×10^{-27} (1.26)	3.6×10^{-24} (0.83)
⊥ 23.22	4.7×10^{-29} (0.83)	1.6×10^{-27} (1.05)	3.0×10^{-24} (0.70)
[26.04]	2.8×10^{-30} (0.05)	8.6×10^{-29} (0.06)	–
[26.45]	3.0×10^{-30} (0.05)	9.4×10^{-29} (0.06)	–
⊥ 34.63	5.1×10^{-30} (0.09)	2.0×10^{-28} (0.13)	7.7×10^{-26} (0.02)
[34.66]	4.6×10^{-30} (0.08)	1.4×10^{-28} (0.09)	–
⊥ 43.01	1.6×10^{-29} (0.29)	6.0×10^{-28} (0.39)	9.4×10^{-25} (0.22)
54.14	8.5×10^{-30} (0.15)	3.3×10^{-28} (0.21)	1.6×10^{-25} (0.04)
[57.60]	8.3×10^{-30} (0.15)	1.8×10^{-28} (0.12)	–
[75.03]	9.6×10^{-30} (0.17)	1.7×10^{-28} (0.11)	–
⊥ 131.58	1.3×10^{-29} (0.22)	4.7×10^{-28} (0.30)	–
⊥ 206.15	1.4×10^{-29} (0.24)	4.8×10^{-28} (0.31)	–

Table C.16. Like Table C.1 for the chrysene cation ($C_{18}H_{12}^+$).

Peak (μm)	Integrated flux		
	ISRF (W sr^{-1}) (%)	Red Rectangle (W sr^{-1}) (%)	IRAS 21282+5050 (W sr^{-1}) (%)
17.87	5.5×10^{-29} (0.45)	3.8×10^{-27} (0.60)	1.1×10^{-24} (0.20)
⊥ 18.38	8.2×10^{-30} (0.07)	5.8×10^{-28} (0.09)	1.2×10^{-25} (0.02)
18.54	2.3×10^{-29} (0.19)	1.4×10^{-27} (0.22)	3.6×10^{-25} (0.07)
⊥ 19.44	5.1×10^{-29} (0.42)	3.2×10^{-27} (0.51)	8.8×10^{-25} (0.17)
[20.26]	5.7×10^{-30} (0.05)	1.2×10^{-28} (0.02)	–
20.86	1×10^{-28} (0.83)	6.7×10^{-27} (1.08)	1.7×10^{-24} (0.33)
[21.28]	6.7×10^{-30} (0.05)	1.9×10^{-28} (0.03)	–
[22.10]	8.1×10^{-30} (0.07)	2.2×10^{-28} (0.04)	–
⊥ 24.09	4.3×10^{-29} (0.35)	2.8×10^{-27} (0.44)	6.3×10^{-25} (0.12)
[26.95]	1.5×10^{-29} (0.12)	3×10^{-28} (0.05)	–
[27.20]	1.4×10^{-29} (0.12)	3×10^{-28} (0.05)	–
⊥ 34.64	2.9×10^{-29} (0.23)	1.8×10^{-27} (0.29)	2.8×10^{-25} (0.05)
[36.34]	2.4×10^{-29} (0.20)	4.9×10^{-28} (0.08)	–
⊥ 45.49	5.3×10^{-29} (0.43)	3.6×10^{-27} (0.57)	6×10^{-25} (0.11)
54.75	4.8×10^{-29} (0.39)	3.2×10^{-27} (0.50)	3.6×10^{-25} (0.07)
[59.57]	4.3×10^{-29} (0.35)	5×10^{-28} (0.08)	–
[78.66]	5.2×10^{-29} (0.43)	4.3×10^{-28} (0.07)	–
⊥ 136.64	6.8×10^{-29} (0.56)	4.4×10^{-27} (0.71)	6.8×10^{-26} (0.01)
⊥ 249.14	7.7×10^{-29} (0.63)	1.7×10^{-27} (0.28)	–

Table C.17. Like Table C.1 for perylene ($C_{20}H_{12}$).

Peak (μm)	Integrated flux		
	ISRF (W sr^{-1}) (%)	Red Rectangle (W sr^{-1}) (%)	IRAS 21282+5050 (W sr^{-1}) (%)
17.21	4.6×10^{-29} (0.59)	3.0×10^{-27} (0.79)	1.9×10^{-24} (0.42)
⊥ 18.36	9.4×10^{-29} (1.20)	6.0×10^{-27} (1.60)	3.8×10^{-24} (0.83)
18.63	1.6×10^{-29} (0.20)	8.9×10^{-28} (0.24)	6.0×10^{-25} (0.13)
⊥ 21.19	5.1×10^{-30} (0.06)	3.4×10^{-28} (0.09)	1.5×10^{-25} (0.03)
21.76	2.0×10^{-29} (0.26)	1.4×10^{-27} (0.38)	8.3×10^{-25} (0.18)
[23.94]	3.6×10^{-30} (0.05)	1.6×10^{-28} (0.04)	–
[27.75]	5.1×10^{-30} (0.07)	2.2×10^{-28} (0.06)	–
[28.48]	5.3×10^{-30} (0.07)	2.5×10^{-28} (0.07)	–
[34.30]	7.7×10^{-30} (0.10)	3.2×10^{-28} (0.09)	–
39.63	9.4×10^{-30} (0.12)	5.6×10^{-28} (0.15)	–
[42.43]	1.1×10^{-29} (0.14)	3.7×10^{-28} (0.10)	–
[48.89]	1.2×10^{-29} (0.16)	3.7×10^{-28} (0.10)	–
⊥ 57.14	2.7×10^{-29} (0.35)	1.9×10^{-27} (0.49)	7.3×10^{-25} (0.16)
[77.69]	1.6×10^{-29} (0.21)	3.0×10^{-28} (0.08)	–
⊥ 105.54	2.0×10^{-29} (0.26)	1.4×10^{-27} (0.38)	7.1×10^{-26} (0.02)
[344.80]	1.4×10^{-29} (0.18)	3.1×10^{-29} (0.01)	–

Table C.18. Like Table C.1 for the perylene cation ($C_{20}H_{12}^+$).

Peak (μm)	Integrated flux		
	ISRF (W sr^{-1}) (%)	Red Rectangle (W sr^{-1}) (%)	IRAS 21282+5050 (W sr^{-1}) (%)
17.41	7.4×10^{-29} (0.71)	4.1×10^{-27} (0.86)	3.0×10^{-24} (0.48)
⊥ 18.75	1.0×10^{-28} (1.00)	6.0×10^{-27} (1.24)	4.1×10^{-24} (0.65)
18.99	2.7×10^{-29} (0.26)	1.6×10^{-27} (0.32)	1.1×10^{-24} (0.17)
⊥ 21.54	9.8×10^{-30} (0.09)	5.8×10^{-28} (0.12)	3.0×10^{-25} (0.05)
21.95	1.4×10^{-29} (0.13)	7.8×10^{-28} (0.16)	4.3×10^{-25} (0.07)
[22.04]	4.7×10^{-30} (0.05)	2.1×10^{-28} (0.04)	–
[23.38]	5.6×10^{-30} (0.05)	3.0×10^{-28} (0.06)	–
[24.23]	5.8×10^{-30} (0.06)	3.4×10^{-28} (0.07)	–
[27.67]	8.5×10^{-30} (0.08)	4.1×10^{-28} (0.09)	–
[28.49]	9.4×10^{-30} (0.09)	4.4×10^{-28} (0.09)	–
[35.52]	1.3×10^{-29} (0.13)	5.8×10^{-28} (0.12)	–
39.35	1.9×10^{-29} (0.18)	1.2×10^{-27} (0.26)	3.5×10^{-25} (0.06)
[40.73]	1.6×10^{-29} (0.16)	6.3×10^{-28} (0.13)	–
[48.48]	2.0×10^{-29} (0.19)	6.8×10^{-28} (0.14)	–
⊥ 57.15	4.3×10^{-29} (0.42)	2.8×10^{-27} (0.58)	1.2×10^{-24} (0.19)
[67.82]	2.5×10^{-29} (0.24)	6.1×10^{-28} (0.13)	–
⊥ 98.04	3.4×10^{-29} (0.32)	2.2×10^{-27} (0.45)	4.1×10^{-25} (0.07)
[247.44]	3.0×10^{-29} (0.29)	1.1×10^{-28} (0.02)	–

Table C.19. Like Table C.1 for pentacene ($C_{22}H_{14}$).

Peak (μm)	Integrated flux		
	ISRF (W sr^{-1}) (%)	Red Rectangle (W sr^{-1}) (%)	IRAS 21282+5050 (W sr^{-1}) (%)
15.78	5.8×10^{-29} (0.65)	2.6×10^{-27} (0.75)	2.6×10^{-24} (0.55)
17.39	1.3×10^{-28} (1.45)	6.1×10^{-27} (1.74)	5.5×10^{-24} (1.16)
20.75	8.6×10^{-29} (0.95)	3.9×10^{-27} (1.12)	3.4×10^{-24} (0.72)
⊥ 21.38	6.4×10^{-29} (0.71)	3.0×10^{-27} (0.85)	2.6×10^{-24} (0.55)
⊥ 21.72	2.4×10^{-28} (2.65)	1.1×10^{-26} (3.11)	9.5×10^{-24} (1.99)
28.18	7.6×10^{-30} (0.08)	3.4×10^{-28} (0.10)	2.2×10^{-25} (0.05)
[34.69]	4.2×10^{-30} (0.05)	1.4×10^{-28} (0.04)	–
[39.34]	5.3×10^{-30} (0.06)	1.5×10^{-28} (0.04)	–
[41.72]	5.9×10^{-30} (0.07)	1.7×10^{-28} (0.05)	–
[43.10]	6.3×10^{-30} (0.07)	1.6×10^{-28} (0.05)	8.4×10^{-29} (0.00)
⊥ 52.61	1.2×10^{-29} (0.13)	5.8×10^{-28} (0.16)	2.0×10^{-25} (0.04)
[66.95]	1.1×10^{-29} (0.12)	1.7×10^{-28} (0.05)	3.8×10^{-28} (0.00)
98.26	1.5×10^{-29} (0.16)	7.1×10^{-28} (0.20)	2.9×10^{-26} (0.01)
[99.27]	1.3×10^{-29} (0.15)	1.3×10^{-28} (0.04)	–
[137.59]	1.4×10^{-29} (0.16)	8.7×10^{-29} (0.02)	–
⊥ 267.28	2.1×10^{-29} (0.23)	9×10^{-28} (0.25)	–

Table C.20. Like Table C.1 for the pentacene cation ($C_{22}H_{14}^+$).

Peak (μm)	Integrated flux		
	ISRF (W sr^{-1}) (%)	Red Rectangle (W sr^{-1}) (%)	IRAS 21282+5050 (W sr^{-1}) (%)
17.37	3.3×10^{-29} (0.15)	1.8×10^{-27} (0.16)	4.7×10^{-25} (0.06)
⊥ 20.63	1.6×10^{-28} (0.76)	9.7×10^{-27} (0.89)	2.3×10^{-24} (0.30)
⊥ 21.94	6.9×10^{-28} (3.20)	4.0×10^{-26} (3.71)	9.4×10^{-24} (1.22)
⊥ 25.93	1.1×10^{-29} (0.05)	6.3×10^{-28} (0.06)	5.1×10^{-26} (0.01)
27.66	1.5×10^{-29} (0.07)	9.1×10^{-28} (0.08)	1×10^{-25} (0.01)
[27.87]	1.2×10^{-29} (0.05)	2.3×10^{-28} (0.02)	–
[35.10]	2.1×10^{-29} (0.10)	3.8×10^{-28} (0.03)	–
[40.11]	2.6×10^{-29} (0.12)	4.5×10^{-28} (0.04)	–
[40.71]	2.8×10^{-29} (0.13)	4.5×10^{-28} (0.04)	–
[41.70]	2.8×10^{-29} (0.13)	4.2×10^{-28} (0.04)	–
⊥ 52.73	6.1×10^{-29} (0.28)	3.5×10^{-27} (0.32)	4.6×10^{-25} (0.06)
[62.41]	4.7×10^{-29} (0.22)	4.9×10^{-28} (0.05)	–
86.88	7.9×10^{-29} (0.37)	4.7×10^{-27} (0.43)	4.5×10^{-25} (0.06)
[100.30]	6.5×10^{-29} (0.30)	3.1×10^{-28} (0.03)	–
[110.73]	6.6×10^{-29} (0.31)	2.9×10^{-28} (0.03)	–
⊥ 474.50	1.1×10^{-28} (0.49)	3.7×10^{-27} (0.34)	–

Table C.21. Like Table C.1 for benzo[g,h,i]perylene ($C_{22}H_{12}$).

Peak (μm)	Integrated flux		
	ISRF (W sr^{-1}) (%)	Red Rectangle (W sr^{-1}) (%)	IRAS 21282+5050 (W sr^{-1}) (%)
⊥ 15.41	1.1×10^{-28} (1.49)	5.8×10^{-27} (1.94)	6.0×10^{-24} (1.19)
17.68	3.0×10^{-29} (0.41)	1.6×10^{-27} (0.55)	1.6×10^{-24} (0.31)
⊥ 18.40	7.2×10^{-29} (0.98)	3.9×10^{-27} (1.31)	3.9×10^{-24} (0.77)
18.62	5.2×10^{-30} (0.07)	2.4×10^{-28} (0.08)	2.3×10^{-25} (0.05)
⊥ 19.44	4.7×10^{-29} (0.64)	2.6×10^{-27} (0.87)	2.6×10^{-24} (0.51)
20.82	4.4×10^{-30} (0.06)	2.6×10^{-28} (0.09)	1.7×10^{-25} (0.03)
22.16	1.9×10^{-29} (0.26)	1.1×10^{-27} (0.35)	9.3×10^{-25} (0.18)
⊥ 23.56	3.1×10^{-30} (0.04)	2.2×10^{-28} (0.07)	3.8×10^{-26} (0.01)
24.43	1.6×10^{-29} (0.21)	8.1×10^{-28} (0.27)	7.3×10^{-25} (0.14)
26.12	4.7×10^{-30} (0.06)	2.9×10^{-28} (0.10)	9.4×10^{-26} (0.02)
27.65	5.3×10^{-30} (0.07)	3.1×10^{-28} (0.10)	7.9×10^{-26} (0.02)
⊥ 34.15	6.3×10^{-30} (0.08)	4×10^{-28} (0.13)	–
[34.37]	6.2×10^{-30} (0.08)	2.0×10^{-28} (0.07)	–
35.04	8.2×10^{-30} (0.11)	4.6×10^{-28} (0.15)	1.4×10^{-25} (0.03)
[36.35]	7.4×10^{-30} (0.10)	2.2×10^{-28} (0.07)	–
⊥ 49.73	1.6×10^{-29} (0.22)	9.6×10^{-28} (0.32)	5.2×10^{-25} (0.10)
[55.73]	1.1×10^{-29} (0.15)	2.3×10^{-28} (0.08)	–
⊥ 76.15	1.9×10^{-29} (0.26)	1.1×10^{-27} (0.38)	5.0×10^{-25} (0.10)
⊥ 105.47	1.6×10^{-29} (0.22)	1.0×10^{-27} (0.34)	3.4×10^{-26} (0.01)
[167.79]	1.4×10^{-29} (0.19)	5.2×10^{-29} (0.02)	–

Table C.22. Like Table C.1 for the benzo[g,h,i]perylene cation ($C_{22}H_{12}^+$).

Peak (μm)	Integrated flux		
	ISRF (W sr^{-1}) (%)	Red Rectangle (W sr^{-1}) (%)	IRAS 21282+5050 (W sr^{-1}) (%)
\perp 15.56	1.9×10^{-28} (1.63)	1.0×10^{-26} (1.99)	7.2×10^{-24} (1.07)
\parallel 15.96	5.3×10^{-30} (0.05)	2.6×10^{-28} (0.05)	1.3×10^{-25} (0.02)
\parallel 17.82	2.6×10^{-29} (0.22)	1.3×10^{-27} (0.25)	8.6×10^{-25} (0.13)
\perp 18.62	1.2×10^{-28} (1.02)	6.4×10^{-27} (1.28)	4.3×10^{-24} (0.63)
\parallel 18.94	1.2×10^{-29} (0.10)	6.0×10^{-28} (0.12)	3.6×10^{-25} (0.05)
\parallel 18.95	1.4×10^{-29} (0.12)	7.7×10^{-28} (0.15)	4.2×10^{-25} (0.06)
\parallel 20.84	1.2×10^{-29} (0.10)	7.7×10^{-28} (0.15)	3.4×10^{-25} (0.05)
[22.24]	6.7×10^{-30} (0.06)	2.7×10^{-28} (0.05)	–
\parallel 22.50	1.4×10^{-29} (0.12)	8.1×10^{-28} (0.16)	3.6×10^{-25} (0.05)
\perp 23.75	8.6×10^{-30} (0.07)	4.8×10^{-28} (0.10)	5.7×10^{-26} (0.01)
\parallel 24.18	8.9×10^{-30} (0.08)	5.3×10^{-28} (0.11)	8.1×10^{-26} (0.01)
\parallel 25.93	1.2×10^{-29} (0.10)	7.1×10^{-28} (0.14)	2.3×10^{-25} (0.03)
\parallel 27.93	2.1×10^{-29} (0.18)	1.2×10^{-27} (0.24)	5.4×10^{-25} (0.08)
\perp 33.76	1.8×10^{-29} (0.15)	1.0×10^{-27} (0.20)	1.7×10^{-25} (0.03)
\parallel 34.33	2.1×10^{-29} (0.18)	1.2×10^{-27} (0.24)	4.0×10^{-25} (0.06)
[35.26]	1.8×10^{-29} (0.15)	5.3×10^{-28} (0.11)	–
[35.59]	1.8×10^{-29} (0.15)	5.3×10^{-28} (0.11)	–
\perp 49.35	3.5×10^{-29} (0.30)	2.0×10^{-27} (0.39)	6.9×10^{-25} (0.10)
[52.23]	2.6×10^{-29} (0.22)	5.1×10^{-28} (0.10)	–
\perp 72.14	5.0×10^{-29} (0.43)	2.8×10^{-27} (0.56)	1.1×10^{-24} (0.16)
\perp 101.69	4.2×10^{-29} (0.36)	2.4×10^{-27} (0.48)	1.8×10^{-25} (0.03)
[149.24]	3.7×10^{-29} (0.32)	1.6×10^{-28} (0.03)	–

Table C.23. Like Table C.1 for anthanthrene ($C_{22}H_{12}$).

Peak (μm)	Integrated flux		
	ISRF (W sr^{-1}) (%)	Red Rectangle (W sr^{-1}) (%)	IRAS 21282+5050 (W sr^{-1}) (%)
\parallel 16.59	7.4×10^{-29} (0.87)	4.5×10^{-27} (1.07)	3.1×10^{-24} (0.62)
\perp 17.73	2.5×10^{-29} (0.29)	1.5×10^{-27} (0.35)	9.7×10^{-25} (0.20)
\parallel 17.90	4.0×10^{-29} (0.47)	2.5×10^{-27} (0.59)	1.6×10^{-24} (0.33)
\perp 18.41	5.5×10^{-29} (0.64)	3.5×10^{-27} (0.82)	2.3×10^{-24} (0.46)
\parallel 20.14	2.1×10^{-29} (0.25)	1.4×10^{-27} (0.33)	8.0×10^{-25} (0.16)
\perp 20.67	2.9×10^{-29} (0.34)	1.7×10^{-27} (0.41)	1.1×10^{-24} (0.23)
\parallel 21.27	3.2×10^{-29} (0.37)	2.0×10^{-27} (0.48)	1.2×10^{-24} (0.25)
[22.18]	3.9×10^{-30} (0.05)	1.9×10^{-28} (0.04)	–
[25.66]	5.4×10^{-30} (0.06)	2.6×10^{-28} (0.06)	–
[26.19]	5.5×10^{-30} (0.06)	2.4×10^{-28} (0.06)	–
[29.45]	6.9×10^{-30} (0.08)	2.8×10^{-28} (0.07)	–
\perp 32.18	1.1×10^{-29} (0.13)	7.3×10^{-28} (0.17)	1.9×10^{-25} (0.04)
\perp 34.88	1.1×10^{-29} (0.12)	6.8×10^{-28} (0.16)	4.7×10^{-26} (0.01)
[35.51]	9.9×10^{-30} (0.12)	3.4×10^{-28} (0.08)	–
\parallel 38.22	2.9×10^{-29} (0.35)	1.9×10^{-27} (0.46)	9.6×10^{-25} (0.20)
[50.48]	1.4×10^{-29} (0.17)	3.6×10^{-28} (0.09)	–
\perp 54.39	3.4×10^{-29} (0.40)	2.3×10^{-27} (0.54)	1.1×10^{-24} (0.22)
[62.57]	1.7×10^{-29} (0.20)	3.1×10^{-28} (0.07)	–
\perp 103.84	2.4×10^{-29} (0.28)	1.6×10^{-27} (0.39)	6.2×10^{-26} (0.01)
\perp 153.88	2.7×10^{-29} (0.32)	1.8×10^{-27} (0.42)	2.8×10^{-26} (0.01)

Table C.24. Like Table C.1 for the anthanthrene cation ($C_{22}H_{12}^+$).

Peak (μm)	Integrated flux		
	ISRF (W sr^{-1}) (%)	Red Rectangle (W sr^{-1}) (%)	IRAS 21282+5050 (W sr^{-1}) (%)
16.80	4.0×10^{-29} (0.33)	2.3×10^{-27} (0.41)	1.2×10^{-24} (0.18)
17.85	1.0×10^{-29} (0.09)	5.6×10^{-28} (0.10)	3×10^{-25} (0.04)
⊥ 17.98	4.3×10^{-29} (0.36)	2.6×10^{-27} (0.46)	1.3×10^{-24} (0.19)
20.08	3.3×10^{-29} (0.27)	1.9×10^{-27} (0.34)	9.3×10^{-25} (0.14)
[20.45]	5.6×10^{-30} (0.05)	3.1×10^{-28} (0.05)	–
⊥ 21.36	1.9×10^{-29} (0.16)	1.3×10^{-27} (0.22)	5.1×10^{-25} (0.07)
21.37	3.4×10^{-29} (0.28)	2×10^{-27} (0.35)	9.1×10^{-25} (0.13)
[22.73]	7.1×10^{-30} (0.06)	3.6×10^{-28} (0.06)	–
[25.48]	1.1×10^{-29} (0.09)	5.1×10^{-28} (0.09)	–
[27.64]	1.1×10^{-29} (0.09)	6×10^{-28} (0.11)	–
[29.96]	1.4×10^{-29} (0.11)	6.1×10^{-28} (0.11)	–
⊥ 32.23	1.7×10^{-29} (0.14)	9.7×10^{-28} (0.17)	7.5×10^{-26} (0.01)
⊥ 35.42	2.0×10^{-29} (0.17)	1.3×10^{-27} (0.22)	2.4×10^{-25} (0.04)
[36.05]	1.9×10^{-29} (0.16)	8.4×10^{-28} (0.15)	–
41.40	4.3×10^{-29} (0.35)	2.7×10^{-27} (0.48)	9.2×10^{-25} (0.14)
[51.25]	2.8×10^{-29} (0.23)	9.9×10^{-28} (0.17)	–
⊥ 55.94	4.5×10^{-29} (0.37)	2.8×10^{-27} (0.49)	8.9×10^{-25} (0.13)
[62.60]	3.2×10^{-29} (0.26)	1×10^{-27} (0.18)	–
⊥ 105.06	4.5×10^{-29} (0.37)	2.7×10^{-27} (0.47)	9.2×10^{-26} (0.01)
⊥ 150.86	5.1×10^{-29} (0.42)	3.1×10^{-27} (0.54)	1.1×10^{-25} (0.02)

Table C.25. Like Table C.1 for coronene ($C_{24}H_{12}$).

Peak (μm)	Integrated flux		
	ISRF (W sr^{-1}) (%)	Red Rectangle (W sr^{-1}) (%)	IRAS 21282+5050 (W sr^{-1}) (%)
⊥ 18.21	3.4×10^{-28} (4.24)	1.2×10^{-26} (5.29)	1.9×10^{-23} (3.41)
[20.07]	3.2×10^{-30} (0.04)	1.3×10^{-28} (0.06)	–
[22.28]	5.3×10^{-30} (0.07)	1.8×10^{-28} (0.08)	–
26.20	2.5×10^{-29} (0.31)	9.7×10^{-28} (0.42)	1.2×10^{-24} (0.22)
[27.34]	8.3×10^{-30} (0.10)	3.1×10^{-28} (0.13)	–
[33.59]	1.2×10^{-29} (0.15)	4.1×10^{-28} (0.18)	–
[34.34]	1.3×10^{-29} (0.17)	4.4×10^{-28} (0.19)	–
[44.57]	8.8×10^{-30} (0.11)	2.9×10^{-28} (0.12)	–
[61.10]	1.2×10^{-29} (0.15)	3.1×10^{-28} (0.13)	–
⊥ 80.60	2.2×10^{-29} (0.27)	8.4×10^{-28} (0.36)	7.2×10^{-25} (0.13)
[113.37]	2.8×10^{-29} (0.36)	4.2×10^{-28} (0.18)	–

Table C.26. Like Table C.1 for the coronene cation ($C_{24}H_{12}^+$).

Peak (μm)	Integrated flux		
	ISRF (W sr^{-1}) (%)	Red Rectangle (W sr^{-1}) (%)	IRAS 21282+5050 (W sr^{-1}) (%)
15.13	8.5×10^{-29} (0.68)	4.4×10^{-27} (0.88)	2.8×10^{-24} (0.40)
18.08	1.4×10^{-28} (1.14)	7.4×10^{-27} (1.50)	4.3×10^{-24} (0.62)
⊥ 18.14	1.4×10^{-28} (1.12)	7.1×10^{-27} (1.44)	4.1×10^{-24} (0.59)
⊥ 19.39	1.1×10^{-29} (0.09)	5.9×10^{-28} (0.12)	2.8×10^{-25} (0.04)
21.36	6.3×10^{-30} (0.05)	3.1×10^{-28} (0.06)	–
[22.94]	6.7×10^{-30} (0.05)	2.9×10^{-28} (0.06)	–
[23.13]	6.7×10^{-30} (0.05)	3.1×10^{-28} (0.06)	–
26.05	2.9×10^{-29} (0.24)	1.5×10^{-27} (0.31)	7.4×10^{-25} (0.11)
26.34	3.4×10^{-29} (0.28)	1.8×10^{-27} (0.36)	9.0×10^{-25} (0.13)
[27.48]	1.1×10^{-29} (0.09)	4.4×10^{-28} (0.09)	–
[28.17]	1.1×10^{-29} (0.09)	4.5×10^{-28} (0.09)	–
[34.15]	1.6×10^{-29} (0.13)	6.8×10^{-28} (0.14)	–
[34.44]	1.6×10^{-29} (0.13)	6.6×10^{-28} (0.13)	–
⊥ 34.56	1.7×10^{-29} (0.13)	9.2×10^{-28} (0.19)	5.7×10^{-26} (0.01)
[36.27]	1.7×10^{-29} (0.14)	7.0×10^{-28} (0.14)	–
[45.64]	2.3×10^{-29} (0.18)	8.8×10^{-28} (0.18)	–
[63.12]	3.2×10^{-29} (0.25)	9.8×10^{-28} (0.20)	–
⊥ 82.64	4.5×10^{-29} (0.36)	2.4×10^{-27} (0.49)	7.9×10^{-25} (0.11)
[111.53]	4.0×10^{-29} (0.32)	7.2×10^{-28} (0.15)	–
⊥ 117.33	4.4×10^{-29} (0.35)	1.9×10^{-27} (0.38)	–

Table C.27. Like Table C.1 for dibenzo[cd,lm]perylene ($C_{26}H_{14}$).

Peak (μm)	Integrated flux		
	ISRF (W sr^{-1}) (%)	Red Rectangle (W sr^{-1}) (%)	IRAS 21282+5050 (W sr^{-1}) (%)
15.05	6.1×10^{-29} (0.42)	5.2×10^{-27} (0.52)	1.5×10^{-24} (0.27)
⊥ 15.10	5.9×10^{-28} (4.12)	4.8×10^{-26} (4.85)	1.4×10^{-23} (2.56)
18.30	1.4×10^{-28} (0.99)	1.2×10^{-26} (1.20)	2.9×10^{-24} (0.52)
19.45	8.0×10^{-30} (0.06)	5.8×10^{-28} (0.06)	1.3×10^{-25} (0.02)
⊥ 19.57	6.5×10^{-29} (0.45)	5.7×10^{-27} (0.57)	1.4×10^{-24} (0.24)
⊥ 20.13	5.7×10^{-29} (0.39)	4.9×10^{-27} (0.49)	1.2×10^{-24} (0.21)
22.21	6.1×10^{-29} (0.42)	5.4×10^{-27} (0.54)	1.1×10^{-24} (0.20)
[29.46]	6.8×10^{-30} (0.05)	1.5×10^{-28} (0.01)	–
[30.08]	7.3×10^{-30} (0.05)	1.6×10^{-28} (0.02)	–
[31.77]	8.9×10^{-30} (0.06)	1.7×10^{-28} (0.02)	–
[35.42]	1.1×10^{-29} (0.08)	1.7×10^{-28} (0.02)	–
⊥ 44.52	7.6×10^{-29} (0.53)	6.7×10^{-27} (0.67)	1.1×10^{-24} (0.19)
[47.28]	1.8×10^{-29} (0.13)	2.2×10^{-28} (0.02)	–
[51.83]	2.0×10^{-29} (0.14)	1.5×10^{-28} (0.02)	–
⊥ 53.43	7.8×10^{-29} (0.54)	7.0×10^{-27} (0.71)	1×10^{-24} (0.18)
54.05	3.5×10^{-29} (0.24)	3.2×10^{-27} (0.32)	2.6×10^{-25} (0.05)
[58.60]	2.4×10^{-29} (0.17)	1.6×10^{-28} (0.02)	–
[103.09]	3.2×10^{-29} (0.22)	1.1×10^{-28} (0.01)	–
[217.08]	2.5×10^{-29} (0.17)	3.2×10^{-29} (0.00)	–
⊥ 223.26	5.5×10^{-29} (0.38)	2.9×10^{-27} (0.29)	–

Table C.28. Like Table C.1 for the dibenzo[cd,lm]perylene cation ($C_{26}H_{14}^+$).

Peak (μm)	Integrated flux		
	ISRF (W sr^{-1}) (%)	Red Rectangle (W sr^{-1}) (%)	IRAS 21282+5050 (W sr^{-1}) (%)
\perp 15.12	2.6×10^{-28} (1.48)	1.5×10^{-26} (1.74)	6.2×10^{-24} (0.78)
\parallel 18.01	1.7×10^{-29} (0.10)	1.1×10^{-27} (0.13)	3.6×10^{-25} (0.04)
\parallel 19.53	2.6×10^{-29} (0.15)	1.7×10^{-27} (0.20)	5.5×10^{-25} (0.07)
\perp 20.78	5.2×10^{-29} (0.30)	3.3×10^{-27} (0.39)	1.1×10^{-24} (0.13)
\parallel 20.90	9.3×10^{-30} (0.05)	5.1×10^{-28} (0.06)	1.5×10^{-25} (0.02)
\parallel 22.17	1.0×10^{-29} (0.06)	5.8×10^{-28} (0.07)	1.7×10^{-25} (0.02)
[29.97]	9.3×10^{-30} (0.05)	3.0×10^{-28} (0.04)	–
[30.48]	8.9×10^{-30} (0.05)	3.3×10^{-28} (0.04)	–
[30.80]	8.5×10^{-30} (0.05)	3.0×10^{-28} (0.04)	–
[37.19]	1.4×10^{-29} (0.08)	4.6×10^{-28} (0.05)	–
\perp 45.12	5.1×10^{-29} (0.30)	3.0×10^{-27} (0.36)	7.4×10^{-25} (0.09)
[50.25]	2.3×10^{-29} (0.13)	5.5×10^{-28} (0.07)	–
[51.70]	2.3×10^{-29} (0.13)	6.1×10^{-28} (0.07)	–
\parallel 53.15	3.1×10^{-29} (0.18)	1.9×10^{-27} (0.22)	2.6×10^{-25} (0.03)
\perp 53.39	8.8×10^{-29} (0.51)	5.3×10^{-27} (0.62)	1.4×10^{-24} (0.18)
[58.72]	2.5×10^{-29} (0.14)	6.3×10^{-28} (0.07)	–
[100.15]	4.0×10^{-29} (0.23)	4.5×10^{-28} (0.05)	–
\perp 211.25	5.6×10^{-29} (0.32)	3.0×10^{-27} (0.35)	–
[226.29]	4.2×10^{-29} (0.24)	1.4×10^{-28} (0.02)	–

Table C.29. Like Table C.1 for bisanthene ($C_{28}H_{14}$).

Peak (μm)	Integrated flux		
	ISRF (W sr^{-1}) (%)	Red Rectangle (W sr^{-1}) (%)	IRAS 21282+5050 (W sr^{-1}) (%)
\parallel 15.10	1.7×10^{-28} (1.12)	8.5×10^{-27} (1.33)	3.7×10^{-24} (0.63)
\parallel 15.78	7.1×10^{-29} (0.47)	3.4×10^{-27} (0.53)	1.5×10^{-24} (0.26)
\perp 16.97	1.7×10^{-29} (0.11)	8.5×10^{-28} (0.13)	3.0×10^{-25} (0.05)
\parallel 17.93	5.3×10^{-29} (0.35)	2.7×10^{-27} (0.42)	9.9×10^{-25} (0.17)
\perp 18.53	2.2×10^{-28} (1.45)	1.1×10^{-26} (1.73)	4.1×10^{-24} (0.71)
\parallel 19.95	1.4×10^{-28} (0.95)	6.9×10^{-27} (1.07)	2.5×10^{-24} (0.43)
\parallel 22.22	1.6×10^{-29} (0.10)	8.1×10^{-28} (0.13)	2.3×10^{-25} (0.04)
\perp 24.57	2.4×10^{-29} (0.16)	1.3×10^{-27} (0.21)	4.3×10^{-25} (0.07)
[32.50]	9.3×10^{-30} (0.06)	2.0×10^{-28} (0.03)	–
[32.65]	9.2×10^{-30} (0.06)	2.0×10^{-28} (0.03)	–
\parallel 32.93	1.8×10^{-28} (1.17)	9.0×10^{-27} (1.40)	2.6×10^{-24} (0.44)
\perp 35.85	1.3×10^{-29} (0.09)	6.5×10^{-28} (0.10)	–
\parallel 35.87	1.4×10^{-29} (0.09)	7.1×10^{-28} (0.11)	3.5×10^{-26} (0.01)
[39.61]	1.4×10^{-29} (0.09)	3.1×10^{-28} (0.05)	–
[41.80]	1.5×10^{-29} (0.10)	2.7×10^{-28} (0.04)	–
[57.33]	2.5×10^{-29} (0.16)	2.6×10^{-28} (0.04)	–
[66.34]	2.9×10^{-29} (0.19)	2.8×10^{-28} (0.04)	–
\perp 94.43	5.7×10^{-29} (0.38)	2.9×10^{-27} (0.45)	3.5×10^{-25} (0.06)
\perp 120.24	4.8×10^{-29} (0.31)	2.0×10^{-27} (0.31)	–
[123.19]	3.6×10^{-29} (0.24)	1.3×10^{-28} (0.02)	–
[300.07]	2.3×10^{-29} (0.15)	3.4×10^{-29} (0.01)	–

Table C.30. Like Table C.1 for the bisanthene cation ($C_{28}H_{14}^+$).

Peak (μm)	Integrated flux		
	ISRF (W sr^{-1}) (%)	Red Rectangle (W sr^{-1}) (%)	IRAS 21282+5050 (W sr^{-1}) (%)
15.04	1.2×10^{-28} (0.68)	7.1×10^{-27} (0.88)	2.8×10^{-24} (0.29)
⊥ 16.42	4.8×10^{-29} (0.27)	2.8×10^{-27} (0.35)	1.1×10^{-24} (0.12)
17.07	3.6×10^{-28} (2.03)	2.2×10^{-26} (2.71)	7.9×10^{-24} (0.84)
⊥ 18.02	1.7×10^{-28} (0.94)	1.0×10^{-26} (1.28)	3.4×10^{-24} (0.36)
[19.20]	5.3×10^{-29} (0.30)	3.0×10^{-27} (0.38)	1.1×10^{-24} (0.11)
⊥ 23.76	2.9×10^{-29} (0.16)	1.9×10^{-27} (0.23)	4.9×10^{-25} (0.05)
[28.08]	8.3×10^{-30} (0.05)	4.8×10^{-28} (0.06)	–
[28.94]	1.0×10^{-29} (0.06)	4.6×10^{-28} (0.06)	–
[29.48]	9.0×10^{-30} (0.05)	4.8×10^{-28} (0.06)	–
30.50	1.1×10^{-29} (0.06)	5.4×10^{-28} (0.07)	–
[30.57]	1.0×10^{-29} (0.06)	5.7×10^{-28} (0.07)	–
[30.81]	1.1×10^{-29} (0.06)	5.4×10^{-28} (0.07)	–
32.95	1.4×10^{-29} (0.08)	6.5×10^{-28} (0.08)	–
⊥ 33.71	1.4×10^{-29} (0.08)	6.5×10^{-28} (0.08)	–
[38.14]	1.8×10^{-29} (0.10)	7.7×10^{-28} (0.10)	–
[41.36]	2.1×10^{-29} (0.12)	9.5×10^{-28} (0.12)	–
[52.19]	2.9×10^{-29} (0.17)	9.7×10^{-28} (0.12)	–
[64.37]	3.7×10^{-29} (0.21)	1.1×10^{-27} (0.13)	–
⊥ 92.83	7.0×10^{-29} (0.39)	4.4×10^{-27} (0.55)	6.6×10^{-25} (0.07)
[102.04]	5.1×10^{-29} (0.28)	7.5×10^{-28} (0.09)	–
⊥ 116.07	5.5×10^{-29} (0.31)	6.4×10^{-28} (0.08)	–
[239.31]	5.8×10^{-29} (0.32)	2.5×10^{-28} (0.03)	–

Table C.31. Like Table C.1 for terrylene ($C_{30}H_{16}$).

Peak (μm)	Integrated flux		
	ISRF (W sr^{-1}) (%)	Red Rectangle (W sr^{-1}) (%)	IRAS 21282+5050 (W sr^{-1}) (%)
\perp 17.82	2.8×10^{-28} (1.22)	1.4×10^{-26} (1.32)	3.6×10^{-24} (0.55)
[18.82]	5.9×10^{-29} (0.26)	3.0×10^{-27} (0.29)	7.3×10^{-25} (0.11)
\parallel 19.47	2.3×10^{-28} (0.98)	1.2×10^{-26} (1.14)	2.7×10^{-24} (0.42)
\parallel 21.27	2.5×10^{-28} (1.10)	1.3×10^{-26} (1.24)	2.7×10^{-24} (0.42)
\perp 37.56	1.1×10^{-28} (0.48)	5.8×10^{-27} (0.55)	7.3×10^{-25} (0.11)
[41.19]	8.2×10^{-30} (0.04)	7.7×10^{-29} (0.01)	–
[45.95]	1.1×10^{-29} (0.05)	9.2×10^{-29} (0.01)	–
[47.77]	1.2×10^{-29} (0.05)	9.6×10^{-29} (0.01)	–
\perp 57.55	2.6×10^{-28} (1.12)	1.3×10^{-26} (1.26)	1.4×10^{-24} (0.21)
[61.21]	2.0×10^{-29} (0.09)	8.9×10^{-29} (0.01)	–
\parallel 67.52	4.8×10^{-29} (0.21)	2.5×10^{-27} (0.24)	1.3×10^{-25} (0.02)
\perp 88.43	3.8×10^{-29} (0.17)	1.7×10^{-27} (0.16)	–
[91.34]	2.6×10^{-29} (0.11)	5.0×10^{-29} (0.00)	–
\perp 271.11	6.5×10^{-29} (0.28)	1.5×10^{-27} (0.14)	–
[306.54]	1.5×10^{-29} (0.07)	–	–

Table C.32. Like Table C.1 for the terrylene cation ($C_{30}H_{16}^+$).

Peak (μm)	Integrated flux		
	ISRF (W sr^{-1}) (%)	Red Rectangle (W sr^{-1}) (%)	IRAS 21282+5050 (W sr^{-1}) (%)
\parallel 15.00	8.0×10^{-29} (0.28)	3.9×10^{-27} (0.31)	1.4×10^{-24} (0.13)
\perp 18.03	1.6×10^{-28} (0.57)	7.9×10^{-27} (0.64)	2.5×10^{-24} (0.22)
\parallel 19.02	1.8×10^{-29} (0.06)	7.9×10^{-28} (0.06)	2.9×10^{-25} (0.03)
\parallel 19.36	6.8×10^{-29} (0.24)	3.2×10^{-27} (0.25)	9.1×10^{-25} (0.08)
\parallel 21.26	4.6×10^{-28} (1.59)	2.4×10^{-26} (1.92)	6.1×10^{-24} (0.55)
\perp 21.32	6.1×10^{-29} (0.21)	2.7×10^{-27} (0.22)	7.8×10^{-25} (0.07)
\parallel 23.09	1.3×10^{-28} (0.46)	6.7×10^{-27} (0.54)	1.6×10^{-24} (0.15)
\perp 37.37	1.0×10^{-28} (0.35)	4.7×10^{-27} (0.38)	8.7×10^{-25} (0.08)
[43.07]	1.6×10^{-29} (0.06)	2.3×10^{-28} (0.02)	–
[43.34]	1.6×10^{-29} (0.06)	2.3×10^{-28} (0.02)	–
[46.15]	1.9×10^{-29} (0.07)	2.6×10^{-28} (0.02)	–
\perp 54.98	3.9×10^{-28} (1.37)	2.0×10^{-26} (1.60)	3.3×10^{-24} (0.30)
[56.03]	2.6×10^{-29} (0.09)	2.6×10^{-28} (0.02)	–
\perp 69.44	5.1×10^{-29} (0.18)	2.5×10^{-27} (0.20)	1.5×10^{-25} (0.01)
\parallel 70.12	4.8×10^{-29} (0.17)	2.4×10^{-27} (0.19)	1.0×10^{-25} (0.01)
[84.87]	4.4×10^{-29} (0.15)	2.3×10^{-28} (0.02)	–
[175.62]	5.1×10^{-29} (0.18)	1.0×10^{-28} (0.01)	–
\perp 324.88	9.3×10^{-29} (0.32)	3.5×10^{-27} (0.28)	–
[572.66]	1.5×10^{-29} (0.05)	–	–

Table C.33. Like Table C.1 for ovalene ($C_{32}H_{14}$).

Peak (μm)	Integrated flux		
	ISRF (W sr^{-1}) (%)	Red Rectangle (W sr^{-1}) (%)	IRAS 21282+5050 (W sr^{-1}) (%)
15.03	7.9×10^{-30} (0.06)	6.1×10^{-28} (0.08)	3.4×10^{-25} (0.05)
15.26	5.3×10^{-30} (0.04)	3.8×10^{-28} (0.05)	2.0×10^{-25} (0.03)
⊥ 15.90	4.8×10^{-28} (3.60)	3.3×10^{-26} (4.33)	1.7×10^{-23} (2.56)
17.45	7.8×10^{-29} (0.59)	5.5×10^{-27} (0.71)	2.7×10^{-24} (0.40)
⊥ 18.42	2.2×10^{-28} (1.66)	1.6×10^{-26} (2.02)	7.8×10^{-24} (1.15)
20.44	8.4×10^{-28} (0.11)	8.4×10^{-28} (0.11)	3.9×10^{-25} (0.06)
23.57	3.9×10^{-29} (0.29)	2.9×10^{-27} (0.38)	1.3×10^{-24} (0.19)
25.61	1.0×10^{-28} (0.76)	7.3×10^{-27} (0.95)	3.1×10^{-24} (0.46)
⊥ 29.42	8.9×10^{-29} (0.67)	6.6×10^{-27} (0.86)	2.7×10^{-24} (0.39)
36.70	7.6×10^{-29} (0.58)	5.5×10^{-27} (0.71)	2.2×10^{-24} (0.32)
[37.15]	7.9×10^{-30} (0.06)	2.2×10^{-28} (0.03)	–
[39.08]	8.3×10^{-30} (0.06)	2.4×10^{-28} (0.03)	–
⊥ 47.39	1.2×10^{-29} (0.09)	2.4×10^{-28} (0.03)	–
[51.42]	1.3×10^{-29} (0.10)	2.4×10^{-28} (0.03)	–
[65.35]	1.8×10^{-29} (0.13)	2.2×10^{-28} (0.03)	–
[79.27]	1.9×10^{-29} (0.15)	1.9×10^{-28} (0.03)	–
⊥ 93.33	3.4×10^{-29} (0.26)	2.5×10^{-27} (0.33)	4.5×10^{-25} (0.07)
⊥ 160.24	3.1×10^{-29} (0.23)	2.2×10^{-27} (0.28)	–
[161.07]	2.1×10^{-29} (0.16)	7.6×10^{-29} (0.01)	–

Table C.34. Like Table C.1 for the ovalene cation ($C_{32}H_{14}^+$).

Peak (μm)	Integrated flux		
	ISRF (W sr^{-1}) (%)	Red Rectangle (W sr^{-1}) (%)	IRAS 21282+5050 (W sr^{-1}) (%)
15.01	3.2×10^{-28} (1.59)	2.1×10^{-26} (1.91)	1.0×10^{-23} (0.90)
⊥ 15.80	4.5×10^{-28} (2.20)	2.9×10^{-26} (2.71)	1.4×10^{-23} (1.25)
18.29	2.7×10^{-29} (0.13)	1.8×10^{-27} (0.17)	7.2×10^{-25} (0.06)
⊥ 18.47	3.7×10^{-28} (1.80)	2.4×10^{-26} (2.26)	1.0×10^{-23} (0.92)
20.17	3.6×10^{-29} (0.18)	2.3×10^{-27} (0.21)	8.4×10^{-25} (0.07)
25.93	2.3×10^{-28} (1.11)	1.6×10^{-26} (1.44)	5.5×10^{-24} (0.49)
⊥ 28.81	1.1×10^{-28} (0.56)	7.9×10^{-27} (0.73)	2.7×10^{-24} (0.24)
[28.90]	9.4×10^{-30} (0.05)	3.5×10^{-28} (0.03)	–
[29.84]	1.1×10^{-29} (0.06)	3.4×10^{-28} (0.03)	–
[30.82]	1.2×10^{-29} (0.06)	4.1×10^{-28} (0.04)	–
[31.97]	1.3×10^{-29} (0.06)	4.3×10^{-28} (0.04)	–
[32.25]	1.2×10^{-29} (0.06)	4.4×10^{-28} (0.04)	–
35.21	1.6×10^{-29} (0.08)	7.8×10^{-28} (0.07)	–
[36.94]	1.7×10^{-29} (0.09)	5.6×10^{-28} (0.05)	–
[38.39]	1.8×10^{-29} (0.09)	5.7×10^{-28} (0.05)	–
⊥ 46.24	3.3×10^{-29} (0.16)	2.3×10^{-27} (0.22)	2.8×10^{-25} (0.03)
[50.96]	2.9×10^{-29} (0.14)	6.2×10^{-28} (0.06)	–
[63.18]	3.5×10^{-29} (0.17)	5.1×10^{-28} (0.05)	–
[79.15]	4.3×10^{-29} (0.21)	4.9×10^{-28} (0.05)	–
⊥ 87.10	9.0×10^{-29} (0.44)	6.5×10^{-27} (0.60)	1.4×10^{-24} (0.12)
⊥ 157.42	6.5×10^{-29} (0.32)	4.4×10^{-27} (0.41)	1.0×10^{-25} (0.01)
[164.36]	4.9×10^{-29} (0.24)	1.9×10^{-28} (0.02)	–

Table C.35. Like Table C.1 for circumbiphenyl ($C_{38}H_{16}$).

Peak (μm)	Integrated flux		
	ISRF (W sr^{-1}) (%)	Red Rectangle (W sr^{-1}) (%)	IRAS 21282+5050 (W sr^{-1}) (%)
15.29	1.7×10^{-28} (1.12)	1.4×10^{-26} (1.31)	6.4×10^{-24} (0.80)
⊥ 16.00	2.8×10^{-28} (1.82)	2.3×10^{-26} (2.15)	1.0×10^{-23} (1.30)
⊥ 17.63	2.6×10^{-28} (1.71)	2.2×10^{-26} (2.07)	9.2×10^{-24} (1.16)
18.78	5.8×10^{-29} (0.38)	5.2×10^{-27} (0.48)	2.1×10^{-24} (0.26)
⊥ 20.00	2.9×10^{-28} (1.86)	2.4×10^{-26} (2.23)	9.3×10^{-24} (1.17)
21.01	2.1×10^{-29} (0.14)	1.9×10^{-27} (0.17)	6.7×10^{-25} (0.08)
22.75	1.3×10^{-28} (0.85)	1.1×10^{-26} (1.01)	4.0×10^{-24} (0.51)
25.69	2.0×10^{-28} (1.32)	1.8×10^{-26} (1.64)	5.9×10^{-24} (0.74)
⊥ 27.75	3.7×10^{-29} (0.24)	3.4×10^{-27} (0.31)	1.1×10^{-24} (0.14)
⊥ 36.47	3.7×10^{-29} (0.24)	3.3×10^{-27} (0.30)	8.6×10^{-25} (0.11)
⊥ 46.53	2.5×10^{-29} (0.16)	2.2×10^{-27} (0.20)	4.5×10^{-25} (0.06)
48.86	1.6×10^{-29} (0.10)	1.4×10^{-27} (0.13)	2.1×10^{-25} (0.03)
[66.22]	1.1×10^{-29} (0.07)	9.9×10^{-29} (0.01)	–
[73.08]	1.2×10^{-29} (0.08)	9.4×10^{-29} (0.01)	–
[92.81]	1.5×10^{-29} (0.10)	7.1×10^{-29} (0.01)	–
⊥ 96.36	3.7×10^{-29} (0.24)	3.4×10^{-27} (0.32)	4.6×10^{-25} (0.06)
[113.61]	1.6×10^{-29} (0.10)	5.9×10^{-29} (0.01)	–
⊥ 226.20	2.7×10^{-29} (0.18)	1.6×10^{-27} (0.15)	–
[276.62]	1.2×10^{-29} (0.08)	–	–

Table C.36. Like Table C.1 for the circumbiphenyl cation ($C_{38}H_{16}^+$).

Peak (μm)	Integrated flux		
	ISRF (W sr^{-1}) (%)	Red Rectangle (W sr^{-1}) (%)	IRAS 21282+5050 (W sr^{-1}) (%)
15.03	1.6×10^{-29} (0.06)	1.2×10^{-27} (0.07)	3.8×10^{-25} (0.03)
15.25	3.3×10^{-29} (0.12)	2.2×10^{-27} (0.13)	7.2×10^{-25} (0.06)
⊥ 15.94	3.1×10^{-28} (1.14)	2.2×10^{-26} (1.34)	6.8×10^{-24} (0.52)
16.75	6.6×10^{-28} (2.46)	5.0×10^{-26} (3.01)	1.4×10^{-23} (1.06)
⊥ 17.37	2.3×10^{-28} (0.83)	1.6×10^{-26} (0.96)	4.3×10^{-24} (0.33)
18.73	3.0×10^{-28} (1.11)	2.3×10^{-26} (1.37)	5.7×10^{-24} (0.44)
⊥ 19.52	3.1×10^{-28} (1.15)	2.4×10^{-26} (1.47)	5.8×10^{-24} (0.44)
22.53	4.1×10^{-29} (0.15)	3.1×10^{-27} (0.19)	6.7×10^{-25} (0.05)
25.13	2.3×10^{-28} (0.85)	1.8×10^{-26} (1.06)	3.4×10^{-24} (0.26)
⊥ 26.80	6.2×10^{-29} (0.23)	5.0×10^{-27} (0.31)	9.6×10^{-25} (0.07)
⊥ 35.05	1.0×10^{-28} (0.38)	8×10^{-27} (0.48)	1.2×10^{-24} (0.09)
[38.53]	1.4×10^{-29} (0.05)	–	–
[40.80]	1.6×10^{-29} (0.06)	–	–
⊥ 44.96	5.8×10^{-29} (0.21)	4.6×10^{-27} (0.28)	5.4×10^{-25} (0.04)
47.82	3.7×10^{-29} (0.14)	2.8×10^{-27} (0.17)	2.4×10^{-25} (0.02)
[62.14]	3.3×10^{-29} (0.12)	–	–
[70.89]	3.6×10^{-29} (0.13)	–	–
⊥ 84.73	1.4×10^{-28} (0.53)	1.1×10^{-26} (0.68)	1.3×10^{-24} (0.10)
[89.77]	4.6×10^{-29} (0.17)	–	–
[109.51]	5.2×10^{-29} (0.19)	1.7×10^{-28} (0.01)	–
⊥ 237.71	8.4×10^{-29} (0.31)	3.4×10^{-27} (0.20)	–
[353.20]	3.0×10^{-29} (0.11)	–	–

Table C.37. Like Table C.1 for quaterrylene ($C_{40}H_{20}$).

Peak (μm)	Integrated flux		
	ISRF (W sr^{-1}) (%)	Red Rectangle (W sr^{-1}) (%)	IRAS 21282+5050 (W sr^{-1}) (%)
\perp 15.06	8.4×10^{-28} (1.61)	4.1×10^{-26} (1.66)	6.5×10^{-24} (0.77)
\parallel 17.49	4.1×10^{-28} (0.78)	2.0×10^{-26} (0.82)	2.7×10^{-24} (0.32)
\perp 17.58	4.2×10^{-28} (0.80)	2.0×10^{-26} (0.81)	2.6×10^{-24} (0.31)
\parallel 18.52	3.7×10^{-28} (0.71)	1.9×10^{-26} (0.79)	2.3×10^{-24} (0.27)
\parallel 19.38	9.4×10^{-28} (1.80)	4.9×10^{-26} (1.98)	5.4×10^{-24} (0.64)
\parallel 22.64	1.1×10^{-27} (2.15)	5.8×10^{-26} (2.33)	5.3×10^{-24} (0.63)
\parallel 24.63	3.5×10^{-29} (0.07)	2.0×10^{-27} (0.08)	1.3×10^{-25} (0.02)
\parallel 28.32	6.3×10^{-28} (1.22)	3.2×10^{-26} (1.28)	2.1×10^{-24} (0.24)
\perp 32.03	3.1×10^{-28} (0.60)	1.5×10^{-26} (0.60)	8.6×10^{-25} (0.10)
\parallel 34.14	7.2×10^{-29} (0.14)	3.6×10^{-27} (0.15)	1.8×10^{-25} (0.02)
\perp 57.30	1.5×10^{-27} (2.89)	7.5×10^{-26} (3.03)	2.0×10^{-24} (0.24)
\perp 87.48	7.0×10^{-29} (0.13)	3.2×10^{-27} (0.13)	4.5×10^{-26} (0.01)
\parallel 102.85	2.2×10^{-28} (0.42)	1.0×10^{-26} (0.41)	1.6×10^{-25} (0.02)
\perp 471.64	7.7×10^{-29} (0.15)	2.7×10^{-28} (0.01)	–

Table C.38. Like Table C.1 for the quaterrylene cation ($C_{40}H_{20}^+$).

Peak (μm)	Integrated flux		
	ISRF (W sr^{-1}) (%)	Red Rectangle (W sr^{-1}) (%)	IRAS 21282+5050 (W sr^{-1}) (%)
\perp 15.20	5.1×10^{-28} (0.82)	2.6×10^{-26} (0.86)	4.3×10^{-24} (0.28)
\parallel 17.54	1.7×10^{-28} (0.27)	8.4×10^{-27} (0.29)	1.1×10^{-24} (0.07)
\perp 17.87	1.5×10^{-28} (0.24)	7.7×10^{-27} (0.26)	9.8×10^{-25} (0.06)
\parallel 18.53	1.8×10^{-28} (0.29)	9.8×10^{-27} (0.33)	1.2×10^{-24} (0.08)
\parallel 19.07	1.5×10^{-27} (2.35)	7.8×10^{-26} (2.63)	9.2×10^{-24} (0.60)
\perp 21.73	1.0×10^{-28} (0.16)	5.6×10^{-27} (0.19)	5.9×10^{-25} (0.04)
\parallel 22.98	1.6×10^{-27} (2.58)	8.5×10^{-26} (2.88)	8.1×10^{-24} (0.53)
\parallel 23.92	4.8×10^{-28} (0.77)	2.6×10^{-26} (0.89)	2.5×10^{-24} (0.16)
\parallel 28.76	7.1×10^{-28} (1.13)	3.7×10^{-26} (1.26)	2.8×10^{-24} (0.18)
\perp 32.83	1.8×10^{-28} (0.30)	1.1×10^{-26} (0.36)	6.9×10^{-25} (0.04)
\parallel 33.58	3.2×10^{-28} (0.52)	1.7×10^{-26} (0.59)	1.1×10^{-24} (0.07)
\perp 58.08	1.2×10^{-27} (1.90)	6.4×10^{-26} (2.16)	2.8×10^{-24} (0.19)
[81.78]	3.7×10^{-29} (0.06)	–	–
\perp 86.12	9.7×10^{-29} (0.15)	4.7×10^{-27} (0.16)	8.6×10^{-26} (0.01)
\parallel 91.10	3.0×10^{-28} (0.48)	1.6×10^{-26} (0.53)	5.0×10^{-25} (0.03)
[175.98]	5.5×10^{-29} (0.09)	–	–
[184.99]	5.2×10^{-29} (0.08)	–	–
[244.91]	4.5×10^{-29} (0.07)	–	–
\perp 456.34	1.6×10^{-28} (0.25)	1.4×10^{-27} (0.05)	–

Table C.39. Like Table C.1 for dicoronylene ($C_{48}H_{20}$).

Peak (μm)	Integrated flux		
	ISRF (W sr^{-1}) (%)	Red Rectangle (W sr^{-1}) (%)	IRAS 21282+5050 (W sr^{-1}) (%)
\perp 17.44	1.2×10^{-27} (3.61)	7.4×10^{-26} (3.94)	1.9×10^{-23} (1.89)
\perp 18.44	1.3×10^{-27} (4.00)	8.4×10^{-26} (4.45)	2.1×10^{-23} (2.03)
\parallel 18.75	2.6×10^{-28} (0.80)	1.7×10^{-26} (0.89)	4.1×10^{-24} (0.40)
\parallel 19.53	8.3×10^{-29} (0.26)	5.6×10^{-27} (0.30)	1.2×10^{-24} (0.12)
\parallel 21.49	4.3×10^{-28} (1.34)	2.7×10^{-26} (1.44)	5.5×10^{-24} (0.54)
\parallel 24.29	1.6×10^{-28} (0.50)	1.0×10^{-26} (0.54)	1.8×10^{-24} (0.18)
\parallel 24.59	5.9×10^{-28} (1.85)	4.0×10^{-26} (2.10)	6.7×10^{-24} (0.65)
\parallel 27.24	1.2×10^{-28} (0.37)	7.5×10^{-27} (0.40)	1.1×10^{-24} (0.11)
\perp 31.63	7.3×10^{-29} (0.23)	4.8×10^{-27} (0.25)	6.0×10^{-25} (0.06)
\perp 33.41	2.2×10^{-29} (0.07)	1.5×10^{-27} (0.08)	1.6×10^{-25} (0.02)
\perp 71.79	3.1×10^{-28} (0.98)	2.0×10^{-26} (1.09)	1.1×10^{-24} (0.11)
[96.67]	1.5×10^{-29} (0.05)	–	–
\parallel 101.49	5.7×10^{-29} (0.18)	3.4×10^{-27} (0.18)	1.0×10^{-25} (0.01)
\perp 101.68	8.9×10^{-29} (0.28)	5.7×10^{-27} (0.30)	2.1×10^{-25} (0.02)
[110.05]	1.5×10^{-29} (0.05)	–	–
[175.85]	1.5×10^{-29} (0.05)	–	–
\perp 390.11	5.4×10^{-29} (0.17)	7.2×10^{-28} (0.04)	–

Table C.40. Like Table C.1 for the dicoronylene cation ($C_{48}H_{20}^+$).

Peak (μm)	Integrated flux		
	ISRF (W sr^{-1}) (%)	Red Rectangle (W sr^{-1}) (%)	IRAS 21282+5050 (W sr^{-1}) (%)
\parallel 15.01	4.4×10^{-28} (0.82)	3.0×10^{-26} (0.95)	5.3×10^{-24} (0.32)
\parallel 16.60	1.4×10^{-27} (2.58)	9.2×10^{-26} (2.97)	1.5×10^{-23} (0.89)
\perp 17.59	1.1×10^{-27} (2.12)	7.6×10^{-26} (2.43)	1.1×10^{-23} (0.66)
\perp 18.61	7.3×10^{-28} (1.34)	4.9×10^{-26} (1.57)	6.7×10^{-24} (0.40)
\parallel 19.31	3.2×10^{-28} (0.59)	2.1×10^{-26} (0.67)	2.8×10^{-24} (0.17)
\parallel 20.18	9.6×10^{-29} (0.18)	6.3×10^{-27} (0.20)	8.3×10^{-25} (0.05)
\parallel 22.26	5.2×10^{-28} (0.96)	3.5×10^{-26} (1.13)	3.9×10^{-24} (0.24)
\parallel 24.33	6.2×10^{-28} (1.16)	4.0×10^{-26} (1.30)	4.2×10^{-24} (0.25)
\parallel 25.31	1.3×10^{-27} (2.36)	8.7×10^{-26} (2.79)	8.4×10^{-24} (0.51)
\parallel 27.50	1.6×10^{-28} (0.30)	1.1×10^{-26} (0.35)	9.4×10^{-25} (0.06)
\parallel 28.79	2.2×10^{-27} (4.13)	1.5×10^{-25} (4.79)	1.3×10^{-23} (0.79)
\perp 32.15	3.8×10^{-29} (0.07)	2.6×10^{-27} (0.08)	2.2×10^{-25} (0.01)
\perp 33.81	3.9×10^{-29} (0.07)	2.4×10^{-27} (0.08)	1.9×10^{-25} (0.01)
\perp 72.81	4.6×10^{-28} (0.85)	3.1×10^{-26} (1.00)	1.6×10^{-24} (0.10)
[88.81]	4.0×10^{-29} (0.07)	–	–
[94.35]	4.4×10^{-29} (0.08)	–	–
\parallel 99.45	8.3×10^{-29} (0.15)	5.1×10^{-27} (0.16)	8.3×10^{-26} (0.01)
\perp 103.49	1.4×10^{-28} (0.25)	9.1×10^{-27} (0.29)	2.5×10^{-25} (0.02)
[109.70]	5.2×10^{-29} (0.10)	–	–
[172.53]	5.4×10^{-29} (0.10)	–	–
\perp 402.76	1.3×10^{-28} (0.25)	1.8×10^{-27} (0.06)	–